Data-driven Modeling Implementation within Materials Development and Manufacturing Systems

Allen Jonathan Román

A dissertation submitted in partial fulfillment of

the requirements for the degree of

Doctor of Philosophy

(Mechanical Engineering)

at the

UNIVERSITY OF WISCONSIN-MADISON

2023

Date of final oral examination: September 14th, 2023

The dissertation is approved by the following members of the Final Oral Examination Committee:

Tim A. Osswald, Professor, Mechanical Engineering
Lih-Sheng Turng, Professor, Mechanical Engineering
Pavana Prabhakar, Assistant Professor, Civil and Environmental Engineering
Alejandro Roldán-Alzate, Assistant Professor, Mechanical Engineering
Lianyi Chen, Assistant Professor, Mechanical Engineering

Abstract

Predicting polymeric material behavior during processing and predicting final part properties continues to be a strong research focus within the scientific community as it involves taking into consideration a wide range of time-dependent variables. By use of data-driven modeling, the materials development process can be accelerated, and the highly predictive modeling techniques can facilitate the development of smart manufacturing systems.

This dissertation worked on solving polymer engineering problems by use of data-driven modeling techniques. The first strategy was using data-driven modeling to provide a predictive model with statistical insights of the injection molding process to ensure part quality is maximized for a highly viscoelastic material blend. By injection molding highly viscoelastic materials, the probability of part defects is increased, therefore, it was crucial to use advanced computational techniques to understand the nuances of this highly non-linear process and to predict the outcome before creating material waste from faulty trials.

The second strategy was in the use of data-driven modeling for reverse engineering purposes, specifically within materials development. By combining experimental characterization and data-driven modeling, algorithms were developed and compared to prove how highly predictive models can be used as reverse engineering toolboxes. This ultimately informed users of the optimal formulation which would reach the specified target material properties.

The final strategy explored using data-driven modeling to validate the high influence of viscous heating within the pressure melt removal process, therefore, work was done in implementing a viscous heating system within a fused filament fabrication (FFF) 3D printer to accelerate the 3D printing process. The instrumented FFF 3D printer proved capable of accelerating print speeds and improving mechanical performance of 3D printed parts, working towards solving two of the largest bottlenecks within additive manufacturing: lead times and part quality. Given the unique capabilities of the data-driven modeling, the novel 3D printer was tested and evaluated via data-driven modeling to provide statistical information regarding which processing parameters were the most influential for improving overall performance of the 3D printing system.

The results of this work provide a basis for future research endeavors related to combining data-driven modeling and polymer science, such as in optimizing the newly developed viscous heating 3D printer.

Keywords: Data-driven Modeling, Polymer processing, Materials Development, FFF

Acknowledgements

First, I'd like to thank my advisor and mentor, Professor Tim Osswald as he provided me with an amazing opportunity to grow alongside many great researchers at the Polymer Engineering Center. You have provided me with countless technical support and numerous jokes to include within my repertoire. *Seguiré poniendo en alto a los Latinos y mi 0.7% parte judía.*

My deepest gratitude to the members of my dissertation committee: Prof. Turng, Prof. Prabhakar, Prof. Roldán and Prof. Chen. Thank you for your valuable input, time, and support throughout my time as a graduate student.

I also would like to show my gratitude to all of the undergraduate students, professionals and visiting scholars who made this research possible. Special mentions go to Juan Blanco, John Estela, Tzu-Chuan Chang, Abrahan Bechara, Oliyad Dibisa, and Shiyi Qin, whose brainstorming sessions represent an integral part in my growth as a researcher. Of course, I must thank the PEC family as the PEC was much more than a research lab. The PEC embodied a home away from home as we all struggled together and celebrated together our personal and professional successes.

It is also important to thank Diana, my fiancé, whose unwavering support helped me stay afloat throughout my PhD and is the reason why I am writing this dissertation. Thanks to Elsie, my sister, you and Diana inspired me to be involved in my community and to pursue goals bigger than myself.

Lastly, Mom and Dad, you walked for days across a desert to give Elsie and me the opportunity to pursue our dreams. You sacrificed everything for us, taught us the most valuable life-lessons and are my inspiration. *Les debo todo a ustedes y espero un día ser grandioso como ustedes.*

Front Matter

List of Acronyms

1-D	One-dimensional
2-D	Two-dimensional
3-D	Three-dimensional
AM	Additive Manufacturing
ANN	Artificial Neural Network
BO	Bayesian Optimization
CAE	Computer aided engineering
CB	Carbon Black
CNC	Computer Numerical Control
CV	Cross-validation
DA	Dimensional Analysis
DMA	Dynamic Mechanical Analyzer
DOE	Design of experiment
DSC	Differential Scanning Calorimetry
FDM	Fused Deposition Modeling
FEA	Finite Element Analysis
FFF	Fused Filament Fabrication
FL	Fiber length
FO	Fiber orientation
GPR	Gaussian Process Regression
HA	Shore A hardness
HDPE	High-density Polyethylene
iARD-RPR	Improved Anisotropic Rotary Diffusion with the Retarding Principal Rate model
LAOS	Large Amplitude Oscillatory Strain
LR	Linear Regression
LR	Logistics Regression
MAE	Mean Absolute Error
MFI	Melt Flow Index
ML	Machine Learning
MPa	Megapascal
MW	Molecular Weight
NN	Neural Network
NR	Natural Rubber
PA	Nylon

PA66	Nylon 66
PEC	Polymer Engineering Center
PEEK	Polyether ether ketone
PP	Polypropylene
PPH	Part per Hundred
PTFE	Polytetrafluoroethylene
RBF	Radial Basis Kernel
RPM	Revolution per Minute
RSM	Response Surface Method
SABIC	Saudi Basic Industries Corporation
SVM	Support Vector Machine
TMTD	Tetrmethylthiuram Disulfide
TTS	Time Temperature Superposition
UHMW	Ultra-high Molecular Weight
VH	Viscous Heating
ZnO	Zinc Oxide

List of Symbols

a_{11}	Fiber orientation tensor in the flow direction
a_{22}	Fiber orientation tensor in the crossflow direction
a_{33}	Fiber orientation in the thickness direction
b	SVM Bias
β_0	Linear/Logistics regression intercept
β_i	Linear/Logistics regression feature weights
C_m	Fiber-matrix interaction coefficient
C_i	Fiber-Fiber interaction coefficient
De	Deborah Number
ε	Linear/Logistics regression computed error
F_{sz}	Filament Force
F	Force
h	Hours
Hz	Hertz
l	Length of Part
L_N	Number Average Fiber Length
L_W	Weight Average Fiber Length
N_i	Number of Fiber
K	Fiber Breakage Coefficient
R^2	R-squared
$R^2_{adjusted}$	R-squared of the variation in the response
$R^2_{predictions}$	R-squared of predictions
x_i	SVM feature variable
w_i	SVM feature weight
λ	Relaxation time
T_g	Glass transition temperature
μ	Fluid viscosity
t	Thickness of Plate

u	Injection Speed
T	Process Temperature
ρ	Melt Density
λ	Relaxation Time
k	Thermal Conductivity
Π	Dimensionless Number
u_i	Injection Speed
$\tan\delta$	Tangent of delta
n_{relax}	Relaxation Decay Constant
σ_{relax}	Maximum Relaxation Stress
μCT	Microcomputed Tomography
r	Pearson Correlation Coefficient
S	Percentage of Variation
R	Radius of Filament
δ	Melt film
W	Watt
N	Newton
$\%wt$	Percent weight of loading
$\dot{\gamma}$	Shear rate
t	Time
s	Seconds
v_z	Velocity in the z-direction

List of Figures

List of Tables

Introduction

The ability of acquiring experimental data has become more economically feasible, and for that reason machine learning scientist positions have been recently created with more frequency. Machine learning scientists focus on acquisition of data, processing and in the implementation of these big data sets within data-driven modeling algorithms to provide predictions for industry. It is important to note that one does not necessarily have the ability to predict all types of events, ranging from sale projections to scientific projections relating to material behavior if one has a lot of data. A crucial aspect of these data-driven modeling implementation studies is in the proper selection of training parameters that one will extract from real experimental set ups or simulation. Users must be able to select the training parameters that are the most influential for the output, and the appropriate algorithm for the specific data set to ensure noise is reduced and convergence rate is maximized, respectively. Regarding polymer science and machine learning, a bridge between both disciplines needs to exist in order to acquire valuable data, and to minimize the amount of experimentation needed to train a robust algorithm.

Data-driven modeling has the ability, if implemented appropriately, to predict material behavior, polymer process performance, formulations, and to provide controls information for close-loop systems in charge of optimizing process performance based on real experimental data, to name a few. Implementing data-driven modeling, such as machine learning within the above-mentioned cases is crucial as the plastics industry highly depends on one's experience to minimize loss-time. For example, a custom polymer blend formulator is compensated heavily for their experience as their knowledge will be leveraged to ensure they understand the effects one additive may incur on

the overall blend and the interacting effects each additive has on one another. Before industry started proposing eco-friendly initiatives to reduce their carbon footprint, the formulator's priority was to purely optimize performance and to not prioritize sustainability. Now with industry embracing sustainable materials development, they now must maximize performance while also minimizing the inclusion of additives detrimental to the environment. Such duty to now optimize two variables has turned into an exceedingly complex task, as these effects may incur non-linear effects to performance. For that reason, machine learning is a valuable tool which with the appropriate training data, one could model and predict material behavior for large amounts of theoretical experiments without having to physically conduct the experiments.

The aim of this work is to enable polymer engineers to predict highly non-linear occurrences with the aid of data-driven modeling toolboxes by providing algorithms, varying in complexity, capable of reverse engineering current materials, predicting defects during polymer processing, and employing a predictive system within fused filament fabrication (FFF) 3D printing which informs users of ongoing defects during 3D printing.

1. Background

1.1 Modeling Approaches

Machine Learning (ML) is a computational method in which mimics human learning by combining statistics and optimization methods. Using such methods allows for algorithms to classify or predict very complex events, and to uncover valuable information regarding influential factors to those outcomes [1]. Key insights extracted from the algorithms serve as guides for decision-making within the application and further acquisition of data allows for continuous improvements, accelerating the optimization of the system [2]. There exist various types of machine learning algorithms, but most fall within the two types of categories: Supervised learning or unsupervised learning.

Supervised learning involves a predictive algorithm that uses data that has the outcomes defined for training purposes. As seen in the flow chart below (Figure 1), a portion of the data is set aside for testing purposes while the remainder of the data is used for training where the model continuously adjusts its rules (for example: weights and biases) until the error between the predicted and actual value is minimized [3]. Unsupervised learning uses machine learning algorithms to analyze and group unlabeled data. The algorithm is in charge of identifying patterns and establishing connections between data without a user to aid in this classification [3].

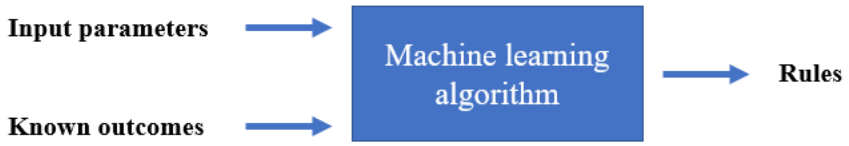

Figure 1. Schematic of machine learning basic theory

1.2 Best Practices for Machine Learning Algorithm Development

The excitement in industry with applying machine learning algorithms has led many to treat machine learning like a black box where one simply inputs large amounts of data into an artificial neural network (ANN) and calls it a day. A developer needs to choose the appropriate machine learning algorithm based on the size of the data, the desired outputs, and the type of inputs fed into the model. Once the testing algorithms are chosen, it is important to develop an unbiased training and testing strategy to ensure that underfitting and overfitting is avoided.

In general, overfitting is when a model has the ability to predict the training data too well. After training, it is unable to neglect noise and predicts inaccurate outputs. This occurrence can be avoided by not including data which has high variance and by introducing early stops within the model to ensure training is sufficient enough for prediction but not long enough in which the model learns from noise. Overfitting can also be avoided by implementing cross-validation (CV), which involves partitioning the data into n equal parts and conducting n independent trials where each part is used once for testing (Figure 2).

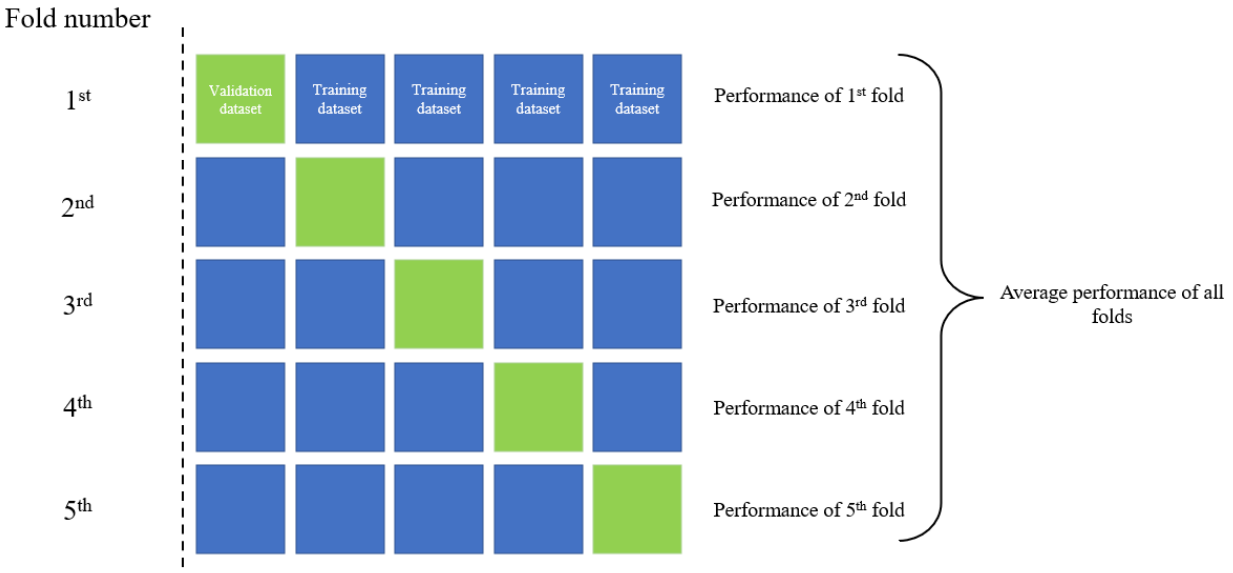

Figure 2. Schematic explaining the theory of cross validation

Underfitting arises when training does not converge and is not able to predict training data effectively. This issue may be addressed by increasing the model complexity, increasing the number of input parameters and by increasing the amount of data used in training to ensure it has enough information.

1.3 Linear and Logistics Regression

Linear regression is the simplest machine learning algorithm to implement as it involves finding a linear relationship between experimental data. Given an accurate model, this supervised machine learning model is primarily used to provide forecasting information based on user inputs and the parameters used for regression give insight into relationships between input and output variables [4]. Linear regression is described using the function seen in Equation 1 below, whereas the summation results in the weighted sum of its n features. Moreover, β_0 represents the intercept, β_i represents the feature weights, and ε corresponds to the difference between the computed prediction and the known outcome.

$$y = \beta_0 + \beta_1 x_1 + \beta_2 x_2 + \cdots + \beta_n x_n + \varepsilon \quad (1)$$

Logistics regression machine learning algorithms are primarily implemented in classification problems where the output can be described in binary format. In logistics regression, a weighted

sum of the inputs is passed through a sigmoidal activation function (Figure 3) whereas a 0 and 1 output is possible, ultimately allowing the user to represent a “No” with a zero and a “Yes” with the number one [5]. The classification model follows Equation 2 below and follows similar nomenclature to what is appreciated in Equation 1 above.

$$P(y=1) = \frac{1}{1+\exp\left(-(\beta_0 + \beta_1 x_1 + \beta_2 x_2 + \cdots + \beta_n x_n)\right)} \tag{2}$$

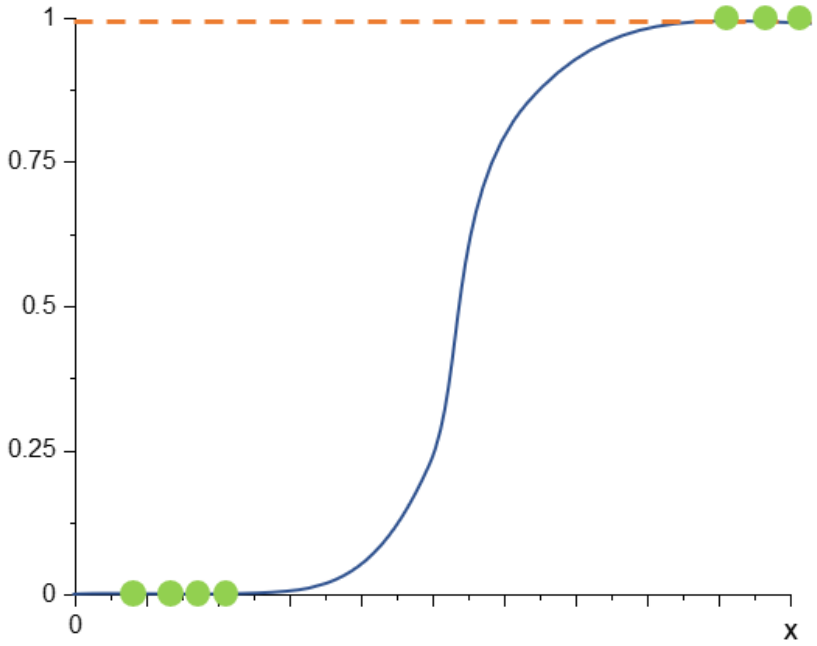

Figure 3. Sigmoidal function logic theory

Both Linear and Logistics regression models provide simple but resource-efficient predictive models which provide users with statistical information regarding significant input variables.

1.4 Response Surface Methodology

Introduced by George E. P. Box and K. B. Wilson in 1951, the Response Surface Method (RSM) uncovers the interconnectivity between various controllable factors and several response variables using nonlinear modeling. It should be acknowledged that RSM serves as an approximation method that provides a relatively simple method for modeling, estimating, and optimizing based on target parameters [6-8]. By use of mathematical and statistical techniques, an empirical model is created from experimental data and is used to evaluate the fit to a statistical model (linear, quadratic, cubic or two-factor Interaction), as described in Equation (3) below.

$$Y = a_0 + \underbrace{a_1A + a_2B + a_3C}_{\text{Linear}} + \underbrace{a_4A^2 + a_5B^2 + a_6C^2}_{\text{Quadratic}} + \underbrace{a_7AB + a_8AC + a_9BC}_{\text{Two-Factor}} \quad (3)$$

Using natural rubber formulation as an example, the independent variables A, B, and C may represent additives used within the formulation, such as: sulfur content, paraffin oil content, and void content, respectively. The output response Y represents the material property one aims to optimize. The coefficients ($a_0 - a_6$) determined by the model within the linear and quadratic sections dictate the influence each respective variable has on the output, Y, while the Two-Factor coefficients ($a_7 - a_9$) of the quadratic model above quantify the level of influence that interactions between two variables have on the output [6-9]. As mentioned above, formulating is a balance between various additives and RSM allows for the user to determine, to some degree, the interaction effects between two controllable variables.

Once the model is created, RSM allows for the optimization of a blend based on target responses, maximizing a specific response, or minimizing a specific response. The options available via RSM are of value as some additives may result in a dramatic increase in raw material expenditure, therefore, one can have a combination of various formulations which maximize certain controllable factors and minimize others to ensure cost rises are mitigated. Additionally, each target response may be given an importance value ranging from 0.1 to 10 if the user is more interested in some responses compared to others. If all target responses are of equal importance, then the default value should be 1. Moreover, if one target response is crucial for the user, the importance value can be increased up to a value of 10. Furthermore, weights may be assigned to each target response with values ranging from 0.1 to 10. The weights influence the desirability function shape between the lower/upper bounds and the target. Figure 4 below shows how different weights may influence the desirability function shape, where it can be seen that a larger weight creates a sharper, and quicker convergence to the target response.

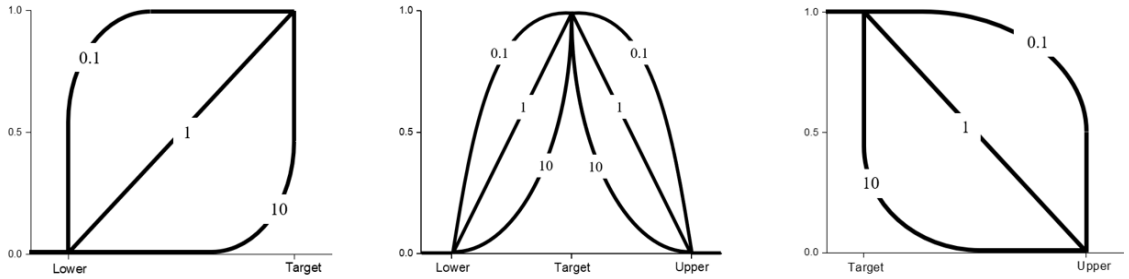

(**a**) (**b**) (**c**)

Figure 4. Desirability functions for different goals and how weights influence their respective shapes. (a) Minimize the response, (b) Achieve target value, and (c) Maximize the response

Although the quadratic function is mathematical, the statistical analysis of this regression model is key for interpreting the model. Minitab® 20 may be used for the RSM study whereas a 95% confidence level may be selected as the threshold for statistical significance. The Pareto chart of the Standardized Effects lists the standardized coefficients to understand which terms have the highest influence on each given response. By observing the magnitude of the standardized effect, the user can understand which controllable factors are the most influential and if a combination of controllable factors creates significant change to the output response. The dashed line within the Pareto chart indicates a significance level of $\alpha = 0.05$, therefore, anything to the right of the line suggests a term that is statistically significant to the response [6-8,10].

Additionally, the Coded Coefficients, such as the coefficients and *p*-value for each respective controllable factor allow the user to determine if a specific term is significant. If $p - \text{value} \leq \alpha$, the association is statistically significant, and if $p - \text{value} > \alpha$, the association is not statistically significant. Finally, the Model Summary is described by the standard deviation of the distance between fit values and input data values (S), the percentage of variation within the model response (R^2), the adjusted R^2 which is the variation in the response adjusted for the number of predictors in the model relative to the number of observations (R^2_{adjusted}), and the R^2 of the predictions which indicates how well the model predicts the removed observations ($R^2_{\text{predictions}}$). It is important to note that if $R^2_{\text{predictions}}$ is substantially less than R^2 then this may indicate that the model tends to overfit.

1.5 Support Vector Machine

Support vector machine (SVM) is a supervised machine learning algorithm best suited for classification and regression-type analyses. This method functions by partitioning data into clusters which separate outcomes from one another [11]. Figure 5.a and 5.b below show how 1-D and 2-D hyperplanes partition datasets effectively, allowing for accurate classification.

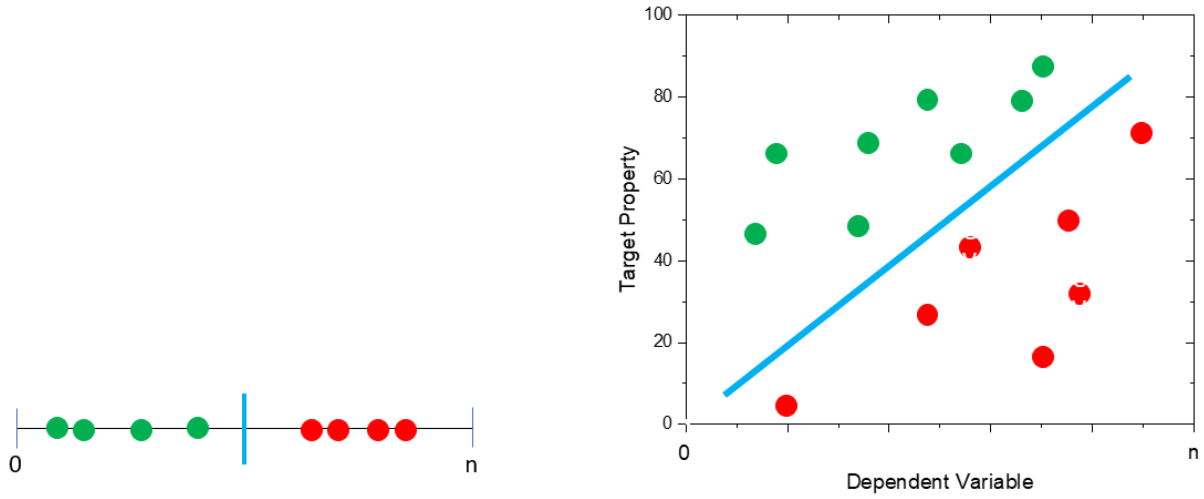

Figure 5. A graphical depiction of a (a) 1-D hyperplane partition and a (b) 2-D hyperplane partitioning

It allows for linear classification but is also capable of non-linear classification by introducing the "Kernel Trick", a method in which the input data is mapped onto a high-dimensional feature space [12], ultimately transforming the shape of the response curve. Figure 6.a and 6.b below shows a graphical representation of what the Kernel Trick can do when a dataset is deemed unclassifiable within a two-dimensional space. Figure 6.a shows scattered data within a 2-dimensional space which cannot be partitioned by a simple hyperplane. The algorithm will result in large amounts of misclassifications if the threshold is defined as a hyperplane. By using the polynomial Kernel trick, the shape of the data is altered and allows for a hyperplane to effectively partition the data within the three-dimensional space, as seen in Figure 6.b. The Kernel Trick is a valuable tool for polymer scientists formulating new materials as an additive does not always have an increasing/decreasing effect [13]. This is apparent for cases in which one assumes that increasing the amount of carbon-black (CB) reinforcement in a natural rubber (NR) formulation will result in an only increasing elongation at break, when evidently it is not the case as it has been proven that surpassing the 30

parts per hundred (pph) of natural rubber concentration begins to steadily decrease the elongation at break as the heavy load of reinforcement no longer has enough polymer material to adhere to, causing a weaker brittle fracture [14].

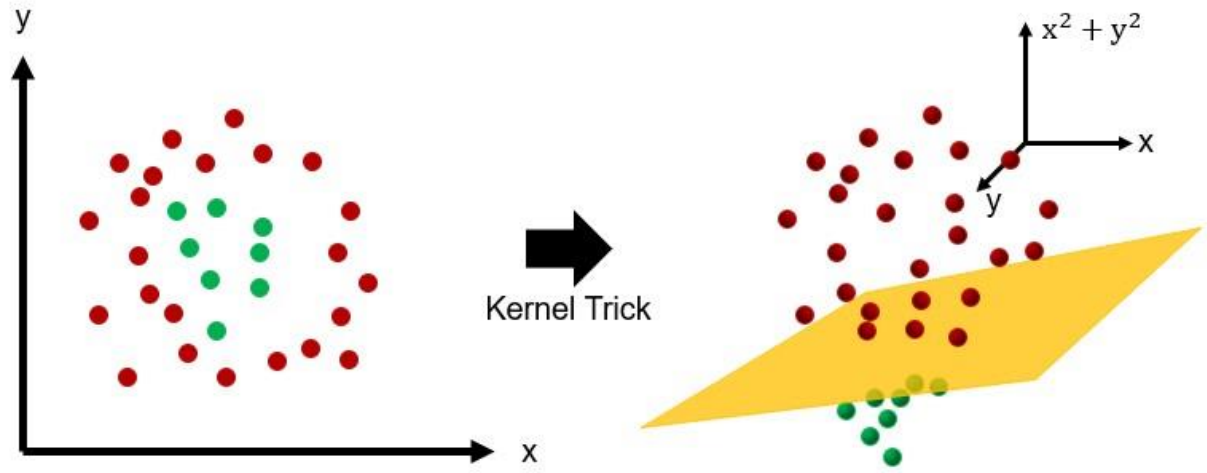

Figure 6. An unclassifiable (a) 2-D problem transformed into a (b) 3-D problem via the Kernel Trick

SVM is one of the most common types of machine learning algorithms implemented as it is effective with small datasets and can be implemented within higher dimensional spaces. The partitioning hyperplane follows the form of Equation 4 seen below, whereas alike linear regression, the weights and biases that make up the partition provide a quantitative insight into which input parameters have the most influence on the overall system.

$$y = \begin{bmatrix} w_1 \\ w_2 \\ \vdots \\ w_n \end{bmatrix} [x_1 \quad x_2 \quad \cdots \quad x_n] + b \tag{4}$$

$$x_i = \text{feature variable}$$

$$w_i = \text{feature weight}$$

$$b = \text{bias}$$

1.6 Artificial Neural Networks

Neural Networks (NN), also known as Artificial Neural Networks (ANNs) are inspired by the human brain as they mimic the way in which neurons signal one another to make decisions [15]. Artificial neural networks, which have added nonlinearity compared to SVM, are a powerful modeling method that can approximate highly nonlinear functions [16]; it can be used to explore complex relationships between experimental design parameters and material properties. The basic architecture of a fully connected ANN can be seen in Figure 7, and consists of an input layer, hidden layer(s), and an output layer. The designer can increase or decrease the number of hidden layers and nodes within the network, ultimately allowing for the development of a complex ANN. This modification of an ANN architecture is crucial as it may lead to a faulty algorithm that overfits data.

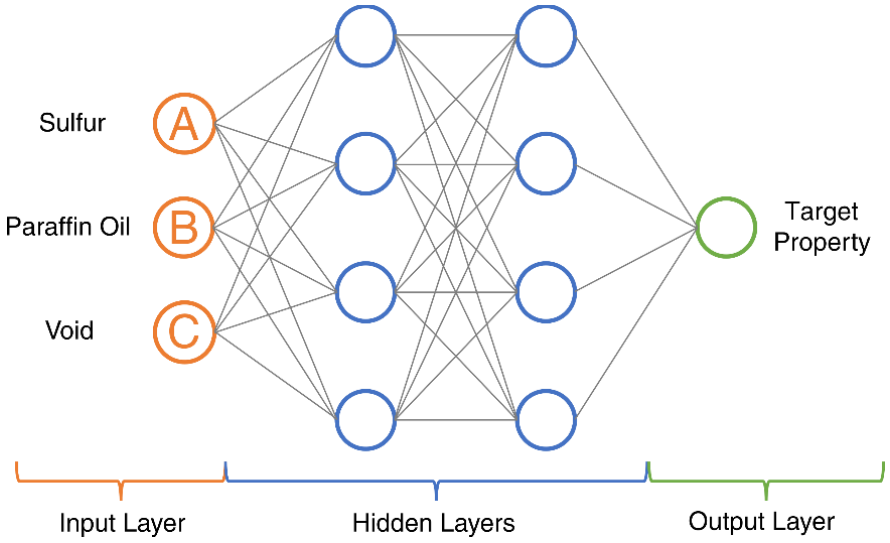

Figure 7. Simple artificial neural network structure

The input layer includes a node for each parameter that influences the final outcome. The connecting line between the input layer node and hidden layer node is initially assigned a random weight, while the hidden layer includes several nodes specified by the user, which also is randomly assigned a bias. Furthermore, the output layer includes the classification node(s) where the expected outcomes are extracted experimentally or computationally. Ultimately, the way an ANN functions is by multiplying each input node parameter by the weight of the connecting line and adding this value to that hidden layer node's specific bias value. This value is then passed through a nonlinear activation function, added to the weight assigned to the connecting line between the

hidden layer node and the output layer node, and then added together. The summation is then compared to the experimental data point in the form of a loss function that penalizes for incorrect prediction. To minimize the loss function (difference between the output and the experimental data), the backpropagation algorithm [16-17] would occur by specifying the gradient of the loss function with respect to all the weights as well as biases; this is followed by the gradient descent optimization step that slightly changes the weights and biases' values in the loss decreasing direction based on the calculated gradient. Unlike the common way to compute gradient where an analytical expression is first established, the backpropagation algorithm utilizes the chain rule of calculus to simplify the procedure. And as a result, the gradient is broken down into the product of several partial derivatives whose numerical values are easier to evaluate and less computationally expensive [16]. This re-assigning of weights and biases is considered the learning phase, which requires multiple iterations and data points to create a valid representation of the model. Once the learning phase is complete, the model stores the weights and biases for subsequent runs to predict events given specific inputs which it has not seen.

1.7 Gaussian Process Regression

Gaussian process regression (GPR) [18] is another class of supervised learning algorithms. Unlike ANNs, GPR makes probabilistic predictions in the form of mean and variance, and therefore uncertainties of the predictions can be calculated. With such information, one can potentially design additional experiments that target the region with high uncertainty. Another advantage of GPR lies in its “non-parametric” nature, and minimal hyperparameters need to be learned. Compared with ANNs whose number of parameters can easily add up to thousands and millions when increasing layers, GPRs usually carry fewer hyperparameters to tune. In general, GPR loses efficiency for high-dimensional data but works well with small datasets. Mathematically, GPR utilizes a Gaussian process prior that is specified by the means and covariance matrices of the training and validation/testing data. The covariance matrices (hyperparameters) are optimized during the training process and serve as a way to approximate the similarity between a test input and the training inputs, which eventually leads to the prediction of the test output based on the training outputs through matrix operation [18].

As illustrated in a one-dimensional example in Figure 8 below, GPR learns from the given data points (training data) and predicts the “y” values with a mean and variance. The region with

training data shows a narrower variance than the region without training data. Based on the mean and variance, a sample curve (dashed line) can be drawn from the predicted distribution.

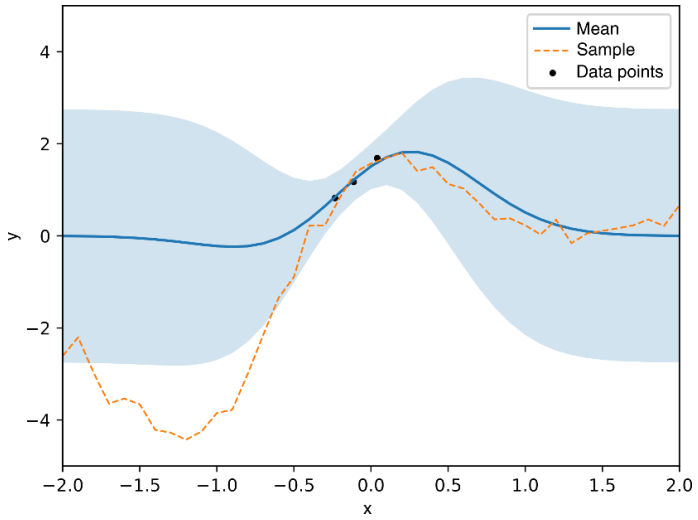

Figure 8. An illustration of GPR and how more data increases the predictive capabilities

1.8 Progress in Machine Learning within Polymer Science

The complex relationship between highly viscoelastic materials and the end-product after production is not completely understood, therefore, traditionally physics-based simulations are designed to give the user an approximation of what might be the outcome [19]. As customary for all simulation approaches, the simulation is only good if it agrees with experimental data, therefore, one must have full understanding of what fitting parameters are suitable for each of the physics-based models being applied. One example: when using the iARD-RPR model in Moldex3D for a mold-filling simulation of a fiber-reinforced thermoplastic part, it is critical to understand how all three fitting parameters ($C_m, C_i,$ and K) influence the fiber orientation distribution. For this application, there are sets of rules that users must abide by, for example, the C_m represents the fiber-matrix interaction coefficient which must be within a certain range when working with short fibers [20-21]. This know-how in setting a proper simulation is what defines whether your simulation will compute to a result similar to what is occurring in the real-world. For that reason, the implementation of sensors within a process and characterization of the end product allows for the acquisition of valuable data which can be fed into a specific data-driven modeling algorithm capable of predicting the outcome of interest.

The implementation of machine learning within polymer processing has reached various areas within additive manufacturing in regard to extrusion behavior [22,23], prediction of injection molding events [24–26], and post-production material behavior [27–30]. The common denominator for above-mentioned applications is that they require real experimental data to aid in the creation of representative models.

As injection molding is one of the most utilized manufacturing processes throughout industry, the final part can have various defects, including warpage, short shot, thermal degradation, parting lines, and flash [31-34]. Previous work included using the Taguchi optimization method to quantitatively determine how influential specific processing parameters were in regard to warpage in injection molded parts within Moldflow simulations [35-37]. Similarly, optimization methods have also introduced machine learning within the framework of the optimizer. However, it is vital to understand that optimization methods that depend exclusively on CAE simulation data are not 100% accurate as they do not fully capture all the physics involved in polymer processing. For that reason, research has been conducted in predicting occurrences within injection molding by developing predictive frameworks [38-39] and including real experimental data as training data. For example, Saad Mukras' optimization framework, based on the Kriging Model, predicted cycle time, warpage, and volumetric shrinkage with an error of 6.7%, 3.2%, and 8%, respectively, by analyzing samples from real injection molding trials [40]. For that reason, it is evident that an optimization approach that accompanies real experimental data has the ability, if set up correctly, to have higher accuracies compared to one with no real experimental data. Additionally, researchers such as Yarlagadda have taken it a step further and applied these neural network optimization methods within controlling systems to automatically adjust injection molding machine parameters [41, 22].

2. Manufacturing Process Outcome Prediction via Machine Learning

2.1 Introduction

Seeking materials with high strength and compliance characteristics has led scientists to develop materials that combine a high strength material with a material that can withstand significant deformations. Of these engineered materials, model polypropylene (PP) blends create a balanced material that exhibits high impact strength at low temperatures while still exhibiting high-performance properties at elevated temperatures. These superior low-temperature properties are attributed to the elastomer modification's cross-linked nature, which gives it the ability to be processed like thermoplastic materials. The morphology of these model polypropylene materials are a blend of external elastomers or reactor-based materials, which are subject to change depending on the flow conditions. Flow conditions ultimately alter the elastomeric compound's orientation within the cavity, and the alignment of those molecules creates various surface properties, such as glossy or matte finishes [42]. Not only are aesthetic defects caused by the morphology of the compounded material, but the mechanical performance of such parts is also influenced by crystal orientations [43]. Mechanical defects can occur in live hinges and weld lines, whereas the strength of the overall part may become compromised at these locations.

Moreover, the crystallinity of the elastomer material contributes to the material's mechanical properties, where Wu and coworkers were able to demonstrate the relationship between the chain structure and toughness of the polymer-elastomer blend [44]. Although elastomer modifications improve the material's impact strength, it causes a decrease in the flexural modulus, which can be

addressed by adding high-density polycomonomer (HDPE) into the system [45-46]. An example of such material that can withstand large deformations is elastomers, as the curled polymer chains can stretch until above 400% elongation [47]. Although a valid idea to use a polypropylene-elastomer composite as a material with high strength and high compliance attributes, manufacturability is the next challenge to face since using non-Newtonian fluids with high viscosities has never been straightforward [48]. A balance between stiffness and elasticity is necessary to ensure that the material can acquire the benefits of elastomers in regard to elasticity while avoiding processability issues because of its high viscosities due to high molecular weight [49].

Furthermore, the probability of flow instabilities occurring during polymer processing increases as you include highly viscoelastic materials, and finding the correct balance between flow rates and processing temperatures is crucial as many instabilities occur at different regions within the shear rate vs. shear stress regime. Navigating through these regimes requires a solid understanding of that specific material where time-temperature-superposition (TTS) could help determine the locations where smooth and defect-free flows are present [50-51]. Given that irregular flow patterns may cause sharkskin defects in extrusion, it is crucial to understand how these irregular flows may also occur within the mold filling process, which can create defects within the part. This work focuses on how machine learning can predict surface defects using processing parameters and viscoelastic properties as the input. Furthermore, it is proven how optimization approaches can be implemented to create a simplified and more robust predictor.

This work focuses on the development of a neural network (NN) for surface defect prediction in injection molding of model polypropylene. Feature optimization allows us to conclude that rheological parameters such as the melt flow index (MFI) and relaxation time (λ) can improve predictive accuracy. Furthermore, Bayesian optimization (BO) is implemented to optimize the NN structure. The optimization approach allowed for a cross-validation (CV) accuracy of 90.2% $\pm$ 4.4% with only five input parameters, while the seven-input parameter optimized structure arrived at a CV accuracy of 92.4%$\pm$11.4%. Although the full-feature structure optimized with Bayesian optimization concluded with slightly higher accuracy, the error range dramatically increased, meaning that this structure tends to overfit.

2.2 Materials and Characterization Methods

Materials and Data

The Saudi Basic Industries Corporation, known as SABIC, provided sets of model samples with varying elastomer content, processing agent content, and varying comonomer content. Besides their material makeup, every injection molding piece was processed at 240°C and processing speeds u_D, u_E or u_F corresponding to 20 mm/s, 50 mm/s and 160 mm/s, respectively. The injection molding processing parameters in Table 1 below were kept constant in the study.

Table 1. The injection molding parameters kept constant for all trials on the Arburg 60T injection molding machine (Molded by Intertek, the Netherlands).

Processing Parameter	**Value**
Hopper Temperature [°C]	40
Zone 1 Temperature [°C]	200
Zone 2-4 Temperature [°C]	240
Holding Pressure [bar]	200
Back Pressure [bar]	40
Cooling Time [sec]	33
Screw Rotation [RPM]	318

Additional to processing parameters, the injection-molded plates were also produced with two different gate geometries, a fan gate and a pin gate, to characterize how gate restriction altered the system. SABIC also provided melt flow index (MFI) measurements per ISO 1133. Injection-molded plate photographs were provided and were analyzed via MATLAB. The pixel intensity was measured throughout the length of the part where an intensity value of 0 equated to a smooth surface and an intensity value closer to 255 referred to a section of discoloration or a defect in this case. As the image analyzer scanned a region with defects, the pixel intensity value would rise towards 255 and return towards a value of 0 once it arrived at a section with no defect. The oscillatory behavior of these pixel intensity values was then classified as the appearance of defects, while a scan with no oscillation was considered a smooth and defect-free part.

Material Characterization

Netzsch DSC214 Polyma was used to determine the glass transition temperature (T_g)of the respective composite by heating up to 300°C at 5 $\frac{K}{min}$. Samples were tested to ensure 240°C was an appropriate processing temperature in which the onset and peak of the endotherm were measured using Proteus software to determine the glass transition region. The TA Rheometer AR 2000EX was used to conduct stress sweeps and relaxation experiments to quantify the machine learning model's input parameter.

Machine Learning Algorithms

Logistic Regression (LR) and Support Vector Machine (SVM) algorithms were used as baseline models for exploratory data analysis to establish a basic understanding of the relationship between the parameters and the occurrence of surface defects [52-53]. Since both models are linear regression-based models, the learned weights were used to indicate the significance of the corresponding parameters. This interpretation was further supported by the domain knowledge on injection molding and served as a parameter selection process for neural network input. Although neural networks are robust, they do not guarantee the physical interpretability of the model, which may intake redundant or noisy information from the dataset but still converge to local minima. Therefore, selecting parameters using a much simpler model before sending the parameters to the neural networks can be viewed as a method to incorporate prior knowledge that constrains the neural network and drives model interpretability and consistency with the physical intuition.

2.3 Methodology

When working with neural networks, the input parameters must influence the outcome. If the outcome is independent of the input parameter, noise results from it, and backpropagation becomes a computationally heavy process that may decrease your prediction accuracy. Determining the input parameters was done by conducting rheological tests and a literature review to ensure that each input parameter was influential to the outcome. Additionally, a Dimensional analysis, also known as Buckingham Pi-Theorem, is a procedure that reduces the input variables of a system by grouping them to create dimensionless numbers. Considering *m* physical quantities governed by *n*, the number of fundamental dimensions present in those physical quantities, one can reduce the system to a set of (m – n) independent dimensionless groups [54]. This analysis technique provides

a method for determining what properties may drive the occurrence of surface defects. As mentioned above, a Differential Scanning Calorimetry (DSC) test was conducted to ensure that the melting temperature was well below the processing temperature of 240°C. Once confirmed that the processing temperature was suitable, 240°C was used with all the rheological measurements, which also corresponded to the temperature used in injection molding trials.

Furthermore, a relaxation test consists of a step shear strain input regarding relaxation tests while logging the shear stress response with respect to time. The corresponding relaxation time is the time required for the stress response to reach 1% of the max stress response experienced at the beginning of the input strain [55]. To ensure full contact throughout the measurement, it is crucial to select a proper shear strain input to prevent slippage.

The TA Rheometer AR 2000ex was then used to conduct stress sweep tests at 240°C with an oscillatory torque input sweeping from 100 μNm to 700 μNm at an input frequency of 1 Hz. These tests highlighted the strains needed to reach a non-linear range and a range in which slippage occurred. Once all measurements were completed with 5 repetitions per sample to ensure proper reproducibility, the smallest strain percentage was then selected, and half of that value was to be used as the input strain percentage for the relaxation tests. The preliminary experiments showed that all relaxation tests would be conducted at 240°C and with a shear strain input of 0.25% to prevent slippage between plates, where Figure 9 shows a relaxation test for a given material. The figure on the right illustrates the normalized plot, and the relaxation time is defined as the time needed for the normalized stress to reach 0.01, 1% of the maximum shear stress.

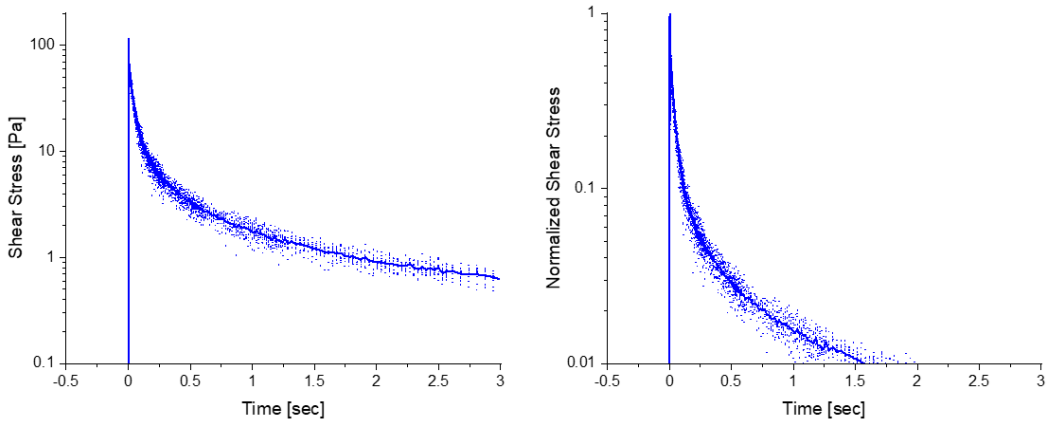

Figure 9. Example of relaxation tests and its normalized version

Once all the materials provided by SABIC were characterized, the next goal would be to use SVM and LR models as a method for quantifying how influential each parameter is to creating surface defects. The weights assigned by these models give insight about which parameters are the most influential and help determine the optimal neural network structure by including nodes that have a significant weight assigned to it. Once the quantity of input nodes are selected, the neural network architecture needs to be created to train, validate and test with experimental data.

Bayesian optimization was used to determine the optimal neural network structure to prevent a random assortment of iterations. Unlike the grid search or random search [56] methods where the hyperparameters are determined by either an exhaustive (grid search) or random (random search) tryout of the searchable space, Bayesian optimization incorporates Gaussian processes to model the probability distribution (mean and variance) of the model performance at any given set of hyperparameters [57]. At each iteration, the optimization algorithm proposes a new set of hyperparameters using the Gaussian process prior calculated from the existing data and evaluates the model performance using the proposed hyperparameters. One of the significant advantages of Bayesian optimization is its tendency to converge to the optimal hyperparameters with fewer computational resources and less time compared to the grid search method. The random search method may outperform Bayesian optimization, but there is usually a lack of information to narrow down the search space due to the complete random process of selecting hyperparameters. In this study, the number of hidden layers and neurons was altered to optimize the model architecture. The optimal hidden layer structure would then be applied to the neural network to validate and test the overall network performance.

24 samples were set aside as the testing data, which were not used during model training or validation. The remaining 213 samples were used for NN model development. These samples were first divided into a training set and a validation set for hyperparameter tuning. After the optimal NN architecture was obtained, the same samples were used for a more robust evaluation of the model performance through cross-validation (CV). To test how the proposed NN architecture performs on new data, the model was retrained on all the training and validation samples, and the test data set aside earlier were used to calculate the prediction accuracy.

Keras Tuner (version 1.0.1) was used to realize the process of hyperparameter tuning with Bayesian optimization described above. Tensorflow (version 2.0.0) with Keras API was used to build the neural network models.

2.4 Results and Discussion

Dimensional Analysis

Dimensional analysis (DA) is a technique capable of highlighting parameters that are influential in the specific system. This system is made up of eight (m) input variables and four (n) basic dimensions, as seen in Table 2 below. With u, k, μ and ρ being the repeated variables, this dimensionless analysis results in five dimensionless number or Pi-groups related to this process. Equations 5-13 depict the overall process of how the final Pi-group is determined. Equation 1 shows how the first Pi-group comprises the repeating variables raised to a unique exponential power multiplied by one of the non-repeated variables, T.

Table 2. Parameters used for the dimensional analysis.

Variable	Symbol	Dimension
Fluid Viscosity	μ	$\frac{M}{LT}$
Thickness of Plate	t	L
Length of Part	l	L
Injection Speed	u	$\frac{L}{T}$
Process Temperature	T	θ
Melt Density	ρ	$\frac{M}{L^3}$
Relaxation Time	λ	T
Thermal Conductivity	k	$\frac{ML}{T^3\theta}$

$$\Pi_1 = Tu^a k^b \mu^c \rho^d \tag{5}$$

The basic dimensions replace the variables, and the exponential power constant remains in each.

$$\Pi_1 = \theta \left(\frac{L}{T}\right)^a \left(\frac{ML}{T^3\theta}\right)^b \left(\frac{M}{LT}\right)^c \left(\frac{M}{L^3}\right)^d \tag{6}$$

Afterward, each fundamental dimension is raised to the zeroth power on the left side of the equation, and the right side of the equation includes each fundamental dimension raised to the power of a combination of all the unique constants present in each repeating variable.

$$M^0 L^0 T^0 \theta^0 = M^{b+c+d} L^{a+b-c-3d} T^{-a-3b-c} \theta^{1-b} \tag{7}$$

Finally, we can solve for each exponential constant as there are 4 equations and 4 unknowns, where one of the equations can be seen below.

$$M^0 = M^{b+c+d} \rightarrow 0 = b + c + d \tag{8}$$

After solving the linear system of equations, each exponential constant is solved and is shown below in equation 9.

$$a = -2, b = 1, c = -1, d = 0 \tag{9}$$

This ultimately allows us to compile our first Pi – group, which can be rearranged to represent the Brinkman Number, a parameter that characterizes the viscous dissipation of a material experiencing flow (Equation 11).

$$\Pi_1 = Tu^{-2}k^1\mu^{-1}\rho^0 = \frac{Tk}{u^2\mu} \tag{10}$$

$$\frac{\mathbf{1}}{\mathbf{\Pi_1}} = \frac{u^2\mu}{Tk} = \mathbf{Brinkman\ Number} \tag{11}$$

Furthermore, the remaining Pi-groups can be determined using the technique mentioned above and can be seen below.

$$\Pi_2 = tu^1k^0\mu^{-1}\rho^1 = \frac{tu\rho}{\mu} \tag{9}$$

$$\Pi_3 = \lambda u^2k^0\mu^{-1}\rho^1 = \frac{\lambda u^2\rho}{\mu} \tag{10}$$

$$\frac{\mathbf{\Pi_3}}{\mathbf{\Pi_2}} = \frac{\lambda u^2\rho}{\mu}\cdot\frac{\mu}{tu\rho} = \frac{\lambda u}{t} = (\mathbf{Deborah\ Number})\mathbf{u} \tag{11}$$

$$\mathbf{\Pi_4} = lu^1k^0\mu^{-1}\rho^1 = \frac{lu\rho}{\mu} = \mathbf{Reynolds\ Number} \tag{12}$$

Upon review, the Deborah number appears in $\frac{\mathbf{\Pi_3}}{\mathbf{\Pi_2}}$ and gives us an inclination that this is a crucial parameter in this system. The Deborah number considers rheological and processing parameters in the system; therefore, these results support the hypothesis that rheological data is crucial for the development of an accurate NN.

SVM and LR Model

Both the SVM and LR models agreed on which parameters were the most influential for these models. Table 3 below shows the weights assigned to each respective input parameter where the larger weight values relate to a more considerable influence on surface defect prediction. Given our input parameters, both models indicate that elastomer content and gate geometry are the least influential, while the processing agent content, MFI, comonomer content, and injection speed are the most influential regarding this aesthetic defect.

Table 3. SVM and LR results depicting weights assigned to input parameters based on the influence.

Input Parameter	LR Weight	SVM Weight
Processing Agent Content	0.207	0.416
Comonomer Content	0.198	0.397
MFI	0.185	0.375
Injection Speed	0.128	0.260
Gate Geometry	0.030	0.062
Elastomer Content	0.008	0.014

This model is not stating that elastomer content and gate geometry is not an influential parameter of the injection molding process since it has been proven that selecting the gate geometry is instrumental in designing the injection molding setup as it brings about burn marks [58], delamination [59], flash [60], jetting [61], sink marks [62], weld lines [63] or warpage [64]. It is also known that a more restrictive opening leads to the increase of principle stress differences [54]. These models purely state that both parameters are not as influential when creating the model and that other parameters, such as processing agent content, are more influential in these models. Additionally, given that MFI is a rheological parameter, relaxation time was assumed to be an influential parameter and allowed testing to begin on the parallel plate rheometer.

Validation of Support Vector Machine and Logistics Regression Parameters

Upon analysis of the injection-molded plates containing the processing agent, it was evident that the surface defect formation was significantly reduced with increased injection speed. Figure 10 depicts the overall trend of defects from injection-molded plates as you increased injection speed.

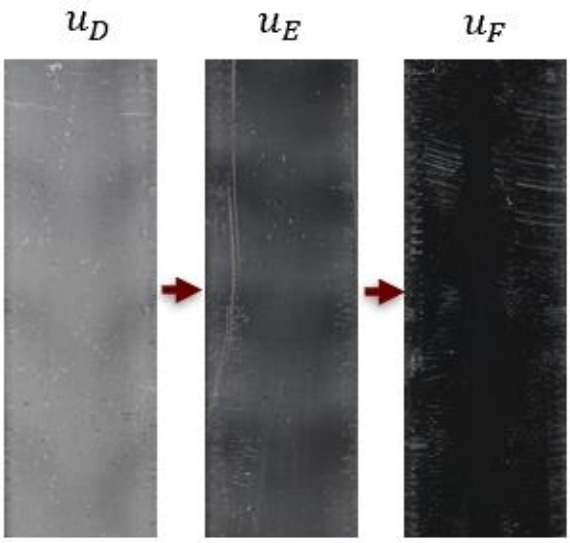

Figure 10. Images of samples processed at varying processing speeds with processing agent.

The processing agent is a common injection molding additive used to improve the polymer's flowability by breaking down the polymeric chains. The degradation of polymeric chains reduces the molecular weight distribution of the material, and as proven by Tzoganakis and coworkers, this shift in molecular weight distribution leads to an increase in melt flow index [65]. The increase in melt flow index may be acquitted to the decrease in shear viscosity, confirmed by Ghosh and coworkers, where an increase in this agent content leads to a decrease in viscosity. Moreover, it was studied that the increase of processing temperature leads to the further reduction of shear viscosity [66].

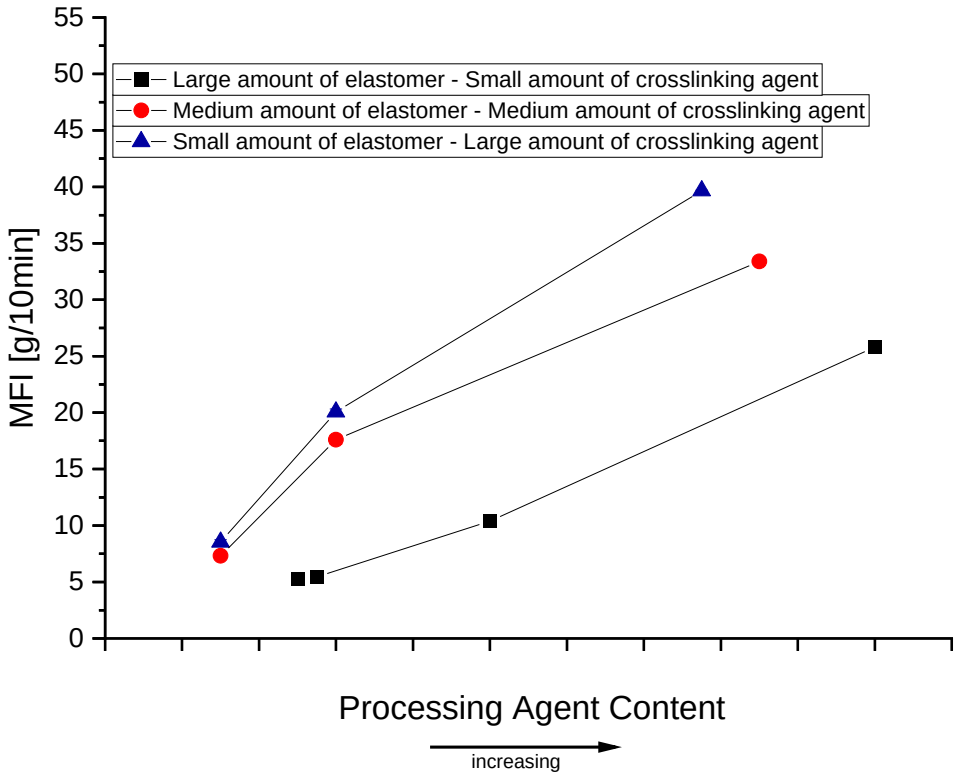

Figure 11. Tests showcasing the increasing effect of processing agent on MFI.

A decrease in chain lengths, from the processing agent, results in decreased relaxation time as the chains can slide past one another more freely with such additive. This effect is visible in Figure 12, where an increase in processing agent content reflects a decrease in λ, relaxation time.

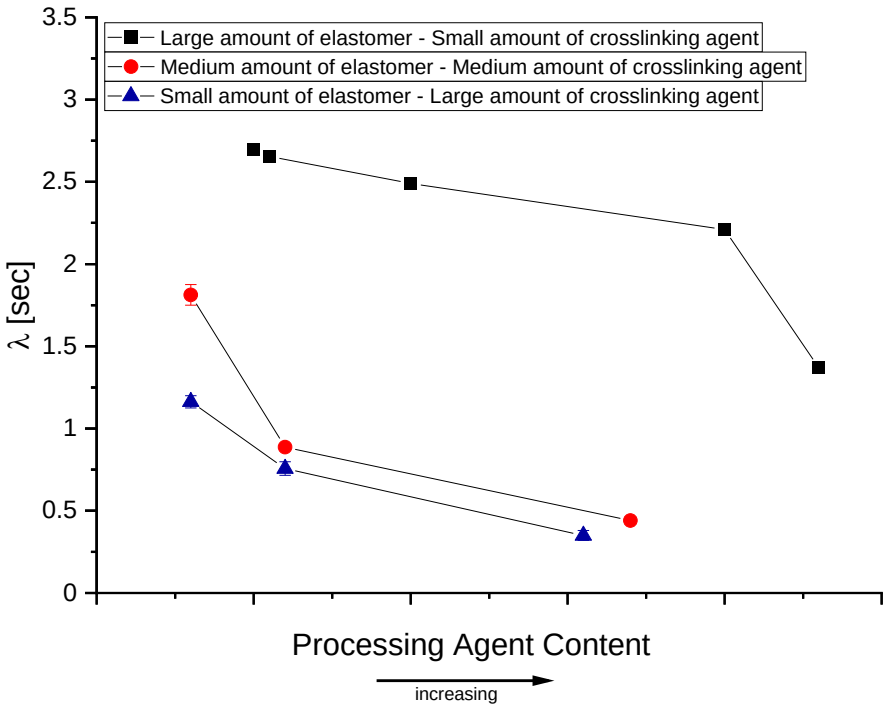

Figure 12. Relaxation tests showing the decreasing effect of processing agent on λ.

Higher stresses are present at higher processing speeds, and with elastomer being present in the system, the high tanδ of elastomer leads to increased dissipation of energy while being under shearing stress [67]. A high tanδ translates to a large loss modulus given a fixed storage modulus. This means that it can absorb energy and dissipate it in other forms. This dissipation of energy translates to the expulsion of heat caused by increased energy inputted into the system. As stated before, the change in the system's thermal state results in the further reduction of viscosity because of the processing agent effect. This decrease in viscosity, resultant of the increase in velocity, halts the creation of these aesthetic defects. This confirms the validity of including processing agent content as an input parameter to the neural network as a change in agent content can reduce the viscosity and further reduce viscosity if processing speeds are increased.

Large amounts of comonomer within the model blend correspond to higher viscosities at the specific processing temperature. This behavior is apparent in Figure 13, where the x-axis is the comonomer content increasing left to right, the y-axis is the relaxation time, and the red box plots represent unique experiments with varying comonomer content.

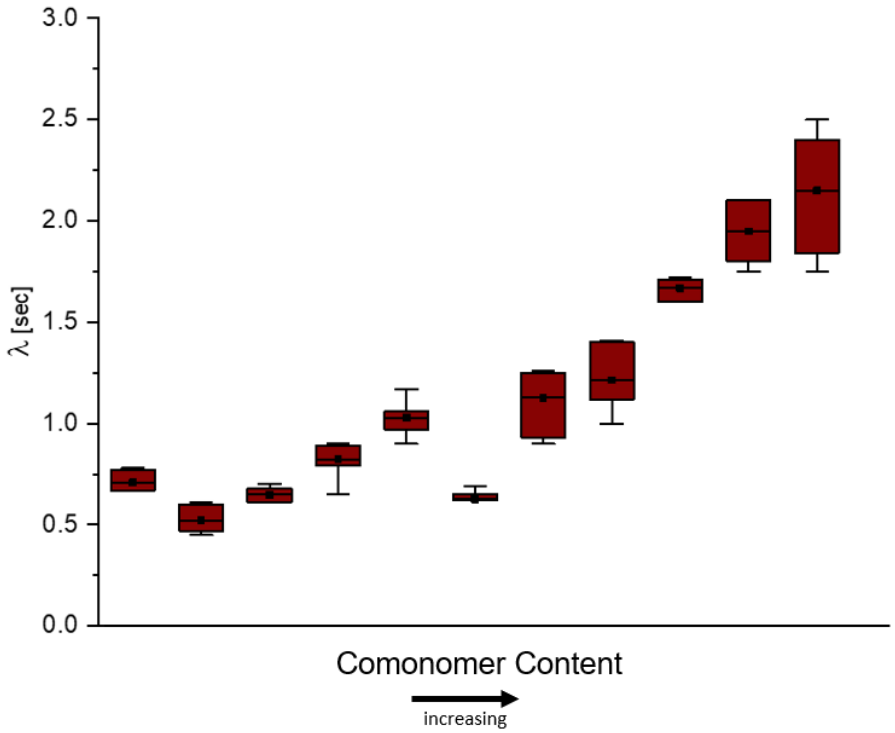

Figure 13. Relaxation tests results showing the positive influence of comonomer content on λ.

This increase in relaxation time suggests that the material experiences increased viscosity with comonomer content, and higher stresses are present for the given strain input. This observation was logged in the preliminary stress sweep experiments where the stress response was plotted against strain %; we can then calculate the slope and relate those slopes to subsequent samples. Table 4 highlights the following observation of increased stress response with corresponding strain input solidifying the fact to include comonomer content within the machine learning algorithms.

Table 4. Results showing that an increase in comonomer content results in the material's inability to deform.

Comonomer Content [%]	Slope [%]
increasing ↓	52
	43
	61
	67
	71
	121

Additionally, it was observed that defects appeared as you increased injection speed when the processing agent was not present. The increase in velocity did not permit sufficient time for the model blend to relax, resulting in rheological instabilities, thus bringing about surface defects.

Preliminary Machine Learning Iterations

The preliminary SVM and LR model allowed for a quantitative method for assessing this dataset's ability to use a classification machine learning algorithm. SVM and LR captured the complex occurrence of these surface defects with 73% classification accuracy. They served as a baseline study for determining the influential parameters in this system, which would ultimately be used for the successive deep learning neural network.

With the SVM and LR model determining that gate geometry and elastomer content were the least influential input parameters, it was crucial to determine if both input parameters introduced noise to the system and reduced the convergence rate. For this reason, MATLAB was used to run the optimizable SVM learner to determine how reducing the number of input nodes altered the classifier's performance. Table 5 below shows the results of the 8-fold cross-validation (CV) tests where test 1 includes all seven input parameters, test 2 includes all seven input parameters except for gate geometry and elastomer content, test 3 includes all seven parameters except for gate

geometry, elastomer content, and relaxation time, and test 4 includes all seven input parameters except for gate geometry, elastomer content and MFI.

Table 5. 8-fold cross-validation accuracy reached with partial input parameters.

Test	CV accuracy [%]
1	85.9
2	86.9
3	84.0
4	85.4

Test 2 resulted in achieving the highest classification accuracy and corroborating with the initial SVM and LR weights where it stated that gate geometry and elastomer content were not as influential for this machine learning algorithm. Additionally, the SVM classifier's confusion matrix can be seen below (Figure 14) and shows how most of the misclassification in validation occurs in predicting the "no surface defect."

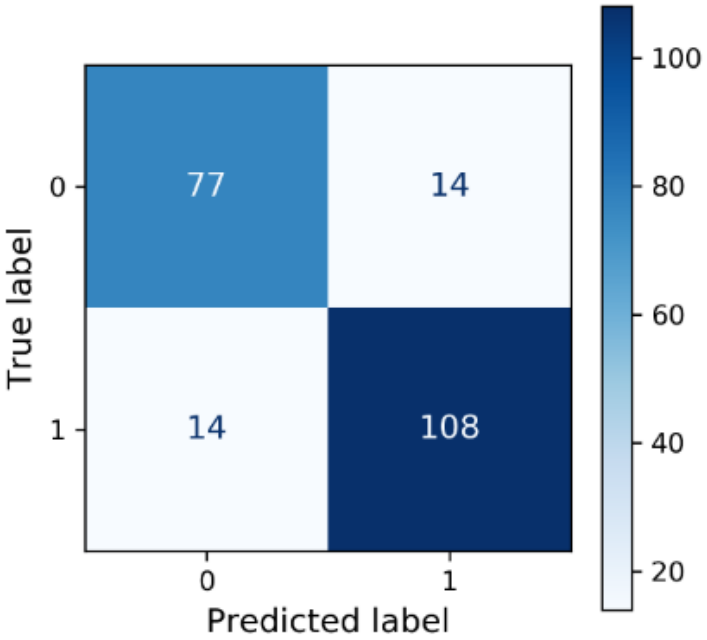

Figure 14. The confusion matrix of the optimized SVM classifier

Final Neural Network Testing

Applying what was observed in SVM and LR to the NN structure, two tests were conducted to validate the hypothesis that eliminating gate geometry and elastomer content would improve the NN accuracy. Test 1 would include all input parameters, while test 2 would include all input parameters except for gate geometry and elastomer content. The NN structure would then be optimized with Bayesian optimization, where Figure 15 depicts the NN architecture for test 1 after optimization, and Figure 16 shows the overall NN structure for test 2 after Bayesian optimization. The tuned hyperparameters include a number of hidden layers (1 to 4), number of hidden nodes (32 to 256), and data normalization method (none, normalization, or standardization). The weights were initialized using the Glorot uniform initializer (Keras default), drawing samples from a random uniform distribution within a limit; the biases were initialized as zero [68].

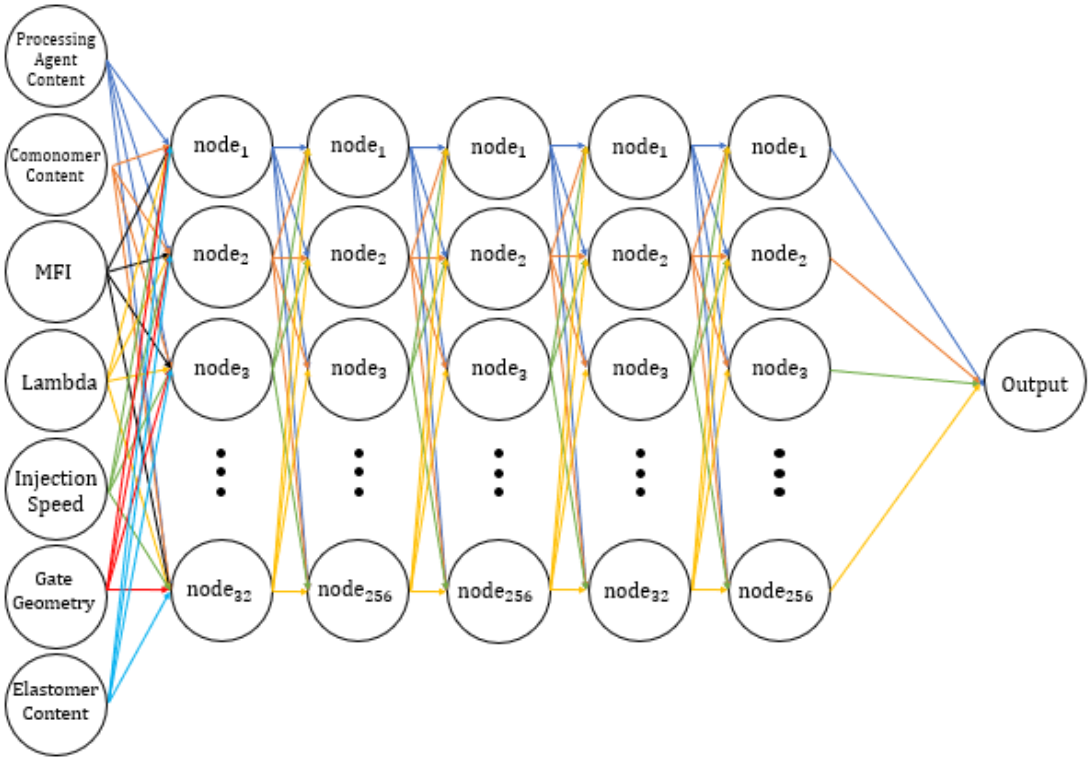

Figure 15. The neural network architecture for test 1 after Bayesian optimization

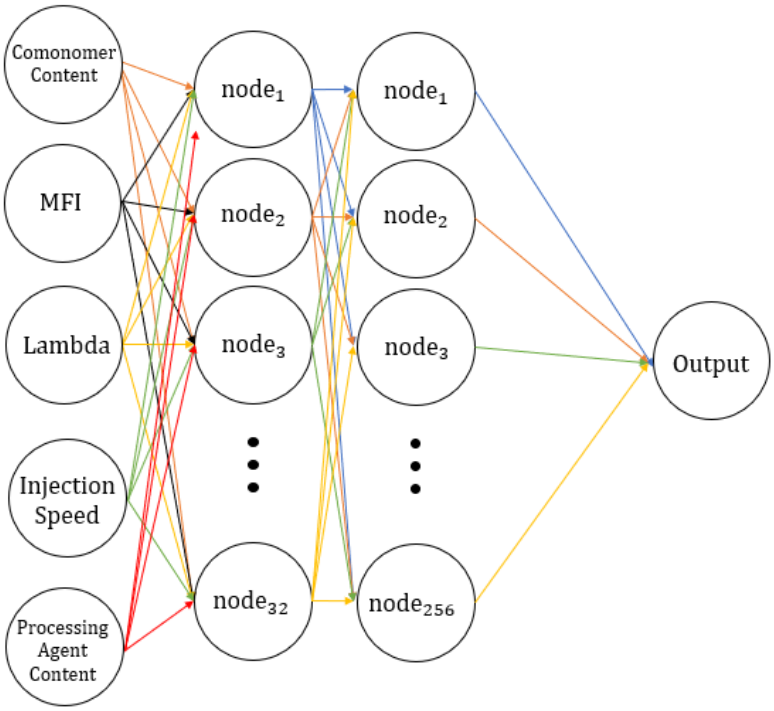

Figure 16. The neural network architecture for test 2 after Bayesian optimization

From the Bayesian optimization, although the optimized NN has a simple architecture with only 2 hidden layers, it achieved an improved 8-fold CV accuracy of 90.2%±4.4%. The trained model's ability to generalize to new data was tested using the test dataset that was set aside during training and CV. The test accuracy reached 90.5% (precision=91.7%, recall=91.7%), with only 1 misclassified data entry in each class, as summarized in the confusion matrix in Figure 17.a. When using all data inputs, the optimal NN architecture exhibited increased complexities, with 5 hidden layers and more hidden neurons than the NN architecture with reduced feature selection, resulting in a total of 91,425 trainable parameters. The 8-fold CV accuracy is 92.4%±11.4% (Figure 17.b). Although the average CV accuracy increased slightly, the error range almost tripled, indicating a higher tendency of overfitting. The test accuracy stayed the same with a value of 90.5% on the same test samples (precision = 85.7%, recall=100%).

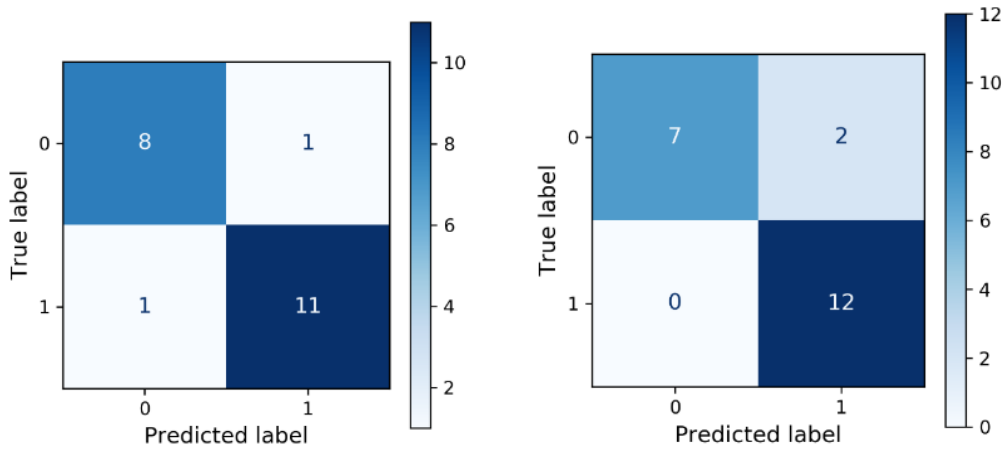

Figure 17. The confusion matrix for test (left) 1 and (right) test 2

Sensitivity analysis was also performed to obtain the gradients of the neural network output with respect to the test samples' input features using backpropagation. The calculated gradient value suggests how a change of input features may change the output, with a more positive and larger gradient contributing more to the occurrence of surface defect and vice versa. As depicted in Table 6 below, on average, comonomer content, processing agent content, and rheological parameters illustrated greater contributions to the NN output than the other features, similar to what was observed in the SVM and LR analyses.

Table 6. Sensitivity analysis results

Input Parameter	**NN Gradient**
Elastomer Content	$2.40 \cdot 10^{-5}$
Comonomer Content	$-4.30 \cdot 10^{-4}$
Processing Agent Content	$9.09 \cdot 10^{-5}$
Injection Speed	$-4.35 \cdot 10^{-5}$
Gate Geometry	$-6.26 \cdot 10^{-5}$
Lambda	$9.10 \cdot 10^{-5}$
MFI	$4.37 \cdot 10^{-5}$

3. Materials Development Optimization via Data-Driven Modeling

3.1 Introduction

The use of naturally derived or sustainable polymers is continuing to gain increasing attention due to the long-term environmental harm that their synthetic analog imposes. These synthetic polymers over the last few decades have become the most practical and economical solution for a huge variety of applications across multiple industries given their cost savings [69-71]. Industry now is being encouraged to embrace polymers that create a negative carbon footprint. An example of such a biopolymer is natural rubber, which is derived from the *Hevea Brasilensis* tree as latex [72-75].

With the appropriate additives, natural rubber can be manipulated to acquire distinct properties for specific applications. Previous studies have shown how increasing sulfur content increases crosslink density and hardness, leading to a less viscoelastic material [76-78]. From these studies, Zhao and coworkers were able to demonstrate that the Shore A and 300% modulus of NR vulcanizates both increased linearly with crosslink density, but dynamic properties still vary in a non-linear fashion [76]. Plasticizers are another commonly used additive in charge of decreasing viscosity and improving processability, meanwhile decreasing tensile properties, tear strength, resilience, and compression set [79-81]. Furthermore, regarding lightweighting, sodium bicarbonate is an additive commonly used for such applications as the elevated temperatures during vulcanization trigger degradation of the additive, resulting in the release of carbon dioxide. The release of gasses within the blends creates the foaming effect where a porous inner structure is produced [82-83]. It is important to recognize that introducing a foamed structure to a testing

specimen under compression behaves very differently from a foamed testing specimen under tension. The act of compressing testing a foamed polymer structure results in an atypical compression curve where there are three zones, the initial zone with a higher tangent modulus, the elastic buckling zone, and the densification zone. The densification region is where the cellular structure begins to collapse on itself, and the stresses begin to grow as gas and polymer are compressed.

It is also important to note that all additives have interacting effects and that varying chemical grades also bring about variation to your blend material properties. The sensitivity of material properties due to additives is a complex issue that deems formulating blends a highly complex task. For that reason, this study focuses on data-driven modeling within the formulation process.

With polymers exhibiting time and temperature-dependent behavior, it is crucial to quantify the long-term and short-term behavior of the polymer of interest to fully understand its material behavior. For that reason, viscoelastic properties (relaxation behavior and tan δ), hardness, and the quantity of voids in the sample were selected as the measured properties as they characterize the morphology, short-term behavior, and long-term behavior of polymers [55,67,84].

Relaxation measurements allow for long-term behavior analysis as it can also be interrelated to creep behavior [67,85-86]. Moreover, dynamic properties are crucial for understanding mechanical behavior for high-performance applications undergoing cyclical loading [87-90]. For example, footwear materials undergo cyclical loading between 1 Hz –5 Hz while materials within the automotive industry may experience cyclical loading within a frequency range of about 0 and 300 Hz [91]. Furthermore, it should be noted that with the automotive industry embracing the electrification of automobiles, it should be expected to encounter higher-frequency vibrations within the automobile, supporting the need to understand the frequency-dependent behavior of polymers implemented in automotive design [91]. Additionally, with foaming technologies entering high-performance applications due to their role in light-weighting, it is no surprise that the addition of air bubbles within a polymer matrix will alter material performance [83,92-93].

The above-mentioned material characteristics deem formulating a highly complex process as one additive may increase one material property but non-linearly decrease another. It is a process that requires the formulator to balance the interacting effects of all additives, while ensuring that the cost of the overall blend is minimized without sacrificing quality. This study will focus on

providing industry with three data-driven formulation methodologies, varying in complexity (Response Surface Method, Artificial Neural Networks, and Gaussian Process Regression) to explain how certain algorithms can offer additional information to the process besides treating the algorithm like a black box. The final goal of this study is to use the algorithms as a method for reverse engineering current materials based on their viscoelastic properties (relaxation, dynamic, and hardness). The reverse engineering aspect of this study is crucial for formulators as they can feed the algorithm a starting point to their design of experiments.

3.2 Materials and Characterization Methods

Material Compounding

SOAN Laboratories provided the Polymer Engineering Center (PEC) with Betapreno, one of their ammonia-free natural rubber (NR) materials produced in Victoria, Colombia. Table 7 below depicts the additives used within this study to understand the influence of commonly used additives on the mechanical behavior of natural rubber blends, primarily its viscoelastic properties. Blends were prepared in an internal batch mixer, C.W. Brabender 3-Piece bowl mixer, using Banbury blades. Table 8 below shows each blend prepared within this study, where the last two blends were outputted by the predictive algorithms as target blends, used to improve the prediction accuracy of the machine learning algorithm. All blends were mixed at 21 °C and 50 RPMs until a homogeneous mixture resulted in the plateau of the torque response logged by the Intelli Plasti-Corder Torque Rheometer mixer attachment. Additives were tested at varying load ranges to capture the effect of a low load amount to a large load amount. This was done to ensure the algorithm captures the limiting effect of an additive as properties do not always trend in the same manner as you increase the amount of additive [94-97]. Jacob and coworkers showed that increasing reinforcement increased the tensile strength of the natural rubber blend only if the loading was below 30 pph (parts per hundred of rubber) [13]. After exceeding 30 pph of fiber loading, the tensile strength would begin to decrease with fiber loading. Capturing this phenomenon is crucial as the algorithm needs to understand when loading becomes detrimental to certain properties. It is also important to note that only a small number of blends were created to prove that a small DOE (design of experiments), given the right data, will be able to aid in the creation of an accurate predictive algorithm.

Table 7. Materials employed within this study

Material	Provider	Purpose
Raw Natural Rubber	SOAN Laboratories	Raw Material
Sulfur	Fisher Scientific	Cross-linking Agent
Sodium Bicarbonate	Sigma-Aldrich	Foaming Agent
Stearic Acid	Fisher Scientific	Activator
Paraffin Oil	Fisher Scientific	Plasticizer
TMTD	Fisher Scientific	Accelerator
Zinc Oxide	Fisher Scientific	Accelerator

Table 8. Blend formulation DOE whereas each blend has 5 pph of Zinc Oxide, 1 pph of Stearic acid, 1 pph of TMTD and 8 pph of Sodium Bicarbonate.

Blend No.	Sulfur (pph)	Paraffin Oil (pph)
1	2.5	80
2	2.5	50
3	1.5	40
4	1.5	80
5	1.5	20
6	0.5	20
7	0.5	0
8	2.5	0
9	4	0
10 *	0.6	39
11 *	0.3	59

* These are blends outputted by the ANN algorithm to improve accuracy.

Rheological Characterization

A TA Instruments AR-2000EX parallel plate rheometer was employed to quantify the vulcanization reaction of each natural rubber blend. By using the ASTM D2084 standard, the reaction was characterized to determine the optimal vulcanization time, t_{90}, at 150 °C. Furthermore, to prevent slippage-induced measurement error, parallel plate rheometry was conducted using serrated parallel plates. After rheological testing, the samples were placed in cylindrical molds and vulcanized in the Carver 3889 compression molding machine.

Lissajous Curve Characterization

The NETZSCH Eplexor® 500 N Dynamic Mechanical Analyzer (DMA) was utilized for the characterization of Lissajous curves to extract the tan δ for each specific sample. For this dynamic study, a 10% static compressive strain was imposed on a cylindrical sample with 10 mm diameter and 10 mm height, and a ±5% dynamic strain was applied at 1 Hz. The large levels of strains classify these testing conditions as a large amplitude oscillatory test (LAOS) which creates a valid representation of what stresses and strains are experienced during walking. The shape of the Lissajous curve gives us an insight into the level of non-linearity present when loaded cyclically, and also gives us the tan δ, a measurement represented by the lag between the stress and strain response during testing, correspondingly the ratio between the Loss Modulus and Storage Modulus.

Relaxation Curve Characterization

Similarly, to dynamic testing, relaxation behavior was characterized with the NETZSCH Eplexor® 500 N DMA by imposing a 30% compressive static strain for 10 min and logging the stress response from the material with respect to time. Strain of 30% was selected as the testing condition since 10% resulted in the same normalized curve, where a large signal-to-noise ratio is present, as seen in Figure 18. As the material is quickly loaded in compression to the predefined strain, the stress reaches the maximum point and begins to decay with time.

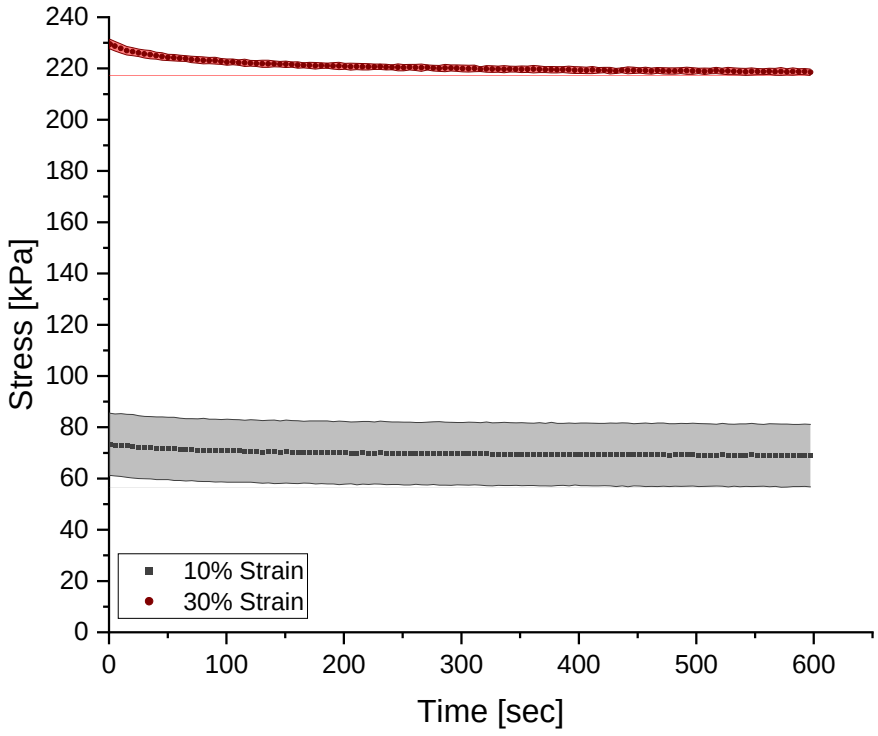

Figure 18. The 10% and 30% relaxation tests showcasing their respective signal-to-noise ratios.

Given that full relaxation of a cross-linked polymer is not frequently attainable at time scales below 10 h, as seen in Figure 19 below, characterization of the relaxation curve was done by tabulating the maximum stress during relaxation testing and by fitting the decay of the curve with a power function. Most polymers during relaxation can be modeled with a power function (Equation (10)) where n_{relax}, is used to quantify the rate at which stress decays [67]. By analyzing the magnitude of n_{relax}, it can be deduced that if a $|n_{relax}|$ is large, then the decay occurs more rapidly compared to a material with a smaller $|n_{relax}|$.

$$\sigma_{relax,normalized} = A \cdot time^{-n_{relax}} \quad (13)$$

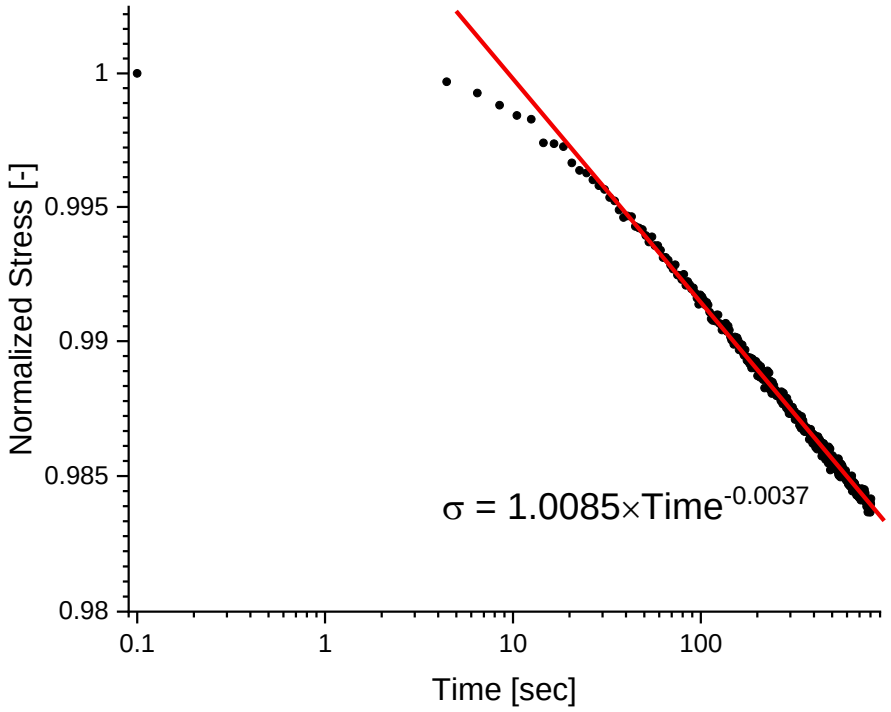

Figure 19. The method used to extract long-term material behavior from relaxation data

Morphological Characterization

Before mechanical testing, the ZEISS Metrotom 800 µCT (Carl Zeiss AG, Oberkochen, Germany) was used to scan the cylindrical specimen by using the scanning parameters mentioned in Table 9.

Table 9. µCT scanning parameters.

Variable	**Symbol**
Voltage [kV]	75
Current [µA]	100
Integration Time [ms]	1000
Gain [-]	8
Number of Projections [-]	1000
Resolution [µm]	4

Each scanned image represents a cross-section of the sample with pixel intensity values ranging from 0 to 255. A pixel intensity value of 0 corresponds to the color black while a pixel intensity value of 255 corresponds to the color white. A material with a higher density will have a much higher pixel intensity value compared to a void, which will output a lower pixel intensity value. A MATLAB program, as schematically shown below in Figure 20, was developed to threshold each image and to characterize the quantity of voids within each cross-section, allowing for a through-thickness analysis of each cylindrical sample.

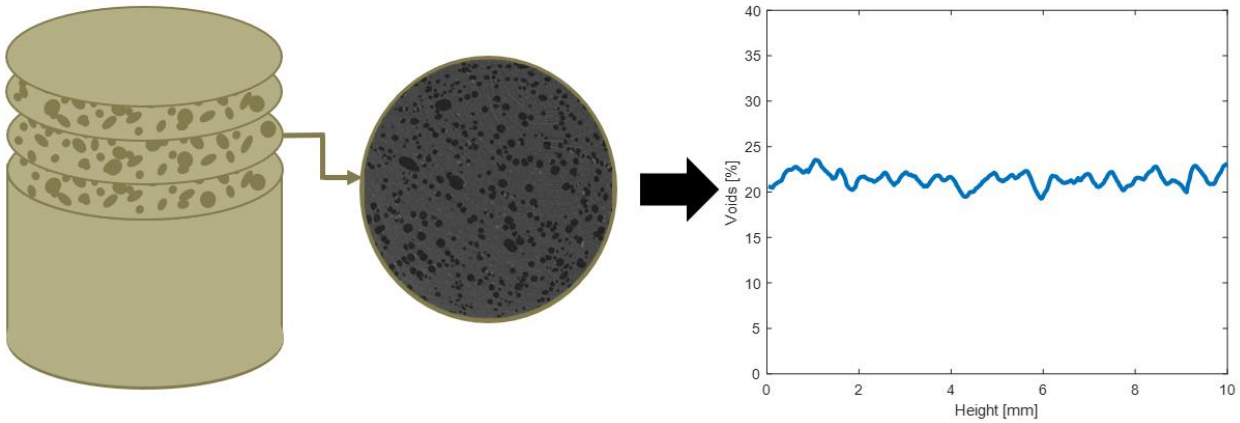

Figure 20. Workflow for the MATLAB program responsible for void analysis.

Durometer Characterization

A durometer (Shore A) was used to characterize the hardness of each respective blend. In accordance with ISO Standard D2240-15, this Type A indenter shape includes a flat cone point (0.79 mm), and a 35° included angle with a range of 0~100 HA.

3.3 Computational Methods

Linear Regression

Multivariate linear regression is one of the simplest models to construct a mathematical expression of the material property as a function of blend content. Each of the target properties—durometer reading, σ_{relax}, n_{relax}, and tan δ—is formulated by Equation (11):

$$Y = a_0 + a_1A + a_2B + a_3C \quad (14)$$

In the model above, A corresponds to sulfur content, B to paraffin oil content, and C to the void content within the sample; the coefficients (or weights and biases) a_i's are determined by ordinary least squares [16]. The model was implemented using Scikit-learn [98] (version 0.24.2) with Python.

Artificial Neural Networks

In this study, an ANN architecture was constructed using Tensorflow [99] (version 2.0.0) and tuned for each of the four material properties, including durometer reading, σ_{relax}, n_{relax}, and $\tan\delta$. To save experimental costs, the dataset for training and validation was kept relatively small, which contains 326 data instances. As a result, the hyperparameters of the ANN models were tuned with several considerations that avoid overtraining, such as the incorporation of dropout layers and early stopping as well as the leverage between the number of model parameters and cross-validation accuracy. To find the optimal set of hyperparameters, a grid search was performed. The grid search considers all the possible combinations of the discretized hyperparameters in the pre-constructed search space—including learning rate (0.001, 0.003, 0.01), number of hidden layers (1, 2, 3), and number of neurons (16, 32, 64, 128, 256)—and evaluates the model performance with each NN architecture. The model parameters were optimized using the mean absolute error and the Adam optimizer [100].

The gradient-based sensitivity analysis gives insight on the influence of individual blend content on each of the material properties. In the sensitivity analysis, the gradients of the output (each material property) with respect to the input (blend content) are computed and summarized for each input variable. The gradient values can indicate how blend content contributes to certain material performance, which may lead to human-informed design logistics for new materials.

Gaussian Process Regression

In this study, the GPR model was implemented using Scikit-learn [98] (version 0.24.2); a basic radial basis function (RBF) kernel was used, and the hyperparameters (length scale parameters) were optimized during data fitting. Again, 5-fold cross-validation was used to evaluate the model performance.

3.4 Characterization Results and Discussion

Influence of Voids on Viscoelastic and Static Properties

The degradation reaction of sodium bicarbonate within the blend has the ability of creating a foamed part with varying levels of void amount depending on the additive load and charge within the compression molding mold [8]. The micrographs seen in Figure 21 below show the three examples of void amounts captured by the ZEISS μCT scanner where the amount of sodium bicarbonate was kept constant and charge weight within the mold was altered.

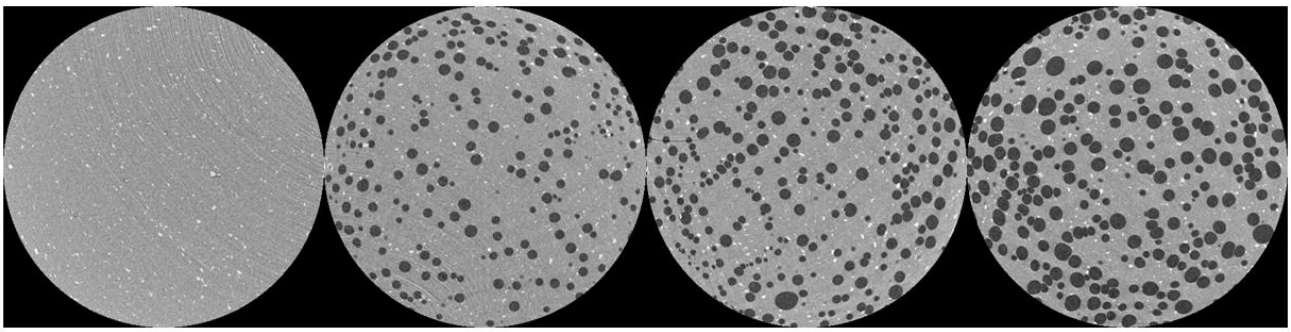

(a) **(b)** **(c)** **(d)**

Figure 21. (a) μCT scan of a sample with 0% voids. (b) μCT scan of sample with 11.8% voids. (c) μCT scan of sample with 19% voids. (d) μCT scan of sample with 32.2% voids.

It is evident that increasing void amount results in a decrease in solid material carrying load during testing [83,92-93]. For that reason, it is expected to see that a foamed structure consisting of the same formulation will result in a less rigid material, compared to one of lesser voids. Figure 22.a below shows the overlay of relaxation tests for the same formulation but at varying void contents and it can be observed that increasing voids results in a vertical shift of the overall curve. Furthermore, in Figure 22.b below, a clear linear relationship between the rigidity of the material and void amount can be seen if the maximum stress reached during testing is grouped with its respective void amount.

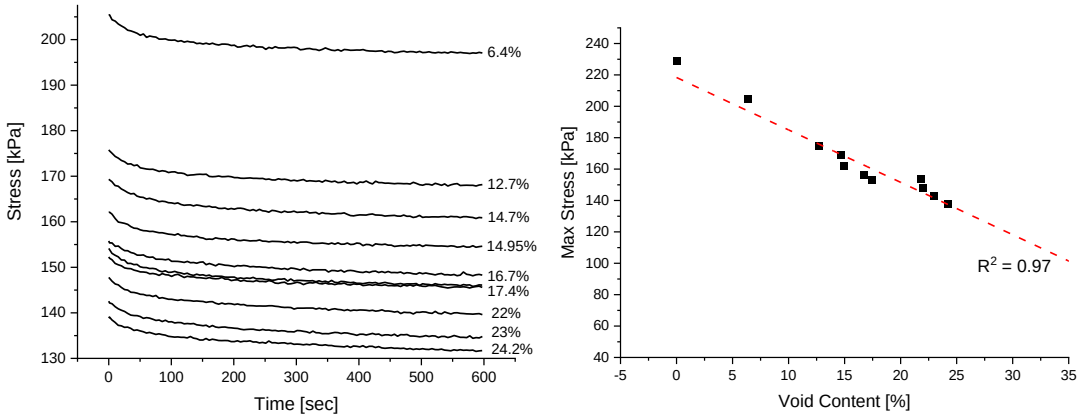

Figure 22. (a) An overlay of relaxation tests of blend 1 at varying levels of void content, and (b) the linear relationship between max stress experienced in relaxation testing and void content

It can be observed that the rate at which stress decays is also influenced by the quantity of voids. Therefore, evaluation the n_{relax} of individual curves allows for the study of how voids influence the rate of stress decay, whereas it can be seen in Figure 23 how voids and n_{relax} have a linear decreasing relationship. This relationship states that as the amount of voids increases, the rate at which stress decays will be larger.

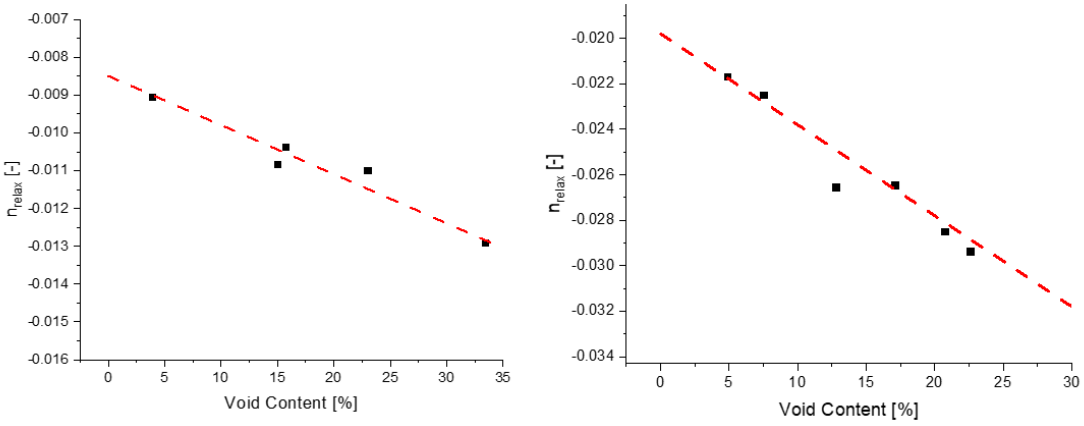

Figure 23. The relationship between voids and the rate at which stress decays for blend 9 (left) and 10 (right), characterized by n_{relax}.

To better understand at a quantitative level the amount of influence that parameters impose on a certain material property, the Pearson correlation coefficient is utilized to determine the level of significance between two specified variables. The coefficients are calculated using Equation 12 below and results in a normalized heat map.

$$r = \frac{\sum(x_i - \bar{x})(y_i - \bar{y})}{\sqrt{\sum(x_i - \bar{x})^2 \sum(y_i - \bar{y})^2}} \quad (15)$$

r = Pearson correlation coefficient
x_i = Values of the x − variable in a sample
$\bar{x}$ = Mean of the values of the x − variable
y_i = Values of the y − variable in a sample
$\bar{y}$ = Mean of the values of the y − variable

Figure 24 below shows the normalized heat map where a Pearson correlation coefficient closer to −1 translates to a highly significant decreasing effect on the specific property, a value of +1 translates to a highly significant increasing effect on the specific property, and a value near zero is interpreted as an insignificant parameter to the property of interest. There are three areas present within this heat map, the Input Blend Formulation coefficients which explain how the blends are not correlated with each other, the Output Material Property coefficients which dictate how each output property is interrelated with one another, and the Input Output Correlation coefficients that give insight into how additives influence the output viscoelastic properties. To mention a few, it can be seen that n_{relax} is negatively correlated with tan δ and that σ_{relax} is positively correlated with hardness of the material, captured by the durometer. It can be seen within the heat map that voids have a positive Pearson correlation coefficient value with tan δ, therefore it is expected to see the rise of tan δ with increased amounts of voids.

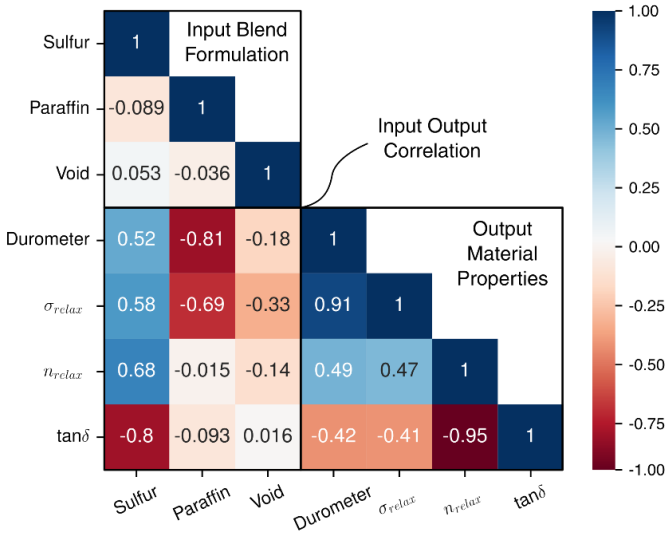

Figure 24. The Pearson correlation coefficients for each parameter.

The positive correlation of void content on tan δ specified by the Pearson correlation coefficient is confirmed in Figure 25.a below where blends 8 and 9 clearly show an increasing trend for tan δ as void content increases. The above-mentioned trend is present in all blends, allowing for the prediction of tan δ behavior for samples with zero percent void content to 40% void content by extrapolating data via linear regression techniques. As seen, the quantity of voids in the sample influences the stresses reached during relaxation testing, an indication of rigidity. This influence on rigidity is also captured in hardness measurements, a static method in which it can be seen that increasing void content results in a decrease in hardness. Figure 25.b below shows how hardness of blend 5 decreases in a linear fashion as void content increases.

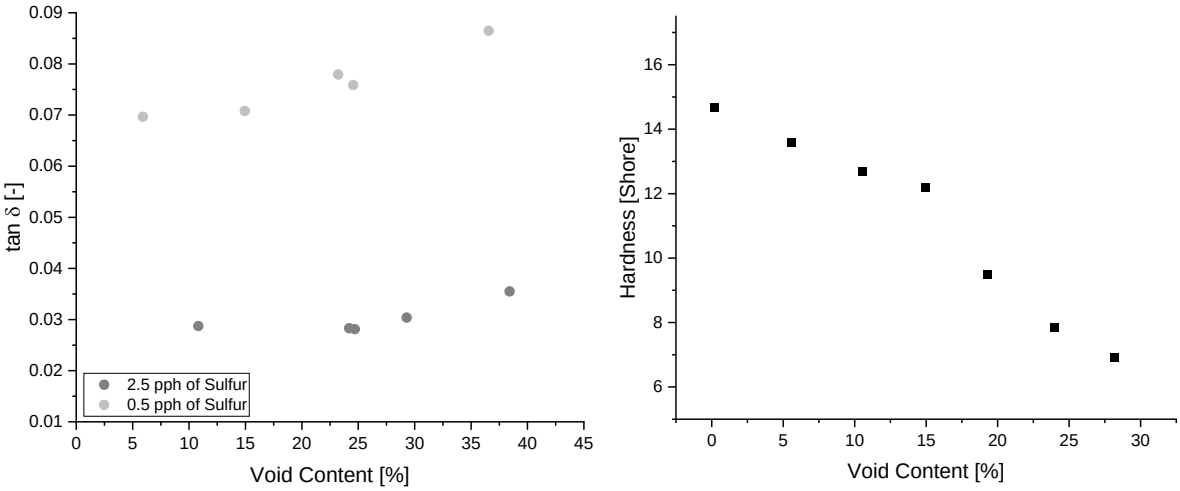

Figure 25. (a) The increasing relationship of void content on tan δ and (b) the influence of void content on hardness.

Influence of Sulfur on Viscoelastic and Static Properties

An increased amount of sulfur within results in increased number of cross-links, decreasing the ability for molecular chains to move past one another [55,101]. If mobility is limited, then intermolecular forces will be present, restricting full relaxation, and the lag between the strain and stress response will be minimized [55,84]. All three relaxation curves in Figure 26 below represent blends that only differ in the quantity of sulfur within the formulation. With no plasticizer present within the formulation, it can be appreciated how increasing the sulfur amount in fact increases rigidity, as seen in (a) where the blend with 4.0 pph of sulfur reaches a maximum stress 1.6 times

larger than the blend with 0.5 pph of sulfur. Moreover, observing the normalized relaxation curves in (b) proves how decreasing molecular mobility creates a material that experiences less relaxation decay behavior. A decrease in relaxation decay behavior, a consequence of increased crosslink density, indicates that such material will take much longer to reach 1% of the maximum stress, to a material with lesser sulfur quantity.

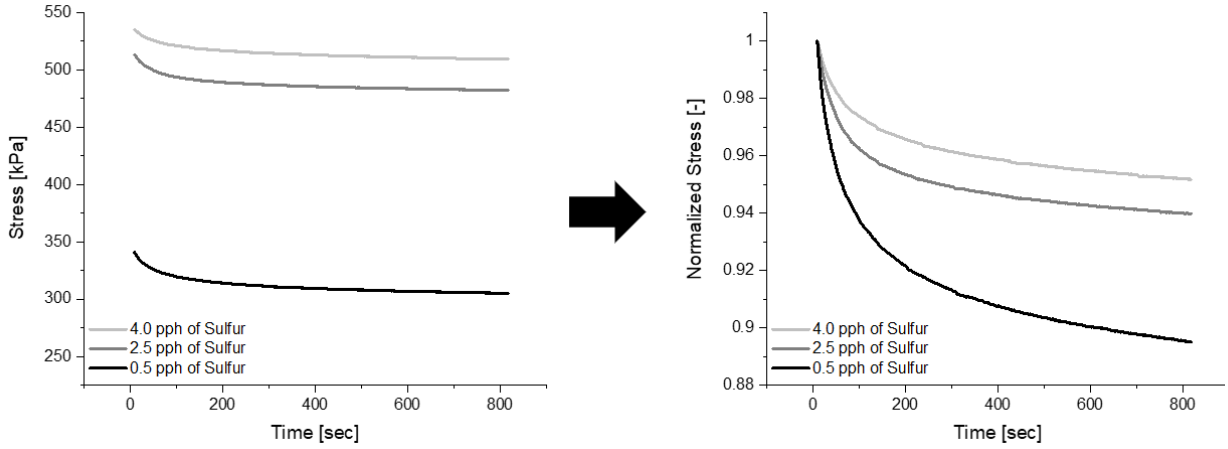

(**a**) (**b**)

Figure 26. (a) The relaxation curves for blends 7, 8 and 9 while (b) represents the normalized curves.

The blends mentioned in Figure 26 above did not contain plasticizer within the formulation and comparing blends with an equal amount of plasticizer with varying amounts of sulfur has the ability of creating a more complex material. It can be seen in Figure 27 below that increasing the sulfur load, for a blend with 80 pph of plasticizer, results in larger maximum stress reached during testing, but opposite to what was observed in Figure 26, the normalized relaxation curves do not follow the same trend. It is visible that increasing the sulfur amount from 1.5 pph to 2.5 pph, all with 80 pph of plasticizer has minimal influence on the rate at which relaxation occurs and a substantial effect on the rigidity of the material.

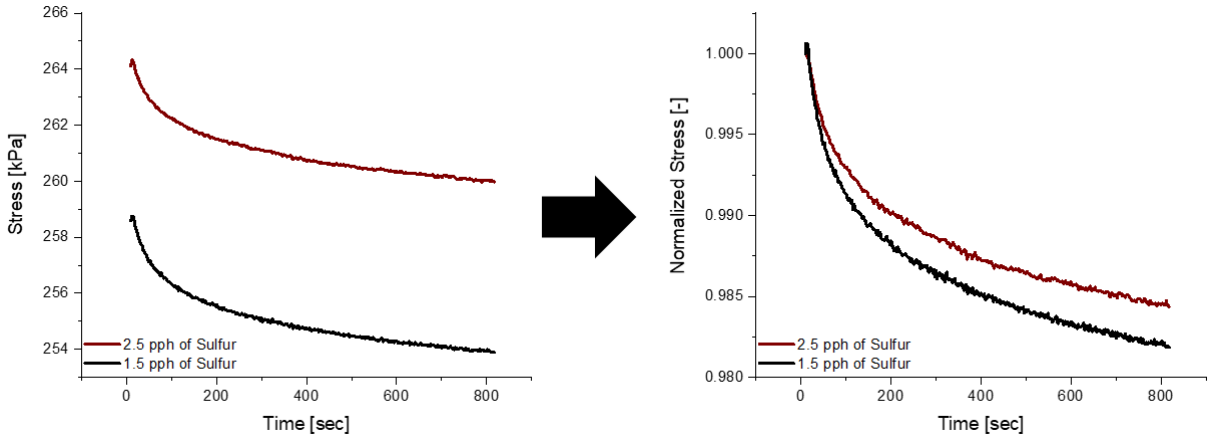

(a) **(b)**

Figure 27. (a) The relaxation curves for blends 1 and 4 while (b) represents the normalized curve, showing a large similarity in regard to the stress decay behavior.

With the Pearson correlation coefficient for sulfur on tan δ being −0.8, it is expected to see a decreasing trend on tan δ with increasing sulfur content. The expected trend can be appreciated in Figure 28 below where each blend has equal amounts of paraffin oil content but with varying sulfur content. A positive vertical shift in the curve can be appreciated as sulfur content decreases since it is known that heavily crosslinked polymers exhibit a decrease in molecular mobility [55,102].

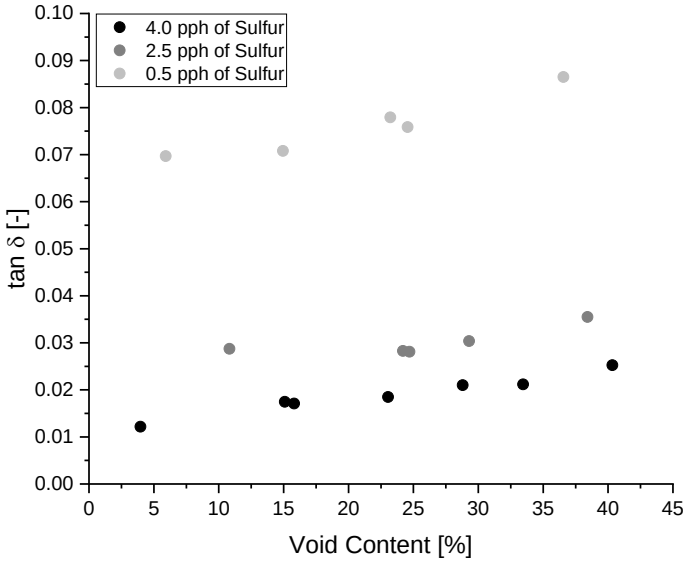

Figure 28. Tests showing the influence of sulfur content and void content on tan δ for blends 7, 8 and 9.

Influence of Paraffin Oil on Viscoelastic and Static Properties

Paraffin Oil is commonly used in the rubber industry to decrease the blend viscosity and to facilitate processing since the ultra-high molecular weight (UHMW) of natural rubber is extremely viscous [94,103]. At the given sulfur amount of 1.5 pph it is visible how the addition of paraffin oil creates a balancing effect to the stresses reached during testing. Unfortunately, this observation is not visible when the amount of sulfur is further increased to 2.5 pph of sulfur, the sulfur amount reaches a point in which it masks the effects of paraffin oil and limits the influence on rigidity. Figure 29 below shows the max stresses experienced during relaxation testing for blends with 2.5 pph of sulfur while Figure 30 shows it for a blend with 1.5 pph of sulfur. Sulfur and paraffin oil have competing effects on the rigidity of the material, and it can be noted by tabulating the slopes of stress decay for each set of data points that slopes differ in trend depending on the amount of sulfur content.

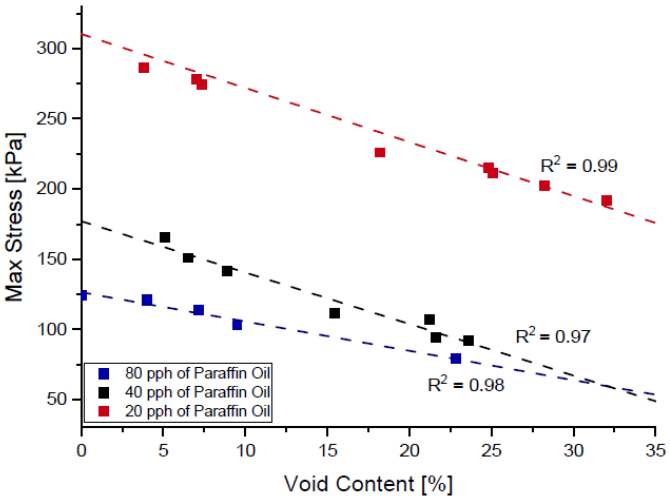

Paraffin Oil Content [pph]	Slope $\left[\frac{\text{kPa}}{\%\ \text{Void}}\right]$
20	−3.9
40	−3.7
80	−2.1

Figure 29. The relationship between paraffin oil content and σ_{relax} of NR blend with 1.5 pph of sulfur.

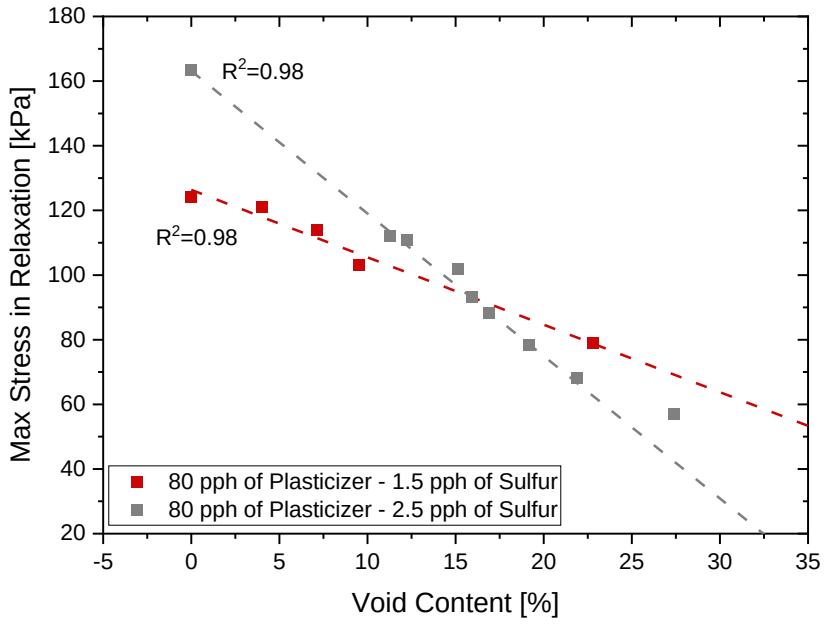

Figure 30. Plot describing the similarity of unique blends by varying void content.

The tanδ for blend 3–5, in Figure 31a below, show how paraffin oil has an increasing effect on tan δ until a threshold is reached. Once the amount of sulfur is increased from 1.5 pph to 2.5 pph, it can be seen in Figure 31b below that the increased sulfur amount overpowers the influence of paraffin oil, and the influence imparted by the plasticizer has an increasing effect on tan δ.

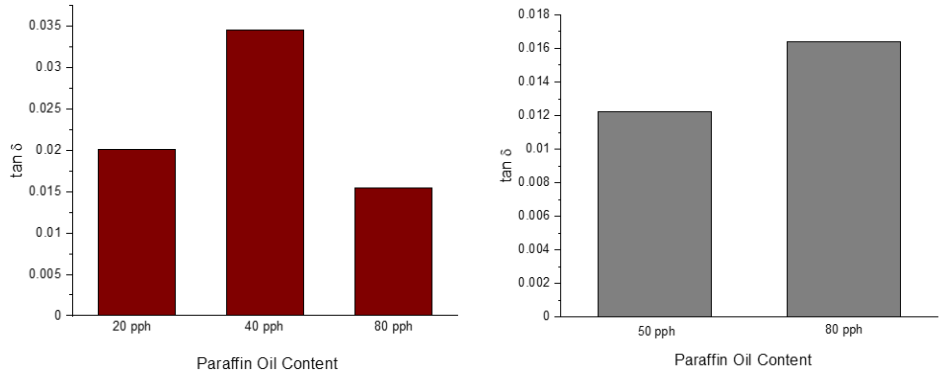

(**a**) (**b**)

Figure 31. The influence of paraffin oil content on tan δ for a blend with 1.5 pph (a) and 2.5 pph of sulfur (b).

3.5 Computational Results

Response Surface Method Prediction Results

Each output response has its respective model equation, as seen in Table 10 below, where each coefficient describes the level of influence that each linear, quadratic, and interaction parameter has on the performance of the system. With hardness and σ_{relax} during relaxation being closely interrelated to the rigidity of the material, a transient property, the models for both responses reach high prediction accuracies compared to the other two viscoelastic properties where time-dependent behavior is characterized. The RSM model created from only 11 blends results in an average Prediction R^2 of 0.89, and by comparing the proximity of each R^2 within each respective model, it is evident that overfitting is not occurring in this model given that there is no large variation between all three R^2 values.

Table 10. Results from the RSM analysis where each accuracy is shown, as well as the influential constants within the model.

Response Variable	Model Equation	R^2	Adjusted R^2	Predicted R^2
Durometer [Shore A]	$25.76 + 7.14A - 0.44B - 0.26C - 1.15A^2 + 0.002B^2 + 0.0001C^2 + 0.03AB + 0.01AC - 0.0005BC$	0.9689	0.9680	0.9667
σ_{relax} [kPa]	$440.12 + 268.26A - 10.80B - 9.90C - 26.37A^2 + 0.07B^2 + 0.01C^2 - 1.39AB - 2.94AC + 0.14BC$	0.9906	0.9903	0.9900
n_{relax} [-]	$-0.024 + 0.01674A - 0.00018B - 0.00049C - 0.003A^2 + 0.000001B^2 + 0.000008C^2 + 0.0000034AB + 0.000025AC + 0.000000BC$	0.7533	0.7463	0.7367
tan δ [-]	$0.119 - 0.0819A + 0.0004B + 0.00079C + 0.014A^2 - 0.000002B^2 - 0.000013C^2 - 0.000083AB - 0.000003AC - 0.000001BC$	0.8748	0.8712	0.8660

Standardizing the coefficients allows for the configuration of the Pareto Chart of the Standardized Effects where Figures 32-33 show the Pareto Chart for each respective output response within this study. A, B, and C all represent a controllable variable (factors), as seen in the legend on the right of each Pareto Chart. A linear term within the chart only includes one factor, such as A, representing the linear term of Sulfur. A quadratic term includes two factors, such as AA, and an interaction term within the chart is shown with two different factors, such as AB, which describe the interaction between Sulfur and Paraffin Oil.

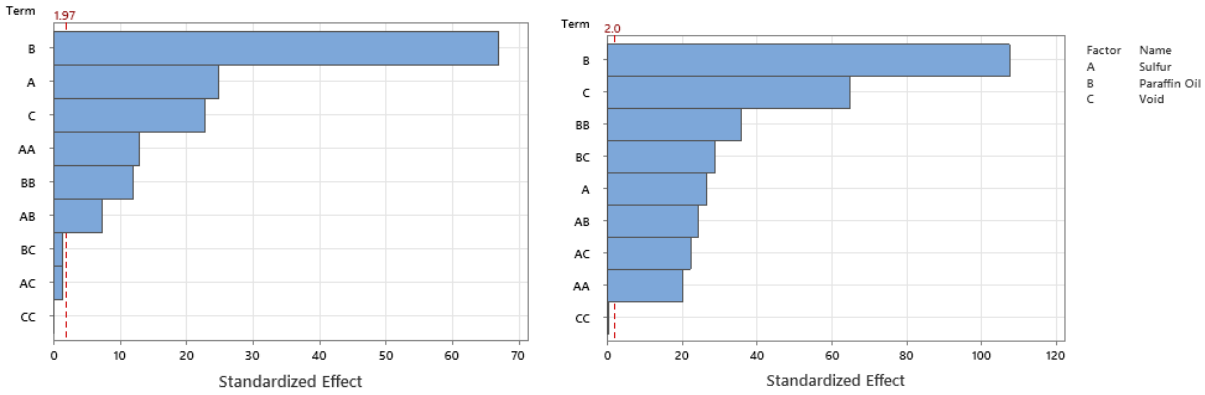

Figure 32. The Pareto Chart of Standardized Effects for (a) durometer reading and (b) σ_{relax}.

The Pareto chart for σ_{relax} and hardness both show that Paraffin Oil has the largest influence on the output response and that the response should closely follow a linear trend since the largest terms only have one factor. This linear relationship can be confirmed by looking at Figure 29 above where the linear trendline is present with an R^2 of 0.99. Observing the Pareto charts for n_{relax} and tanδ both show how complex the model is as the top two most influential terms are quadratic terms. RSM suggests that if the coefficient of the squared term is significant, then one can conclude that the relationship between both controllable variables closely follows a curved response. This statement is supported in Figure 34 where the relationship of sulfur on n_{relax} does not follow a linear trend, but more of an asymptotic curve.

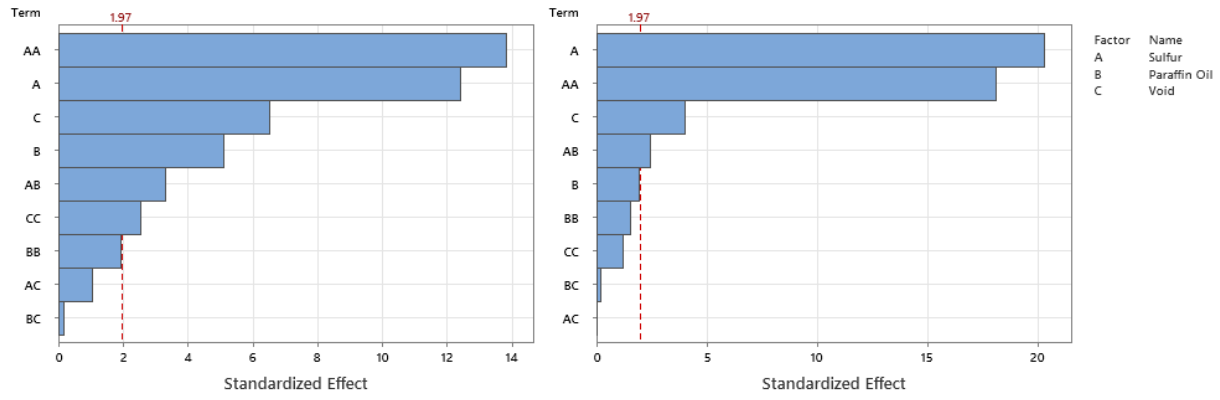

(a) (b)

Figure 33. The Pareto Chart of Standardized Effects for (a) n_{relax} and (b) tan δ.

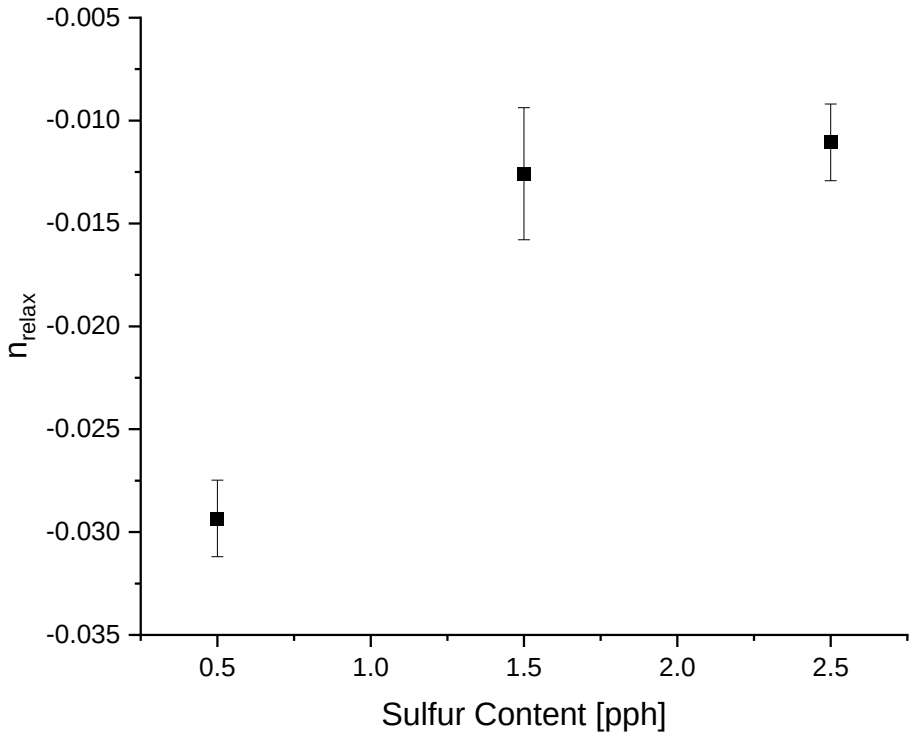

Figure 34. The curved response of sulfur content on n_{relax}, further confirming the results in the Pareto chart.

Artificial Neural Network Prediction Results

The final ANN architectures selected are summarized in Table 11, and the parity plots of the experimental and predicted values from 5-fold cross-validation are illustrated in Figure 35. For

each of the four material properties, the R^2 value increased compared to the linear regression baseline. It is worth noting that a simple NN architecture has the ability to capture material-property correlation pertinent to the rubber blend content, especially for n_{relax} and $\tan\delta$ whose underlying functions are more nonlinear, as suggested by the significant improvements of the two. When compared with RSM, ANNs also showed improvements in prediction accuracies for n_{relax} and $\tan\delta$. This again confirms that n_{relax} and $\tan\delta$ would benefit from a more nonlinear modeling approach. Although the selected ANN architecture for σ_{relax} performed slightly worse than RSM, some of the more complex architectures (with over 1000 parameters) tested could reach a comparable R^2 value. However, to avoid overtraining, the model complexity and accuracies were leveraged during the model selection process.

Table 11. The predictive capabilities of the ANN and the overall architecture for each model.

Target Material Property	No. of Hidden Layers	No. of Neurons in Hidden Layer	Learning Rate	Number of Learnable Parameters in the Model	5-Fold CV R^2 of ANN	5-Fold CV R^2 of Linear Regression Baseline
Durometer	1	64	0.01	321	0.99	0.91
σ_{relax}	2	16, 16	0.01	353	0.96	0.90
n_{relax}	2	16, 16	0.01	353	0.94	0.48
$\tan\delta$	1	32	0.003	161	0.98	0.67

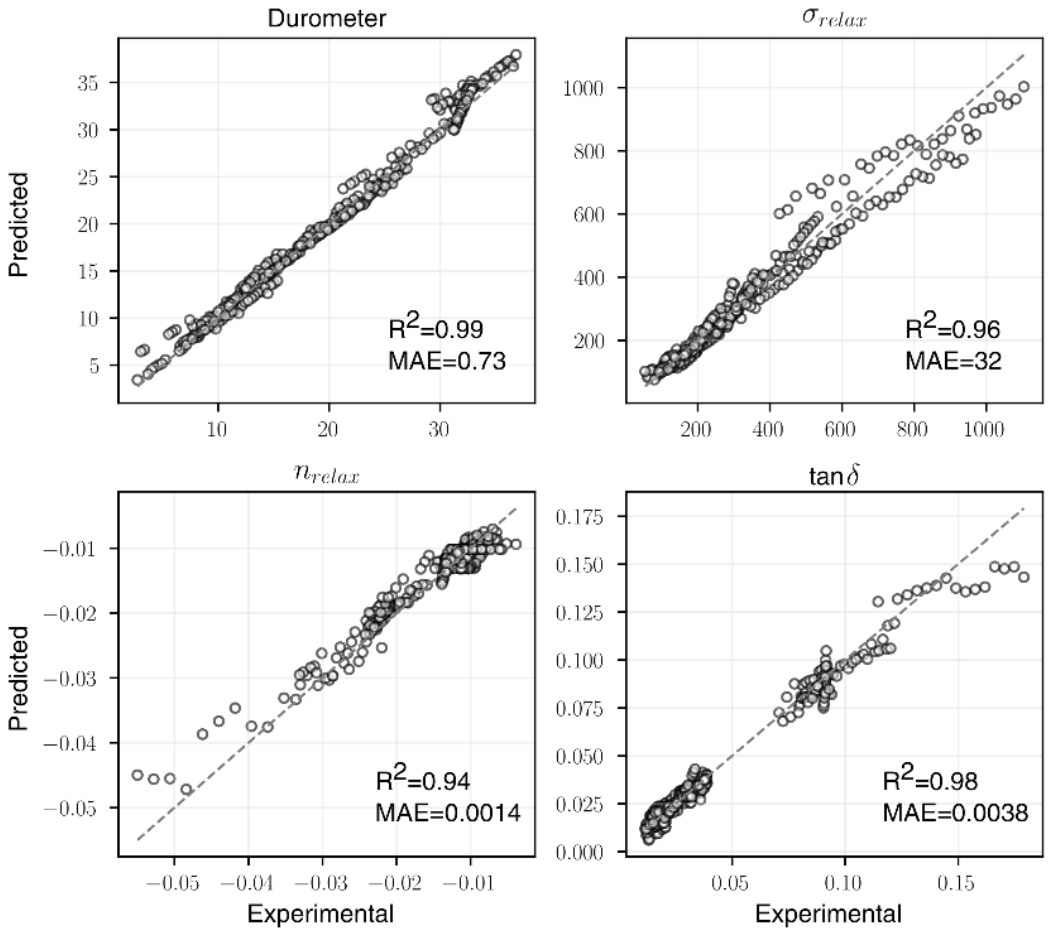

Figure 35. The parity plots for all four ANN models.

After the models were developed, the sensitivity analysis was performed on both the linear regression baseline and the ANNs. For linear regressions, the gradients were simply the weights, and for ANNs, the gradients were obtained from backpropagation. Figure 36 shows the averaged gradients from the individual folds of cross-validation. In general, the gradients from both the LR and ANN models have the same trend except for n_{relax}, where the paraffin oil content has a positive gradient in LR but negative gradient in ANN. The RSM analysis also suggests a negative gradient, which corroborates with relaxation theory as the plasticizer increases the free volume between the rubber molecules, further facilitating relaxation as you increase plasticizer content.

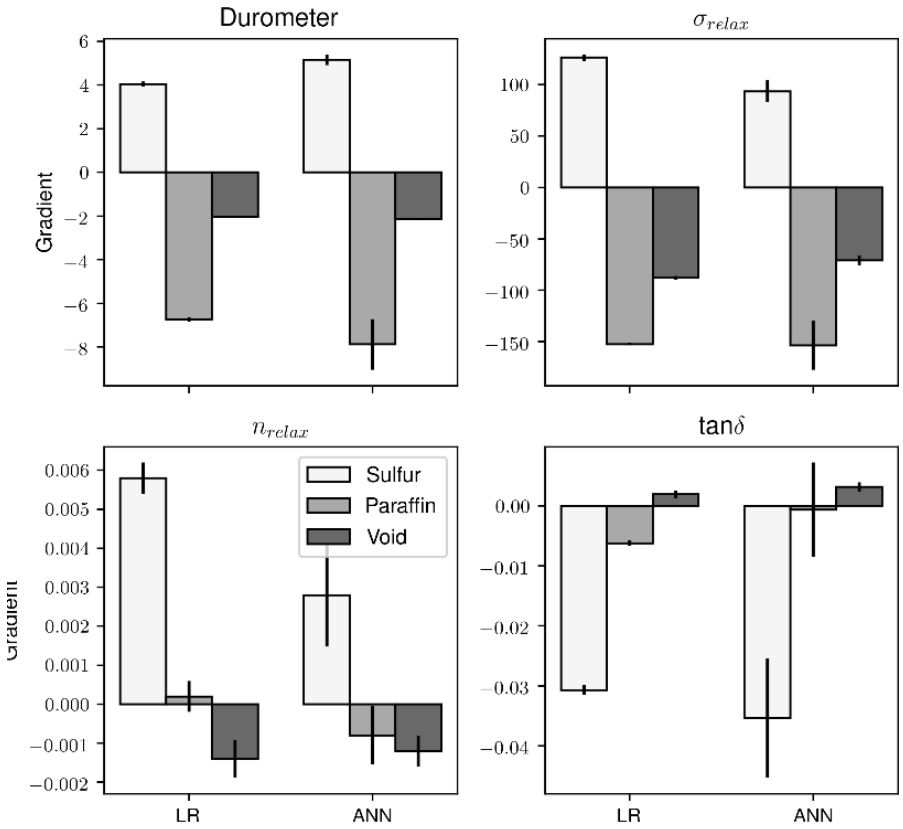

Figure 36. The results from the sensitivity analysis for both the linear regression baseline and the ANNs.

Gaussian Process Regression Prediction Results

The parity plots for GPR are illustrated in Figure 37, with the shaded region suggesting the bounds for 95% confidence intervals (obtained by 1.96 standard deviations given by GPR prediction). For each of the four material properties, the R^2 value increased significantly compared to all the above methods, and the uncertainties are small in regions where the experimental data are abundant. In spite of the ability to make predictions with uncertainty, it is difficult to obtain physical insights from GPR due to its nonparametric nature. However, given the high cross-validation accuracy, GPR could potentially be used to generate synthetic data for the Bayesian optimization algorithm that aims to find the optimal blend content.

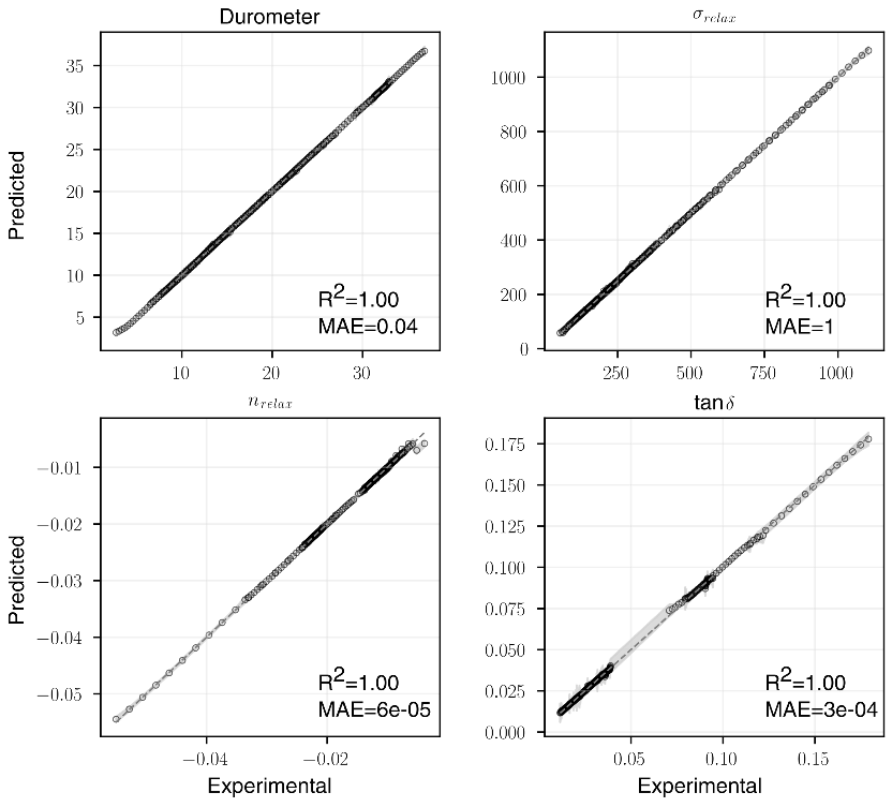

Figure 37. The parity plots describing Predicted vs. Experimental for GPR.

3.6 Material Design Optimization

With industries, such as the footwear industry moving towards sustainable material alternatives for midsoles, target properties could be selected based on an existing footwear material via characterization techniques. The respective methods would be implemented to predict the blends that would theoretically exhibit the target properties. In this section, we show that the previously developed predictive models can be used to aid reverse engineering.

RSM provides an empirical model that allows users to utilize it as a method for reverse engineering based on target parameters. Similarly, the trained ANN and GPR could also be used for reverse engineering. Based on the target parameters, a score function was constructed based on the weighted Euclidean distance between the predicted and the target values. The optimal set of parameters is the ones that minimize the score function. The input rubber blend compositions are constrained by experimental considerations, such as upper and lower bounds that are physically

meaningful and precision limits of the characterization equipment. Table 6 below shows the blends outputted by each predictive method which exhibit the target properties mentioned within it.

For ANN and GPR, since the input design space is relatively small, we generated all the possible input rubber blend compositions in the input design space within the feasible region. This is possible due to the consideration of experimental precision that makes the distribution of the design space rather discrete. Overall, around 6600 possible blend compositions and their corresponding predicted properties were obtained. The composition with the minimum score (loss) was identified as the optimal blend composition.

The above reverse engineering method is relatively straightforward and fast to populate given this small design space. In fact, all the predicted values were generated within seconds. Nevertheless, when we have a large design space or when the input compositions are no longer discrete, this method may fail. Alternatively, we used Bayesian optimization (BO) [104] to find the optimal blend compositions. BO utilizes Gaussian processes (as in GPR) to solve the black-box optimization problem—in this case, a minimization problem with an objective function to minimize the score while satisfying the design parameter constraints [105]. The algorithm first establishes a surrogate model that computes a posterior distribution (mean and variance) of the objective function using a set of sample points. The surrogate model is then used to construct an acquisition function that estimates the distribution of the objective function for any test data. A recommended blend composition can be obtained by minimizing the acquisition function (where we used the score function); this blend composition is used to obtain a new observation data point (usually from an experiment or from some existing predictive model) to be incorporated for updating the surrogate model. After running these steps iteratively, the algorithm will converge to an optimal blend composition.

In this study, instead of collecting data from experiments for each iteration, we used the previously trained GPR model to generate the new “observations” given its high CV accuracy. The BO was implemented using Scikit-learn [98] (version 0.24.2) and Scipy [106] (version 1.7.0). The resulting blend composition from BO is similar to the findings from the previous approach. Overall, even though BO bypasses the construction of specific predictive models for material properties, it can guide the design of new experiments and thus reduce the overall experimental costs.

Table 12. Summary of the blends that were classified as the optimal blend based on target properties.

Modeling Method	Prediction Results
Target Properties	σ_{relax}: 90 n_{relax}: −0.0527 tan δ: 0.066
RSM	Sulfur: 0.65 Paraffin: 69.5 Void: 30.0 Durometer: 0.45
RSM-predicted Properties	σ_{relax}: 90.26 n_{relax}: −0.02875 tanδ: 0.0982
ANN	Sulfur: 0.55 Paraffin: 54 Void: 17 Durometer: 5.612
ANN-predicted Properties	σ_{relax}: 82.45 n_{relax}: −0.0399 tanδ: 0.113
GPR	Sulfur: 0.55 Paraffin: 57 Void: 10 Durometer: 6.187
GPR-predicted Properties	σ_{relax}: 111.78 n_{relax}: −0.0347 tanδ: 0.114

Natural rubber formulation methodologies implemented within industry primarily implicate a high dependence on the formulator's experience as it involves an educated guess-and-check process. The formulator must leverage their experience to ensure that the number of iterations to the final blend composition is minimized. The study presented in this paper includes the implementation of blend formulation methodology that targets material properties relevant to the application in which the product will be used by incorporating predictive models, including linear regression, response surface method (RSM), artificial neural networks (ANNs), and Gaussian process regression (GPR). Training of such models requires data, which is equal to financial resources in industry. To ensure minimum experimental effort, the dataset is kept small, and the model complexity is kept simple, and as a proof of concept, the predictive models are used to reverse engineer a current material used in the footwear industry based on target viscoelastic properties (relaxation behavior, tan δ, and hardness), which all depend on the amount of crosslinker, plasticizer, and the quantity of voids used to create the lightweight high-performance material. RSM, ANN, and GPR result in prediction accuracy of 90%, 97%, and 100%, respectively. It is evident that the testing accuracy increases with algorithm complexity; therefore, these methodologies provide a wide range of tools capable of predicting compound formulation based on specified target properties, and with a wide range of complexity.

4. Viscous Heating Fused Filament Fabrication 3D Printer

4.1 Motivation for Optimizing Fused Filament Fabrication 3D Printing

Fused Filament Fabrication (FFF), also referred to as Fused Deposition Modeling (FDM™) is an additive manufacturing technology which deposits material layer-by-layer until creating a full three-dimensional structure. Figure 38 below graphically depicts the overall workings of such technology, whereas a plastic filament is pushed into a heated nozzle via a gear-driven pushing system. Once the solid filament comes into contact with the heated nozzle, melting begins to occur and the physical pressure exerted by the gears causes material to travel through the small die until being deposited onto the print bed.

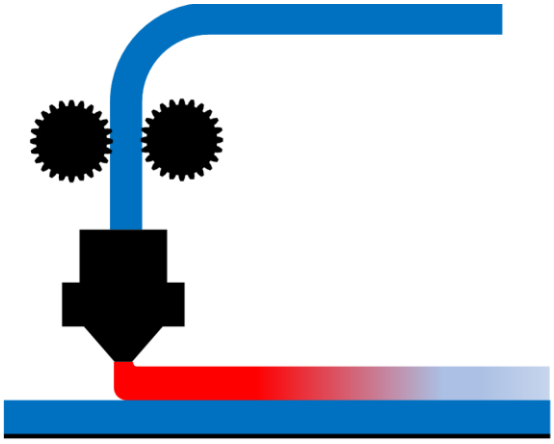

Figure 38: Graphical depiction of the 3D printing process via FFF

Such stratified build approach provides users with a method of manufacturing complex parts without the need for a complex and costly mold. Avoidance of acquiring molds is a crucial aspect within manufacturing as these mold costs are quite elevated [108-109]. If a user constantly creates mold design modifications, this increases overall expenses because of mold manufacturing and continuous machine setup. Additive Manufacturing (AM) has the benefit in that no molds are needed for production of parts. One essentially inputs the 3D model within a slicing engine, and the software provides the user with specific machine instructions. For this reason, industry has begun embracing additive manufacturing for various uses, such as for: producing tooling, end-of-use products and for prototyping [110-112].

While AM provides users with design flexibility and with reduced capital costs, it comes with its own set of limitations and disadvantages. Time for manufacturing is one of the largest limitations that it has for full implementation within high-volume manufacturing. Currently, print speeds average around 60 mm/s and result in extensive print times ranging from hours to multiple days depending on the size of the part. This machine limitation is brought about by the physical limitation of the gears responsible for pushing the filament into the heated nozzle. The force exerted onto the nozzle reaches a threshold in which the gears begin to slip against the filament, ultimately halting all movement towards the nozzle [113-114]. This has led for the development of high force gearing mechanisms which can impart large amounts of force, but this ultimately leads to mechanical failure of the filament under compression. Secondly, the layer-by-layer build approach produces extremely anisotropic parts, leaving vulnerabilities within your final product [115-117]. The anisotropic behavior is exacerbated when working with fiber-reinforced materials, as it can be clearly seen (Figure 39) that depositing such materials causes fiber orientation to primarily be in the print direction [118-119].

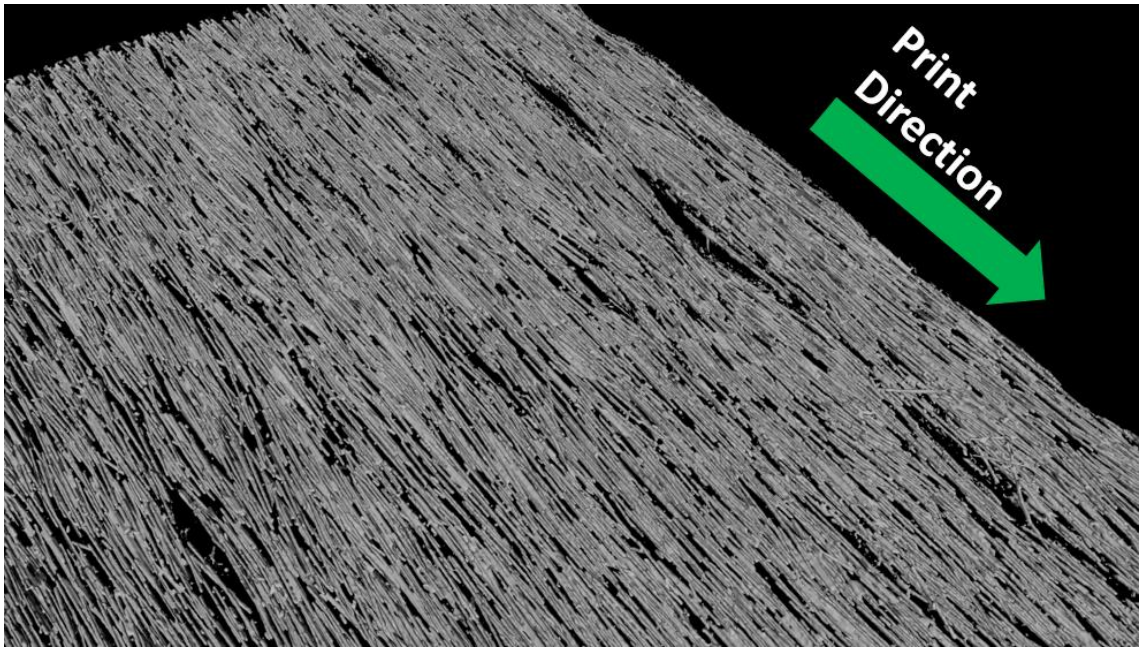

Figure 39. micro-CT scan of Nylon with short glass fiber reinforced 3D printed beads.

Creating a part with the majority of the fibers oriented in one direction produces a component with favorable strength-characteristics in the print direction, but ultimately reduces the strength perpendicular to the print direction. The highly anisotropic nature of 3D printed parts makes it difficult for prediction of part failure, therefore, this limitation has hindered its implementation within demanding engineering fields such as the aerospace and automotive industries. For these two reasons, the slow embrace of AM within industry has remained minimal and solving both crucial issues in FFF would alleviate the negative repercussions of AM.

4.2 Introduction to Viscous Heating

It was noted that the amount of force in which the gears can exert onto the filament is limited, which is directly related to the extrusion speed during the FFF 3D printing process. Increasing filament force directly increases extrusion speeds, therefore, a proposed solution to the slow printing speed issue lies in being able to print at the same given print speed but at lower forces. For this to happen, heat transfer must occur at a faster rate, ultimately allowing for melting to occur at a rapid pace. Now, the thermal conductivity of polymers hovers around $0.2\ \frac{\mathrm{W}}{\mathrm{mK}}$ while the thermal conductivity of steel is approximately $45\ \frac{\mathrm{W}}{\mathrm{mK}}$ [120-121]. Heat transfer driven by conductivity is quite limited for plastics given their extremely low thermal conductivity coefficients, therefore,

introducing viscous heating into the equation provides an accelerating effect to this heat transfer problem.

$$\rho C_p \frac{DT}{dt} = k\left(\frac{\partial^2 T}{\partial x^2} + \frac{\partial^2 T}{\partial x^2} + \frac{\partial^2 T}{\partial x^2}\right) + \dot{Q}_{\text{heat source}} + \mu\left(\frac{\partial u_x}{\partial u_y}\right)\left(\frac{\partial u_x}{\partial u_y}\right) \quad (16)$$

One can harness viscous heating by introducing movement around the stationary plastic surface which is in contact with the heated metallic surface. Frictional heat caused by the interaction between the stationary surface and the moving surface produces viscous dissipation, which results in an added heat transfer mechanism within the system. It has been proven that viscous heating has the ability of increasing energy efficiency during the extrusion process as taking advantage of heat generated via heat dissipation lessens the amount of energy required from an external heating source [122]. This concept of viscous dissipation within conventional polymer processing has the ability of being applied within advanced manufacturing technologies such as within the FFF 3D printing process. The concept of applicability can be proven by constructing an experimental setup where a plastic rod is pushed onto a heated surface, all while introducing rotation to either the heated surface or to the plastic rod itself. From there, it can be investigated if the pressure melt removal process is accelerated when rotation is introduced.

4.2.1 Proof of Concept

Introducing viscous heating has the ability to eliminate one of the largest bottlenecks in FFF 3D printing, which is long lead times for production. Experiments have shown that melting speed is directly related to the amount of force used to drive the filament onto the heated nozzle surface, and that the amount of force applied onto the filament is one of the primary physical limitations for conventional FFF 3D printers [107]. There comes a point in which a larger amount of force is no longer attainable by the hardware, which is where this new viscous heating technology takes into full effect. The physics of such rotation have been proven by creating small experimental setup (Figure 40 and 41) where plastic rods are rotated at varying rotational speeds and pushed onto a heated platform to understand the influence of rod diameter, temperatures, forces and RPM on melting behavior.

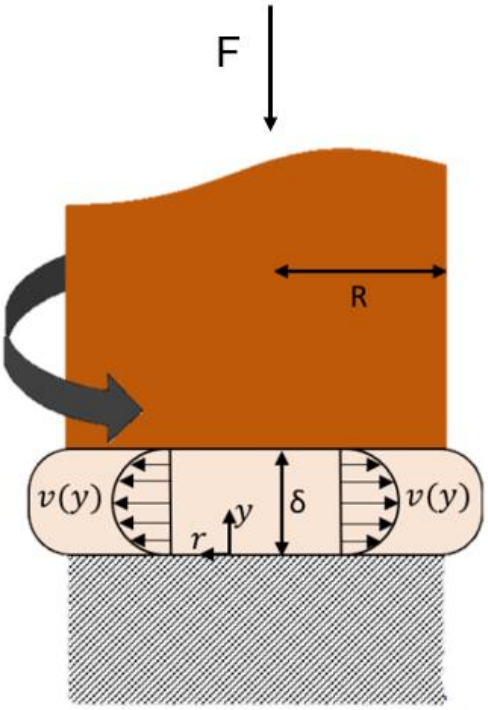

Figure 40. The melting experiment of applying rotation to the plastic rod while exerting a downward force onto a heated surface.

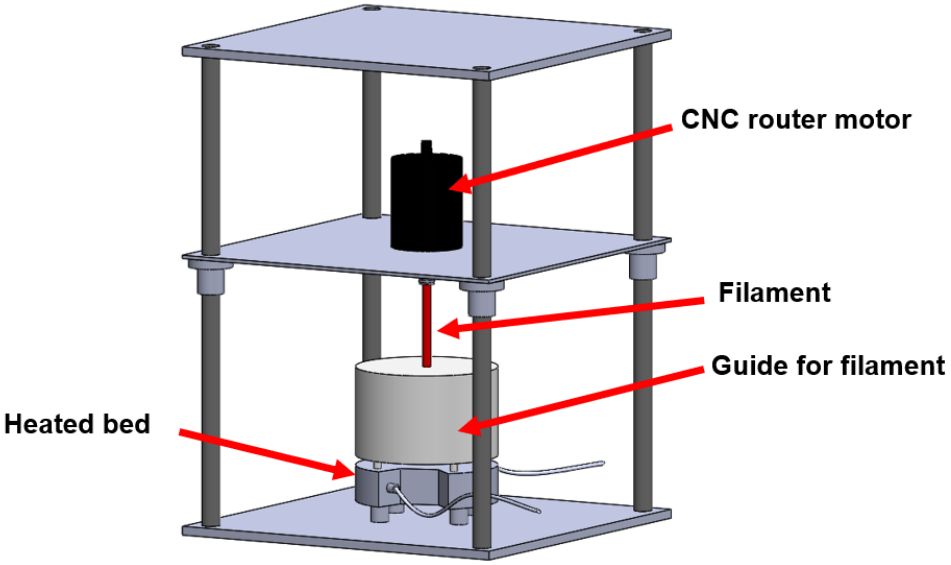

Figure 41. Small-scale experimental setup to prove the influence of viscous heating on melting behavior.

The primary components within this experimental setup include two 200W cartridge heaters placed inside the heated bed made up of Aluminum 6061. By having a K-Type thermocouple control the heated bed temperature, this allows for testing various isothermal conditions, ultimately mimicking the heated nozzle in the FFF 3D printing process. An adjustable collet was attached to the 24V Genmitsu CNC router motor to allow for plastic rods of varying diameters to be tested. Rotating the plastic rods at high RPMs would result in the rods being displaced in the radial direction because of the high centrifugal forces. For that reason, a low-friction PTFE guide was installed to ensure the plastic rods did not create frictional heat when coming into contact with the guide tube surface. The last component of the setup is the structure which holds the CNC router motor. The platform is held in place by four linear bearings which allow for the plastic rods held by the CNC router motor to move in the vertical direction towards the heated bed with minimal frictional losses.

For this experimental study of the influence of viscous heating on the melt removal process, each plastic rod was cut to 100 mm lengths and was weighed before/after testing to calculate the amount of material melted for 1 minute of testing. Testing included warming up the heated surface to the pre-specified temperature and waiting 10 minutes before testing to ensure isothermal conditions were met. By placing a weight at the center of the CNC router platform one can control the force being exerted onto the plastic rod. After placing the corresponding weight onto the platform, the plastic rod was fixed into the collet and lowered until reaching full contact with the heated bed. Upon completion of the 1-minute test, the platform was lifted and the weight of the plastic rod which remained intact within the collet was measured. By using a power supply to modify the amperage and voltage going into the CNC router motor, this allowed for testing various rotational speeds within our design of experiments. It should be noted that a laser photo tachometer was used to monitor and to ensure a consistent rotational speed was sustained during each experimental condition.

Design of Experiments for Melt Removal Process Setup

The design of experiments is described below (Table 13) whereas Nylon was chosen because of its significance within industry and PEEK was chosen because of its difficulty for implementation within industry because of its high-melting transition. Each experiment was repeated at least 5 times to ensure repeatability in results.

Table 13: Design of experiments for the small-scale experimental study referred to as the pressure melt removal experiment.

Experimental Condition	PEEK	Nylon 66
RPM [-]	0 – 12,500	0 – 10,000
Force [N]	15, 36	15, 36
Temperature [°C]	310, 330, 350	260, 275, 290
Diameter [mm]	4.7625, 6.35	3.175, 4.7625, 6.35

A laser photo tachometer was used to ensure constant RPMs were reached before testing and a K-type thermocouple was also employed to ensure isothermal conditions were met inside the heated bed for 10 minutes before commencing testing.

4.2.2 Influence of Viscous Heating to Melt Throughput

As stated above, the primary goal of introducing viscous heating within the 3D printing process is to drive printing forces down, ultimately facilitating the faster movement of the filament through the nozzle. For this experimental setup, the objective was to prove that the introduction of rotation caused an increase in melting performance, and upon completion of testing with Nylon 66 plastic rods, it can be appreciated in Figure 42 below that increasing RPMs of the plastic rod had an increasing effect on melt throughput. For the set of experiments shown in Figure 42 below, plastic rods of varying diameter were rotated at RPMs ranging between 0 and 8000 RPMs. The amount of material melted at a one-minute interval was logged and it can be seen from the figure below that rotation brings about an increase in melting behavior. It can also be observed that the larger diameter rods experience an increased rate of melting as the experiment moves towards higher RPMs. Given that viscous heating utilizes the interaction between surfaces, this increase in rate of melting can be attributed to the increase in surface area from the larger diameter rods. By purely pressing the plastic rod against the heated bed at 280°C without rotation, all plastic rods with varying diameters reach a melt throughput of about 160 mg/min. Now, if comparing the static rod results with rotation, it can be seen that at 7000RPMs that the 6.35 mm, 4.6725 mm and 3.175 mm diameter rods reach a melt throughput of 482 mg/min, 389 mg/min and 263 mg/min, respectively.

These changes in melt performance translate to a 3x, 2.4x and 1.6x increase in melt performance for plastic rods with the following diameters: 6.35 mm, 4.7625 mm and 3.175 mm, respectively. Given the large number of experiments, only some of the experimental conditions will be discussed within this section. To provide an overall analysis of the influence of viscous heating, the Response Surface Method was employed to offer predictive capabilities and statistical insight to the underlying physics of this phenomenon. This statistical analysis is to be explained in the ensuing section.

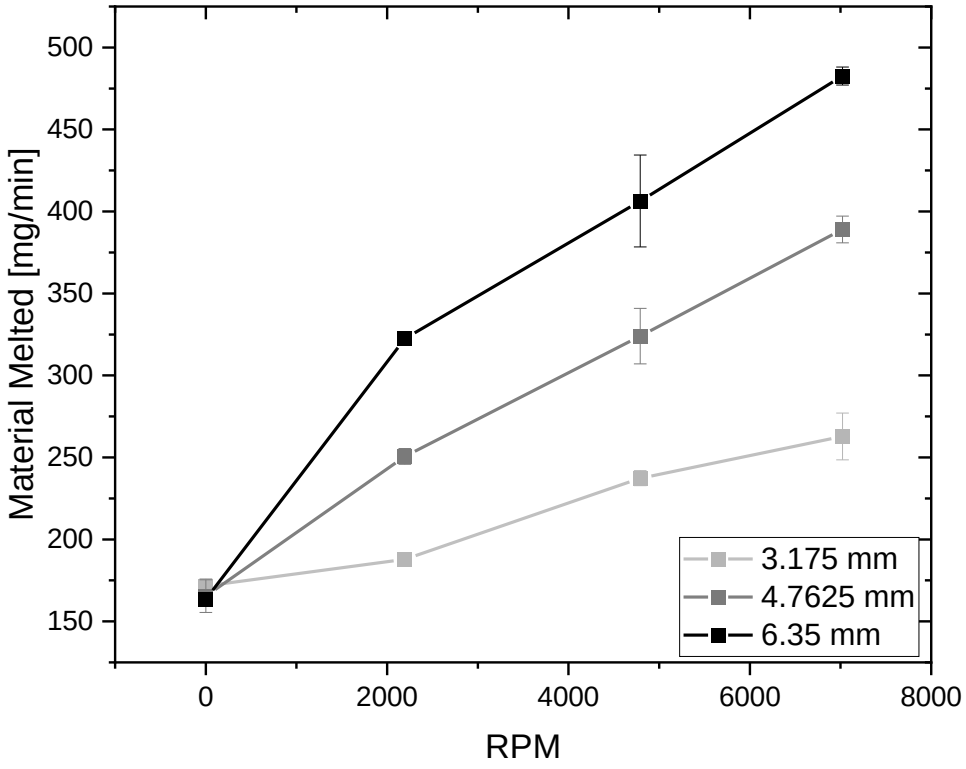

Figure 42. Pressure melt removal experiments of Nylon 66 at 280°C for varying rod diameters and rotational speeds.

Similar trend to what is seen in Figure 42 above is observed when increasing the heated bed temperature to 295°C. Figure 43 below depicts the increasing effect of RPMs on melt throughput for the Nylon 66 rods and it also shows how increasing diameter also increases melt throughput rate.

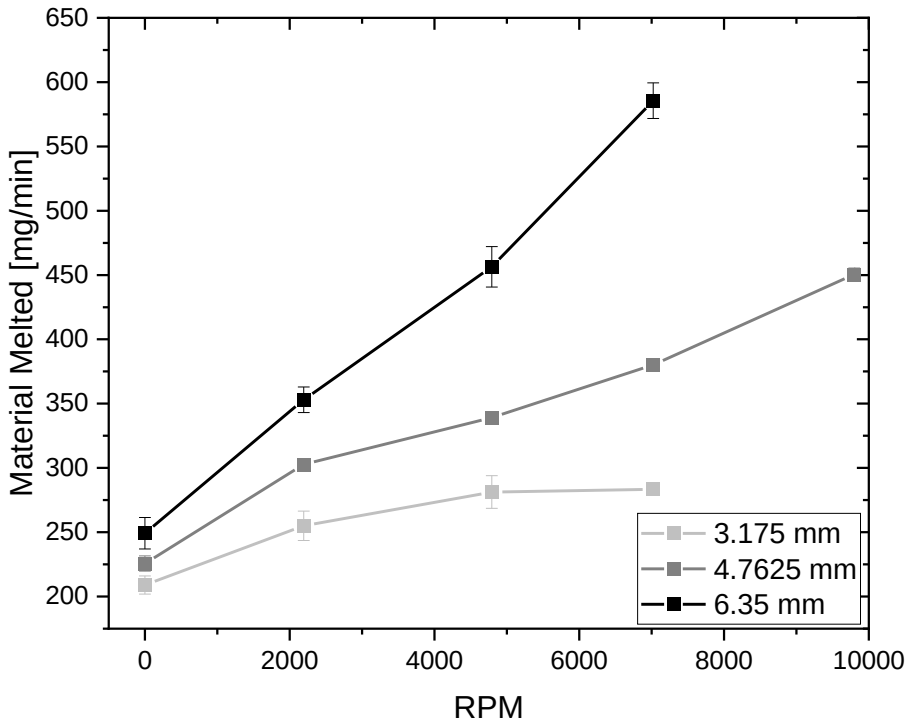

Figure 43. Pressure melt removal experiments of Nylon 66 at 295°C for varying rod diameters and rotational speeds.

As this technology is centered around minimizing forces, we can start to take a look into the effects of print forces and RPMs on melt throughput. Figure 44 below shows the comparison between tests with varying temperature, forces and RPMs for Nylon 66. Similar to what Colón and coworkers uncovered with the instrumented Fused Form FFF 3D printer, an increase in force results in an increase in melt throughput. This effect can be appreciated by the vertical shift present between the 15 N and 36 N test conditions, whereas the higher force results in a positive vertical shift within the plot.

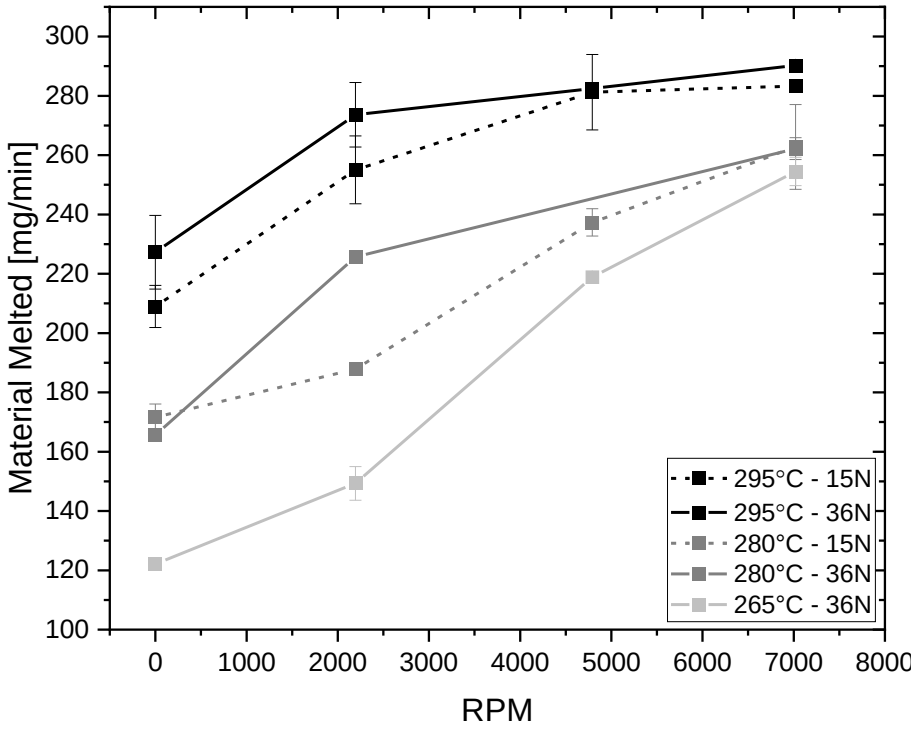

Figure 44: Pressure melt removal experiments for the Nylon 66 3.175 mm diameter case at varying temperatures and at two distinct forces.

As mentioned before, the experimental plan included testing PEEK as this material is known for its high-temperature transitions, making it difficult to incorporate within conventional manufacturing practices. Figure 45 below shows how PEEK can experience high throughput melting if rotation is introduced into the apparatus. It is evident that more material throughput will result from a system that is heated to a higher temperature or if the material is pushed onto the heated surface with a greater force, as seen in previous work [107]. The novelty of this system is that now there is a third variable, viscous heat, that can be introduced to further accelerate melting. Figure 45 below clearly shows how 750 mg of material is melted per minute when one exerts 36 N of force and heats the material to 350°C. One is now able to achieve the same melting behavior if the force is kept at the same level, the temperature is decreased to 310°C and if the material is rotating at 3800 RPMs. Users are now also able to depend less on the heat generated from inefficient external heating systems and now utilize viscous heating, which localizes the heat generated by rotation onto the filament itself.

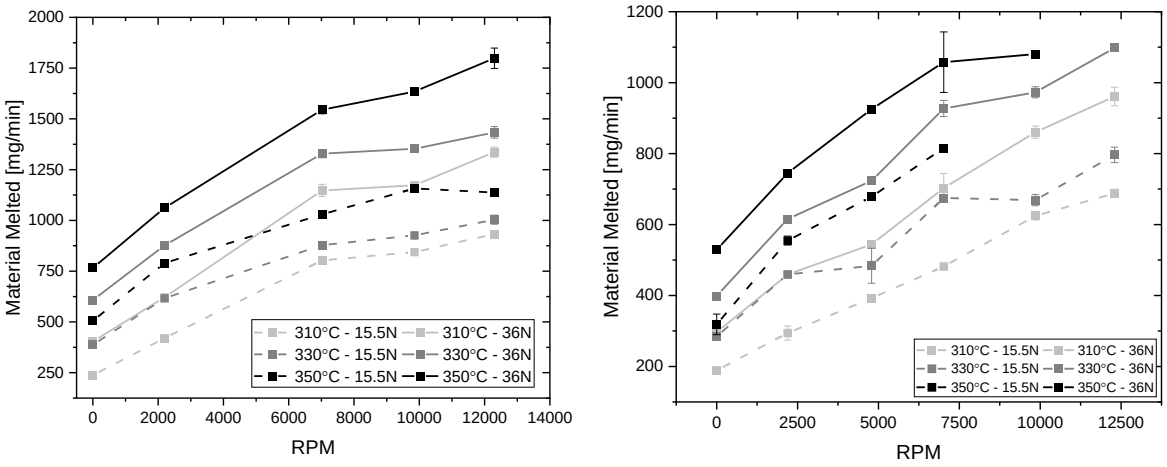

Figure 45. (a) Pressure melt removal experimental results using PEEK with a 6.35 mm rod and (b) 4.7625 mm diameter rod

Similarly, to what is seen the case with the 6.35 mm diameter rod, a 4.7625 mm diameter rod experiences similar effects in that an increase in pushing force results in the positive vertical shift in the y-axis, translating to a higher melt throughput. Furthermore, an increase in RPMs and temperature results in the increase in melt throughput, ultimately proving that viscous heating has a positive influence on melting rate.

4.2.3 Statistical Analysis of Viscous Heating

By feeding the experimental data into a Response Surface Method (RSM) model, one can run a statistical analysis to understand which parameters are the most influential in driving change to the output. The resultant algorithms for the Nylon 66 and PEEK experimental conditions result in a 91% and 97% prediction accuracy, respectively. It is evident that the Pareto chart below (Figure 46) states that diameter and rotational speed are the most influential parameters for altering melting speed within the system and that rotational speed has a non-linear influence on melting behavior. This information is crucial for design adjustments within the prototype to ensure the appropriate hardware is selected which would allow for more sensitive process parameter adjustments to what is deemed most influential by the statistical analysis of the small-scale setup.

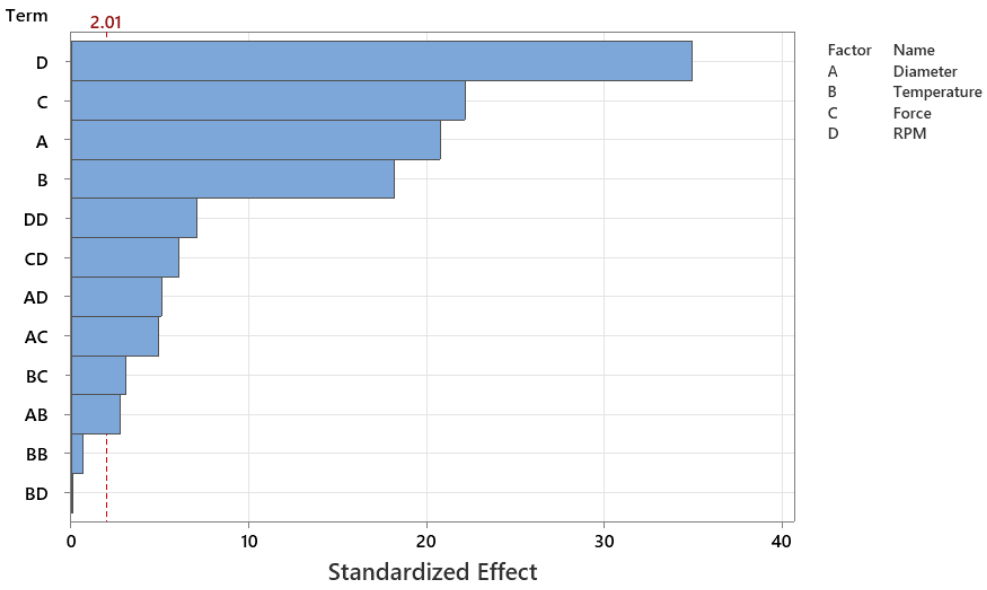

Figure 46. Pareto chart analysis of the input parameters for the PEEK melt throughput experiments

Each material possesses its own set of material properties, therefore, running a statistical analysis on separate systems is necessary to ensure the model does not confuse data with noise. In order to fully determine the effects of material properties on its behavior within the viscous heating 3D printer, thorough characterization work would be required for all tested materials given that same materials of different grades may perform drastically different regarding thermal, rheological and frictional properties [123]. After a fully characterization study, an RSM analysis would inform the user of which material properties provide a more profound effect on the output response.

Nevertheless, the Pareto chart seen in Figure 46 above lists the following 3 variables in order of importance: (1) RPM, (2) Force and (3) Diameter while Figure 47 below depicts the Pareto chart for the Nylon 66 material which outputs the variables in a different order of importance. The Pareto chart for the Nylon 66 experiments state that the following three variables are in order of importance (1) RPM, (2) Diameter and (3) Temperature.

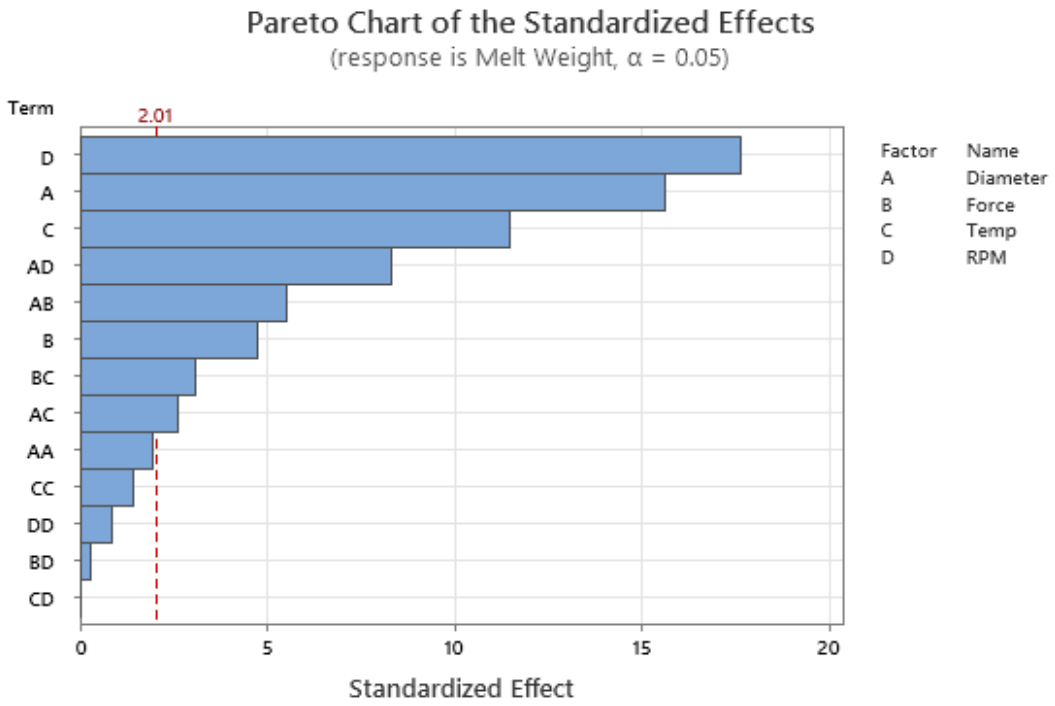

Figure 47. Pareto chart analysis of the input parameters for the PA66 melt throughput experiments.

Both models agree that RPM causes a non-linear effect on the output and that it is the most influential variable within the design of experiments, corroborating with our hypothesis that viscous heating arising from a rotating component has a profound effect on the system.

This analysis allows us to study the input variables at a quantitative level to ensure that the 3D printer construction incorporates hardware which functions effectively. For example, the RSM model states that RPMs is the most influential for both materials, therefore, this insight shows that a robust motor must be installed within the apparatus which is capable of transferring load efficiently. The following section will describe the general machine construction.

4.3 Rotating Nozzle Fused Filament Fabrication 3D Printer

4.3.1 General Construction of 3D Printer

The custom FFF 3D printer with capabilities of a rotating nozzle was built by Fused Form (Bogotá, Colombia) completely instrumented to record the force imparted by the pushed filament, temperature inside the nozzle, the change in extruded length over time and a tachometer to measure the rotational speed of the nozzle. The schematic of the instrumented extruder can be seen in Figure

48 below. It is important to note that the final design used for the rotating nozzle 3D printer is merely a rendition of what is found within the schematic in Figure 49. By using MATLAB as the acquisition interface in conjunction with the Arduino board, the 150 N $\pm$ 0.1N load cell acquired data at a sampling frequency of 5 Hz while the encoder had a sampling frequency of 6000 pulses per revolution.

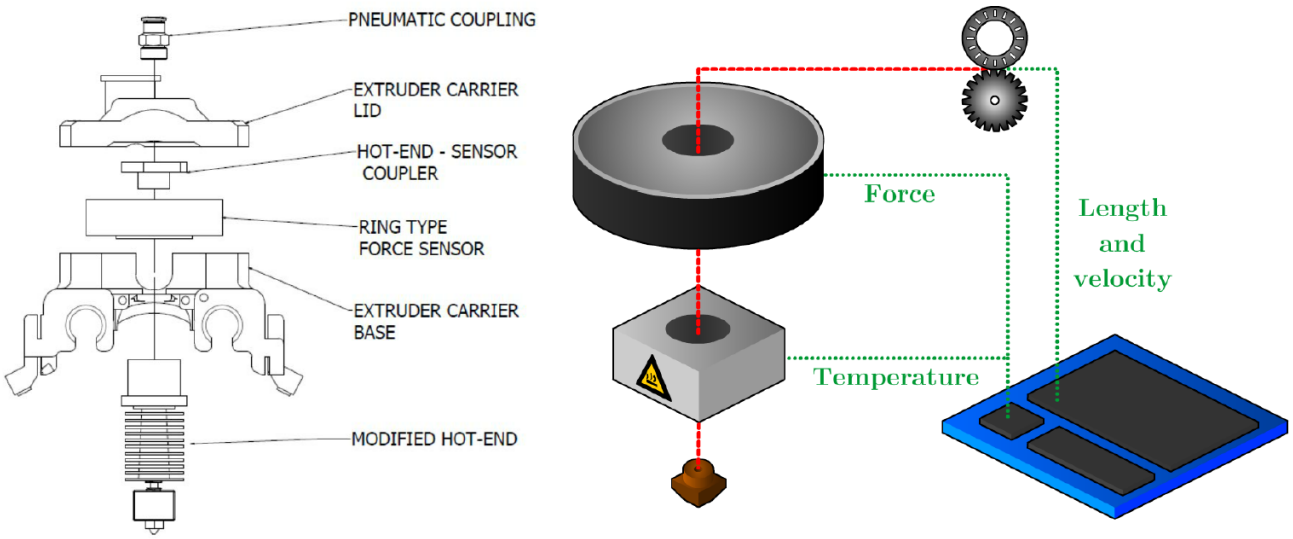

Figure 48. Schematic of the general construction of the modified extruder end used to provide extrusion length, force and temperature data during the 3D printing process [124].

The work within this study is not centered around hardware design and in the intricacies within the dynamic seal designed for minimizing material leakage during strenuous rotation. For that reason, only information at a high-level will be provided regarding the general construction of the 3D printer. To allow for rotation, the instrumentation within the nozzle needed to be connected to a slip ring which would ultimately allow rotation without cables becoming entangled.

An aluminum 6061 heat break was designed as a separation mechanism between the nozzle hot-end and the slip ring to ensure that heat did not travel towards the slip ring, eventually compromising the structural integrity and performance of the slip ring. To facilitate rotation, a 1100-peak-watt motor was used as the driving mechanism. It was designed as a side-mounted motor system, designed to indirectly transfer the power by use of a rubber cog belt. There exist no compact hollow-bore motor designs which would make this project economically feasible, therefore, an indirect driving system was chosen as it provides high torque and high-speed motors, all within a compact design.

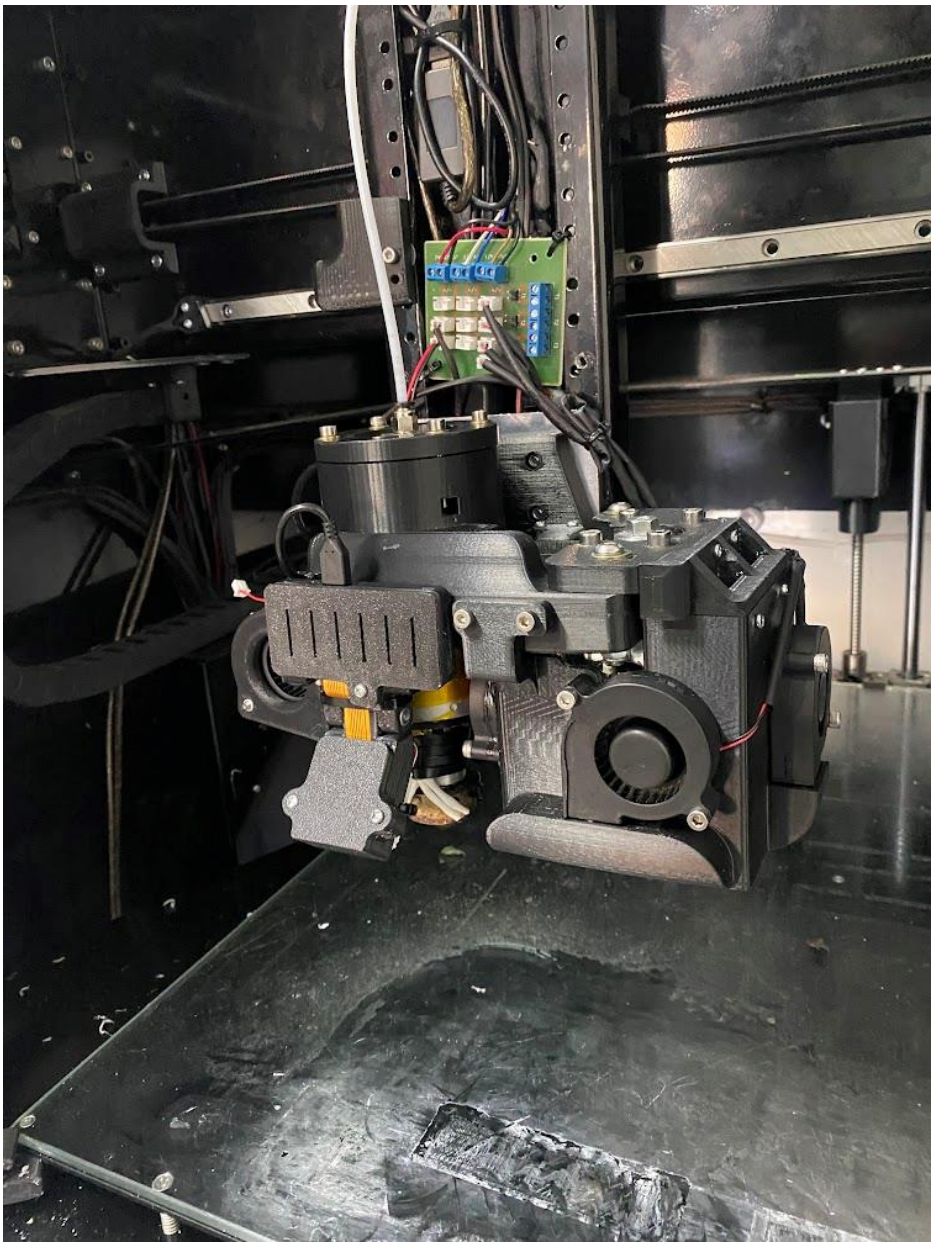

Figure 49. Photo of the existing setup

Figure 50 below shows a cross-sectional view of the extruder-end where the blue squared region (Figure50.a) depicts the stationary portion of the extruder and the green squared region is the rotating portion. Another crucial aspect of the design is in the guide tube seen within Figure 50.b below (red part) which is responsible for ensuring that the plastic filament does not come into contact with any rotating surface. The guide tube ensures that the interaction between the stationary filament surface and rotating nozzle surface only occurs in the yellow highlighted lines seen in Figure 50.b. Early contact with the rotating surface would result in premature melting, increasing

the risk of material leaking through any imperfections created within the machining of the components.

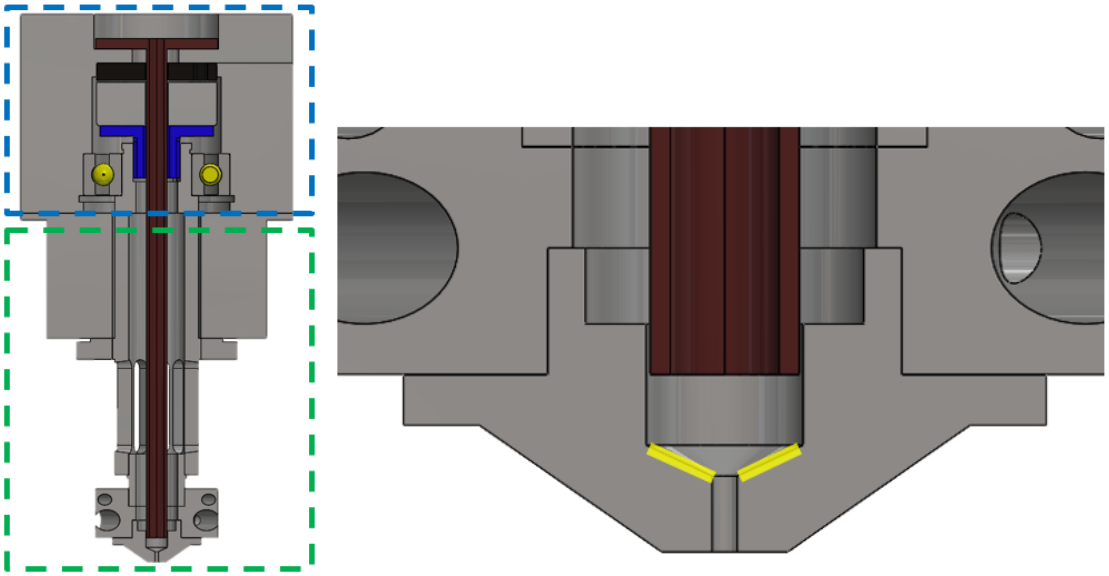

(a) (b)

Figure 50. (a) Overall cross-section of the design showing the static (blue) and rotating region (green). (b) Zoomed-in view of the region which shows the surface in which filament comes into contact with the rotating surface.

4.3.2 Influence of Rotating Nozzle on Print Forces

As the limiting factor for reaching high pushing forces is attributed to the filament pushing mechanism, the load cell within the instrumented 3D printer was crucial within the machine design to understand how a rotating nozzle influenced the force exerted onto the filament during extrusion. As seen in section 4.2.3, the rotation introduced viscous heating, ultimately accelerating the melting of the plastic rod. For these set of experiments, the viscous heating 3D printer was left to extrude in open-air, mimicking an extrusion process. By first conducting extrusion trials, this allowed for reducing variability caused by printing at various layer heights and the variability of depositing a bead onto a previously placed bead. To truly test the limits of the new 3D printer, tests were conducted on a short fiber-reinforced (~8%wt) Nylon filament (Matterhackers, USA). Tests were conducted by following the design of experiments seen below in table 14.

Table 14: Design of experiments for the extrusion trials using the viscous heating 3D printer.

Experimental Condition	**PA-GF**
RPM [-]	0 – 5000
Filament Speed [mm/min]	4, 6, 8
Temperature [°C]	200, 220, 240, 260
Diameter [mm]	1.75

These tests allowed for the understanding of how each input variable influenced the force experienced by the filament for a material which exhibits high mechanical properties because of its glass-fiber reinforcement. Figure 51 below shows a segment of the data acquired during the extrusion trials. To highlight a few of the observations, it can be observed how increasing filament speed has an increasing effect on forces, and that increasing RPMs has a decreasing effect on forces experienced by the filament. The decreasing effect that higher temperatures impose on print forces can be seen in Figure 52, whereas with aid of the color-scale, one can appreciate that increasing temperatures leads to a decrease in forces present within the nozzle. Instead of providing figures for the 15,471 datapoints collected from the instrumented 3D printer, these data points were used as training data for the RSM modeling technique to aid in the understanding of what is the most crucial component withing this design of experiments.

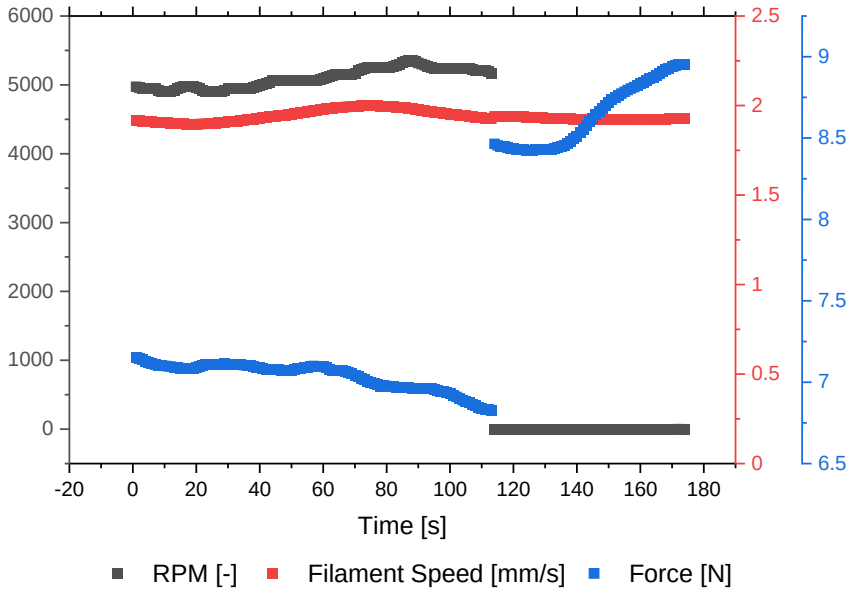

Figure 51. Raw experimental data points extracted from the instrumented 3D printer for tests at 260°C

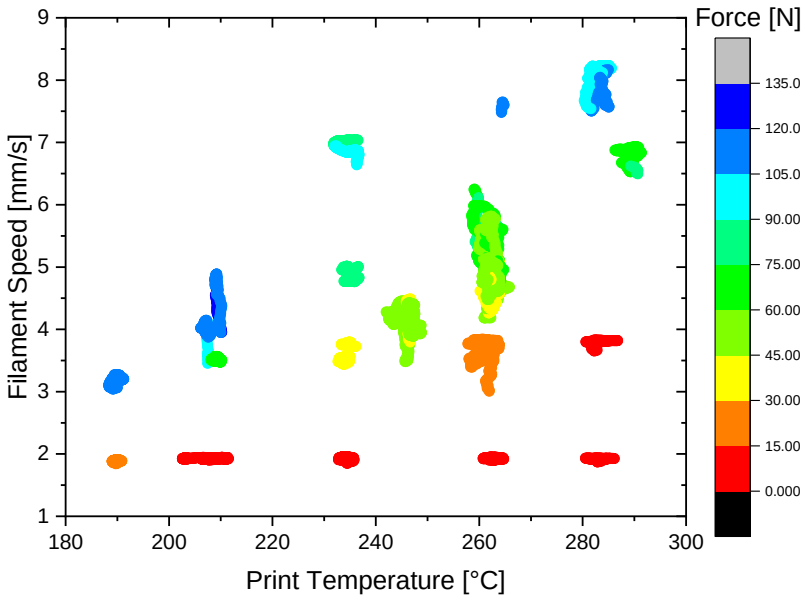

Figure 52. All datapoints extracted from 0 RPM trials using the instrumented 3D printer to show the effect of temperature and filament speed on forces.

As used previously, an RSM analysis was conducted to predict experiments within the range of the design of experiments which were not conducted, allowing us to understand this multivariable problem. The RSM model summary can be seen in table 15 below, whereas it can be se seen that all R^2 coefficients average out to a prediction accuracy of 87.66% and with an uncertainty of 0.01%. By having all three R^2 coefficients near one another, this indicates that the model is not vulnerable to overfitting. The model equation describes the regression model, which has RPMs represented as variable A, temperature is represented by the variable B and the filament speed is described by the variable C. Additionally, inspecting the variables' coefficients allows us to recognize the importance of each parameter within the model. This technique also allows for the interaction effects of variables to be studied by assessing the last three parameters within the model equation. Additionally, the RSM model also allows for us to understand which variables exhibit non-linear effects on the output response.

Table 15. Model summary of the RSM model which predicts extrusion forces within the instrumented viscous heating 3D printer

Model Equation	$\mathbf{R^2}$	$\mathbf{R^2_{adjusted}}$	$\mathbf{R^2_{prediction}}$
$\mathbf{514.54 - 0.04A - 4.61B + 67.37C + 0.000001A^2 + 0.0096B^2 + 0.31C^2 + 0.00016AB - 0.0043AC - 0.197BC}$	87.67%	87.67%	87.65%

By using the equation of the output response, one can generate contour plots (Figure 53) showing the non-linear effect of RPMs on extrusion forces and translating this model to various temperature profiles to understand the effects of temperature on forces.

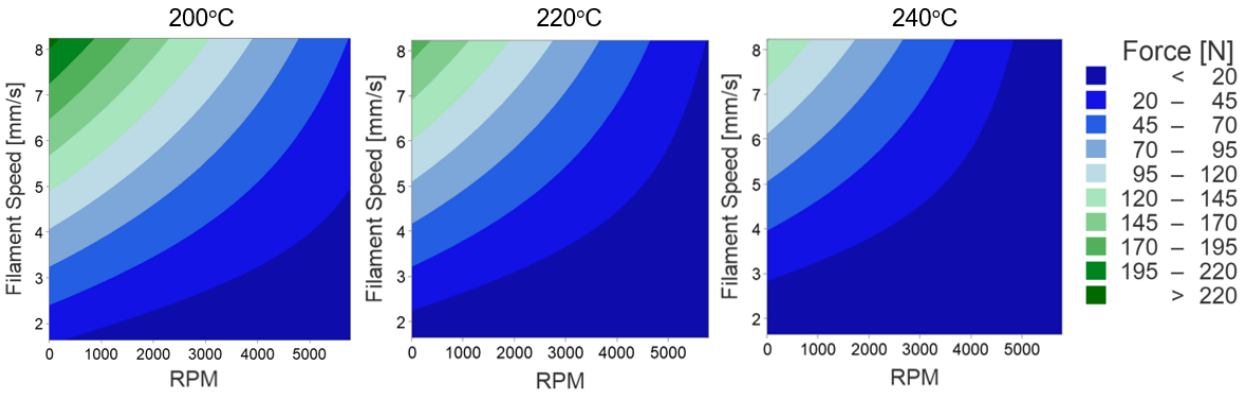

Figure 53: Contour plots displaying the effects of all input variables on the output response

It can be clearly seen from Figure 53 above that RPMs decrease forces non-linearly and that increasing temperature provides a horizontal shift to the contour plots. It can be observed that one is capable of extruding with a filament speed of 8 mm/s at near-zero forces when having the nozzle rotate at 5000 RPMs at 240°C. In addition to the two-dimensional contour plots which describe the multivariable problem, three-dimensional surface plots can be generated for each respective temperature, as seen in Figure 54 below. This allows us to appreciate that there are no overlapping points within the RSM model, leading to the conclusion that a change in temperature translates to an approximate vertical shift in the surface plot. One observation to note is that at very low filament speeds there is an apparent increase in extrusion forces as the 4000 RPM threshold is surpassed. Since forces are already near zero at 4000 RPMs, the additional rotation most likely begins to introduce noise as the system is no longer able to reduce forces below 0 Newtons.

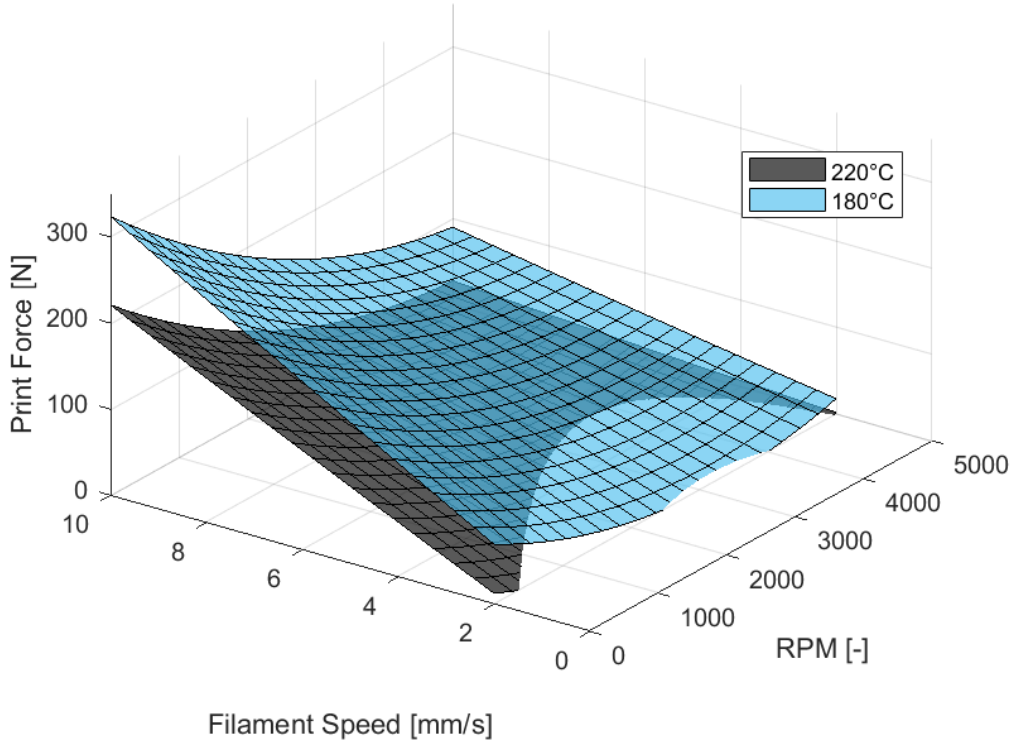

Figure 54. Surface plots from the RSM model extracted from the viscous heating 3D printer extrusion trials.

Like section 4.2.3, the Pareto chart (Figure 55) provides insight regarding the importance of each input variable. For the extrusion trial study, the input variables in order of significance are the following: (1) RPM, (2) Filament Speed, and (3) Temperature. The rotational speed of the nozzle is the most influential component within this instrument setup. This statistical information provided by the Pareto chart informs the designer of what hardware components should be prioritized in regard to robustness. Nevertheless, given the dynamic nature of the viscous heating 3D printer, a quite powerful controller and motor is required if rotational speed of the nozzle is to be chosen as the adjustable parameter for improving print quality. For sake of manufacturability of the 3D printer, and feasibility of the slip-ring design, the filament speed is chosen as the adjustable parameter given the ease of implementation compared to RPM.

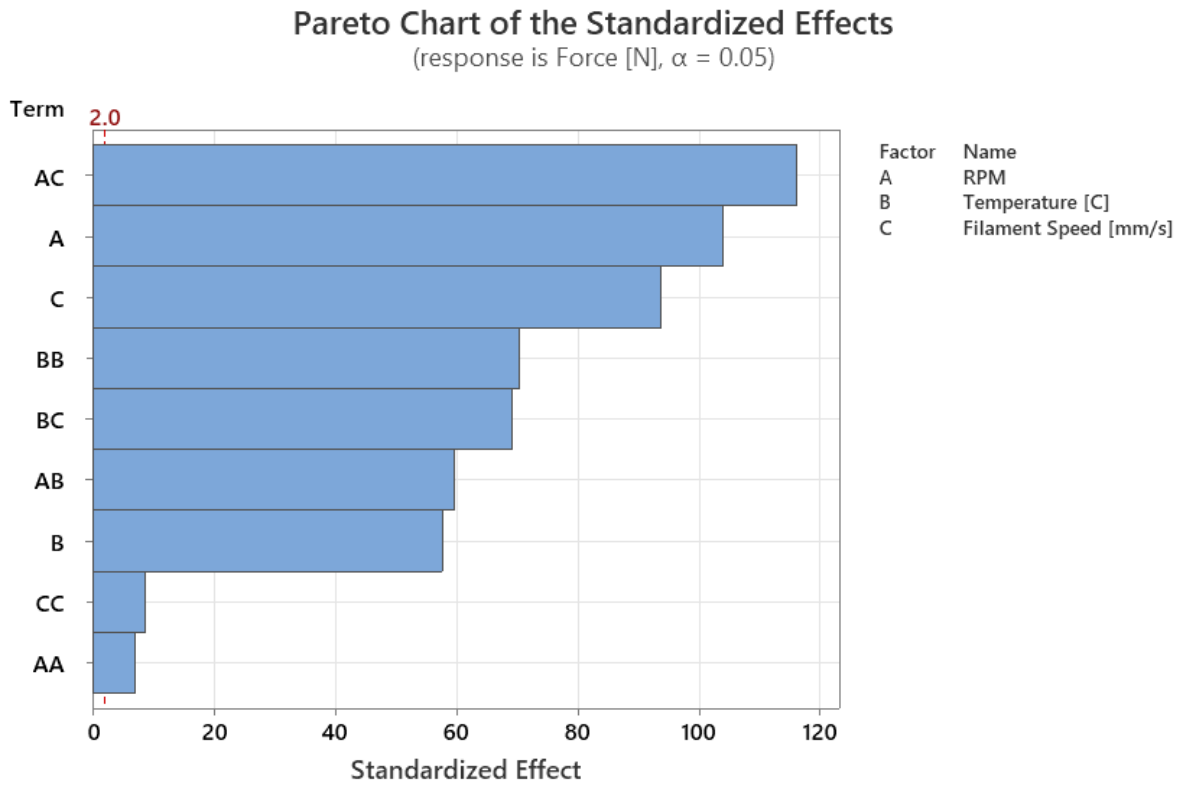

Figure 55. Pareto chart for the Nylon 66 glass-fiber reinforced extrusion trials using the instrumented viscous heating 3D printer

4.3.3 Influence of Rotating Nozzle on Microstructure

As mentioned above, the extremely anisotropic nature of FFF 3D printed parts creates the negative stigma of additive manufacturing implementation within high-performance manufacturing applications. For that reason, it is important to study the influence of the rotating nozzle on 3D parts, specifically gaining an insight regarding its microstructure. For full adoption of such technologies within manufacturing, it must be proven that the overall performance of the 3D printed parts produced with the viscous heating 3D printer results in superior properties compared to conventional FFF 3D printers where the nozzle remains in a still position. This section describes the characterization work related to microstructure analysis via micro-CT analysis. To begin scanning with the µCT, a rectangular sample was cut out (10mm x 10mm x 0.6mm) of the tensile testing coupon and four adjacent beads were analyzed within the region of interest to provide a representative analysis of the overall sample microstructure in regard to porosity, fiber orientation and fiber length for the 3D printed fiber-reinforced tensile testing coupons. It is important to note

that all tensile testing coupons were adapted from the ASTM D673 standard, whereas three layers were printed for each testing coupon. To allow for a consistent μCT scanning procedure, all samples were CT scanned using the parameters seen in Table 16 below. All microstructural analysis was completed using Volume Graphics' Fiber Composite Material Analysis module by using the raw μCT images extracted from the ZEISS Metrotom 800 μCT (Carl Zeiss AG, Oberkochen, Germany).

Table 16. μCT scanning parameters.

Variable	**Symbol**
Voltage [kV]	80
Current [μA]	80
Integration Time [ms]	1000
Gain [-]	8
Number of Projections [-]	1000
Resolution [μm]	4.85

First-layer adhesion provided a challenge for nylon short-fiber reinforced prints given the poor glass fiber adhesion properties onto a glass substrate. Therefore, to minimize issues with adhesion, the first layer was printed with no rotation and the following two layers were printed with rotation enabled to study the influence of the rotating nozzle on microstructure.

Rotating Nozzle Effects on Porosity

Adhesion of the first layer onto the printing substrate demonstrated a challenge due to the poor adhesion properties between two glass materials: one being the glass fibers present within the nylon glass-fiber reinforced filament and the other being the glass print bed. For that reason, the first layer of the 3-layer tensile testing coupon was printed without enabling rotation of the nozzle. Once the first layer was properly adhered, rotation commenced, and the two final layers were printed with rotation enabled.

The primary objective of this section is to show that a rotating nozzle does not impart additional porosity into the 3D printed part. By viewing Figure 56 below, two distinct curves are presented

simultaneously: the first dashed curve shows a test with rotation disabled and the solid curve represents a print with rotation enabled. Looking into the rotation-enabled print, it is important to note that 1 layer was printed without rotation. This translates to one third of the normalized thickness having been printed with no rotation. This one third is represented as the gray-shaded region within Figure 56 below and it can be clearly seen how the rotation-enabled print does not experience an increasing or decreasing effect on void content.

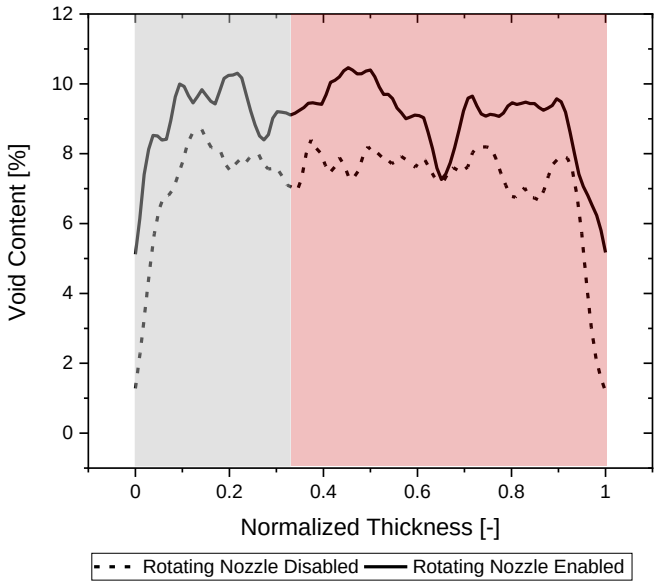

Figure 56. Void analysis of two 3D printed components. Dashed line represents the component 3D printed with a conventional FFF 3D printer setup and the solid line represents the 3D printed part with a rotating nozzle.

The independence of porosity on rotation can be seen in all other experiments within the design of experiments, whereas Figure 57 below depicts all of the void analyses data points overlaid behind the rotation-disabled distribution. This porosity study found no direct correlation between the rotational speed of the nozzle, temperature and print speed within the design of experiments.

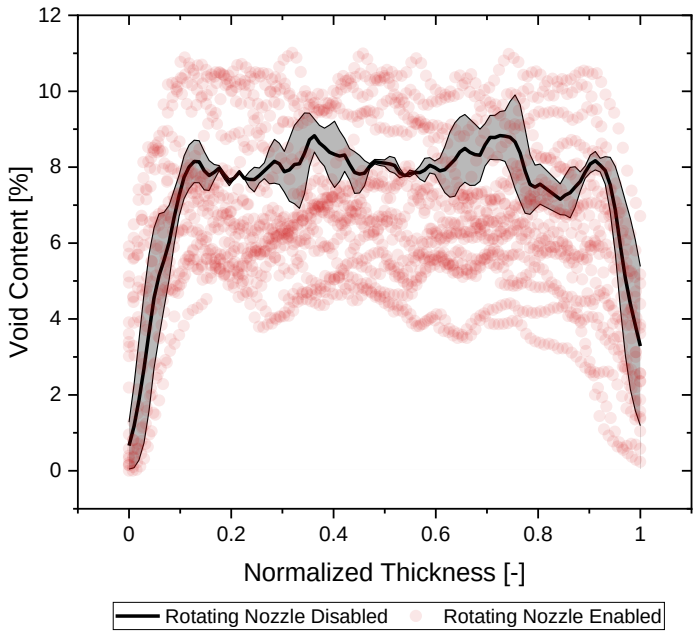

Figure 57. Void analysis on all samples to describe the independence of rotational speed of the nozzle on the void content within 3D printed samples.

Rotating Nozzle Effects on Fiber Orientation

As mentioned above, fiber orientation analysis is crucial for approximating mechanical performance as the orientation of fibers provides reinforcement in the fiber direction. In this work, the tensor representation proposed by Advani and Tucker [119,125] is used to quantify the fiber orientation distribution within the 3D printed components. If using a single glass fiber as an example and depicting it as a single rigid rod in a three-dimensional space, Figure 58 below describes how the angle pair (θ, ϕ), or unit vector $\boldsymbol{p}(\theta, \phi)$ is used to describe the fiber's orientation.

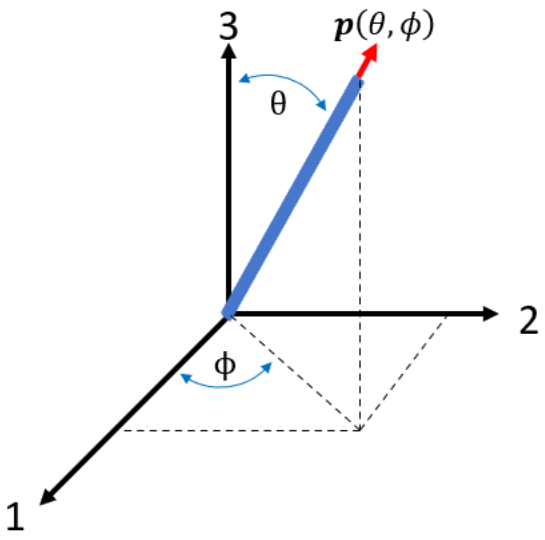

$$\mathbf{p} = \begin{Bmatrix} p_1 \\ p_2 \\ p_3 \end{Bmatrix} = \begin{Bmatrix} \cos\phi\sin\theta \\ \sin\phi\sin\theta \\ \cos\theta \end{Bmatrix}$$

Figure 58. Visual representation of how the angle pair is used to describe the orientation of a single fiber per Advani and Tucker's orientation method.

For describing the entire fiber population within a designated volume, Advani and Tucker proposed a concise orientation characterization method which represents the fiber orientation distribution via the use of a tensorial description. The outcome of this operation results in the orientation tensor a_{ij}, which is calculated by averaging all of the fibers' orientation throughout the volume of interest using the equations seen below.

$$\begin{array}{ccc} a_{11} = \langle \cos^2\phi \sin^2\theta \rangle & a_{12} = \langle \cos\phi \sin\phi \sin^2\theta \rangle & a_{13} = \langle \cos\phi \sin\theta \cos\theta \rangle \\ a_{21} = a_{12} & a_{22} = \langle \sin^2\phi \sin^2\theta \rangle & a_{23} = \langle \sin\phi \sin\theta \cos\theta \rangle \\ a_{31} = a_{13} & a_{32} = a_{23} & a_{33} = \langle \cos^2\theta \rangle \end{array}$$

* The angle brackets ⟨ ⟩ represents the average value of all fibers within the analysis

The diagonal components ($a_{11}, a_{22}, \text{and } a_{33}$) within the a_{ij} orientation tensor describe the orientation of the fibers at the specific location, whereas the 1-direction represents the printing direction, the 2-direction is the cross-bead direction, and the 3-direction denotes the thickness direction. It should be noted that the sum of the diagonal components equates to the value of 1, and that the ratio between the three tensors ($a_{11}, a_{22}, \text{and } a_{33}$) provides insight into how isotropic the fibers are within the volume. Figure 59 below shows two examples of how the orientation

tensors are used to describe the orientation distribution within a sample. It can be seen how scenario 1 (Figure 59, Left) represents a volume with randomly aligned fibers while scenario 2, which has an $a_{11} = 1$, depicts a volume with all fibers aligned in the print direction.

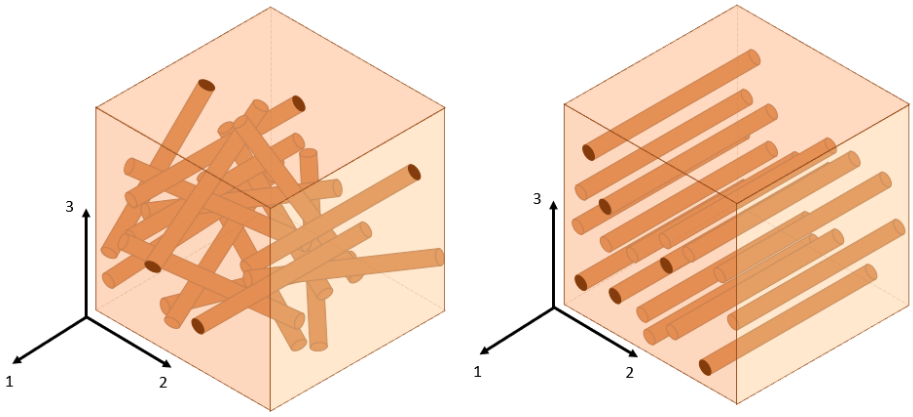

Figure 59. Orientation tensor examples described graphically with two case scenarios. (left) Describes the scenario with $a_{11} = a_{22} = a_{33} = 1/3$, and (right) depicts the scenario with $a_{11} = 1, a_{22} = a_{33} = 0$

The schematic below (Figure 60) depicts the conventional FFF 3D printing process, whereas the orientation in which fibers are placed within the extrudate is portrayed graphically. Mulholland and coworkers showed that preferential orientation is in fact achieved when printing in conventional FFF 3D printers.

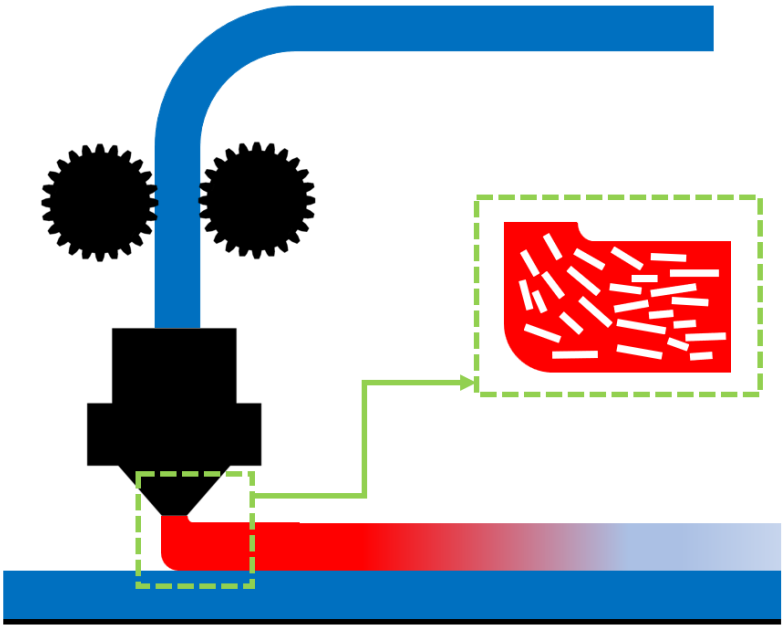

Figure 60. Graphical depiction of the conventional FFF 3D printing process

It was observed by the researchers that the majority of the fibers oriented in the printing direction [119], similar to what was observed in the viscous heating 3D printer while maintaining rotation of the nozzle disabled (Figure 61). It can be seen that the fiber orientation analysis for the nylon glass-fiber reinforced tensile testing coupon resulted in the majority of the fibers being oriented in the 1-direction, signaling that the fibers are primarily pointing in the printing direction.

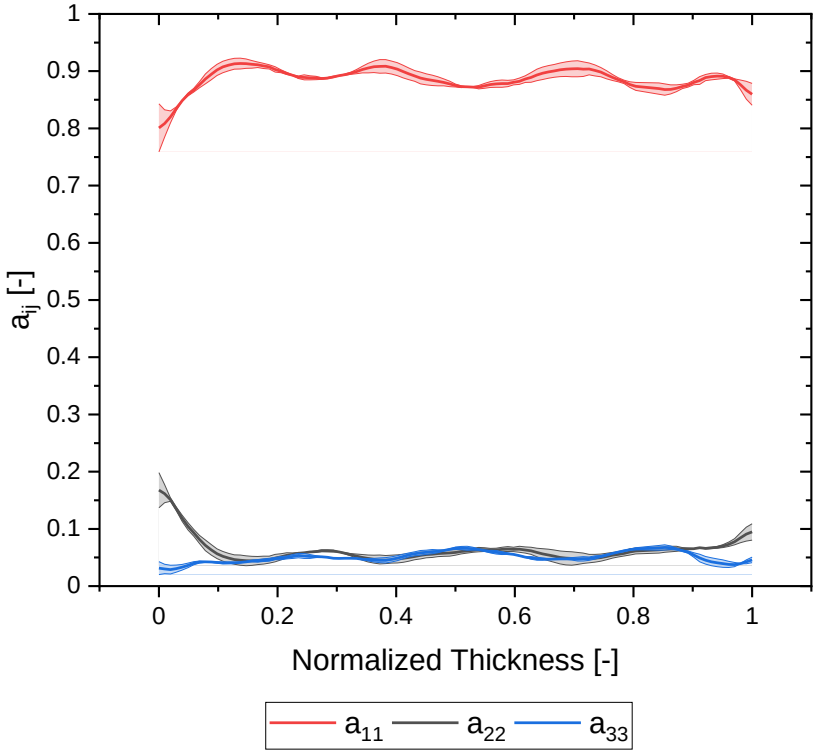

Figure 61. Fiber orientation distribution for a 3D printed specimen with rotation of the nozzle disabled.

The purpose of this section is to display the effects of a rotating nozzle on fiber orientation distribution. As mentioned above, the first layer was printed with the nozzle rotation disabled, and it can be clearly seen in an example analysis below (Figure 62) how the orientation tensor (a_{11}) reaches higher values within the gray region of the plot, compared to the rest of the plot. Again, it should be noted that the grey region represents the 1st layer of the print which has the nozzle in a stationary position.

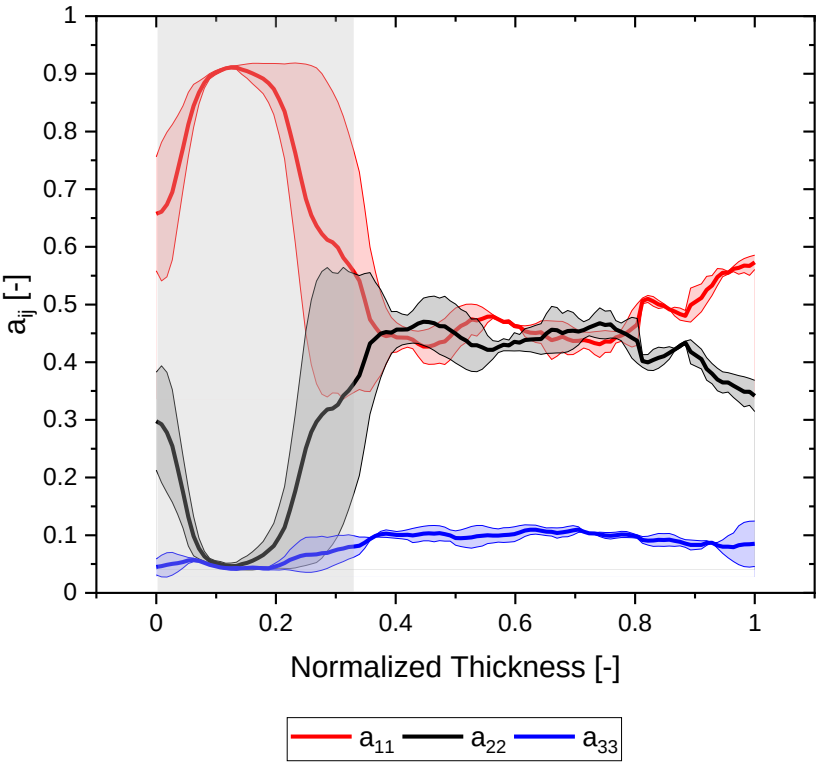

Figure 62. Orientation analysis of a 3D printed specimen with rotation of the nozzle enabled for the last 2-layers of printing.

Unlike the experiments where rotation is disabled and the majority of the fibers orient in the shear direction (extrusion direction) during the manufacturing process, the transition to a less anisotropic part begins as the rotation of the nozzle is enabled. The mentioned isotropic microstructural properties are evident within the fiber orientation distribution as the a_{11}(print direction) and a_{22} (cross-bead direction) fall within a similar order of magnitude. Both orientation tensors hover near the 0.4 value, while the a_{33} (thickness direction) orientation tensor slightly increases to ~0.09.

The drastic transition from an a_{11}-dominated part to a 3D printed part which possesses balanced a_{11} and a_{22} orientation tensors is attributed to the rotation of the nozzle constantly changing its 1-direction axis as it is constantly rotating at elevated RPMs. Assuming a print speed of 60 mm/s and a nozzle rotational speed of 6000 RPMs, this would result in the nozzle achieving 100 full rotations after every 1 millimeter of travel. By reaching a high number of rotations per millimeter of travel, the nozzle has sufficient time to deposit material in a radial manner, ultimately ensuring that the fibers are aligned in a random fashion within the 1-direction and 2-direction. For that

reason, it is apparent that there is a lack of direct correlation between RPMs, print temperature and print speed with fiber orientation within the executed design of experiments. This random alignment of fibers is not the case when RPMs are quite low. When RPMs are lower in comparison to the linear travel speed of the print head, the influence of rotation on additives is more apparent [126]. This statement can be verified in Figure 63 below which shows the print direction fiber orientation (a_{11}) of experiments with rotation enabled represented as red circles. As a benchmark, the experiments without rotation are represented as the dark gray band where it can be seen that the a_{11}orientation tensor reaches values near 0.9.

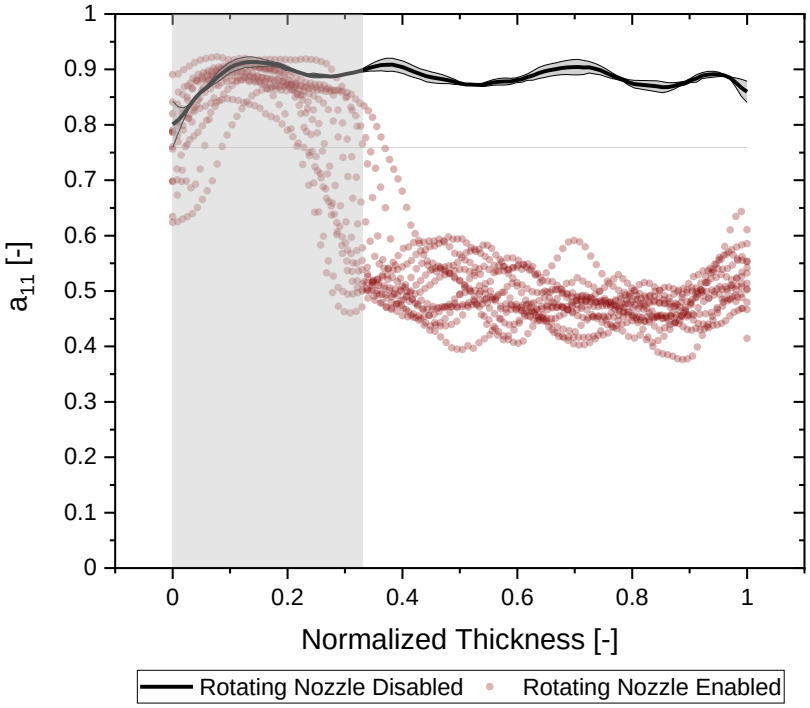

Figure 63. The a_{11} orientation tensor for all 3D printed samples with the rotating nozzle enabled compared against the a_{11} orientation tensor of a 3D printed sample with a stationary nozzle.

Confirming that a rotating nozzle produces a less anisotropic part regarding fiber microstructural properties, it is important to show how the evolved fiber orientation due to the rotating nozzle influences mechanical performance. As stated above, poor bead adhesion suppresses mechanical properties of 3D printed parts, therefore, the mechanical property evaluation of parts is to be discussed in a future section within this document.

Rotating Nozzle Effects on Fiber Length Degradation

There is extensive evidence showing that the fiber length distribution of fiber-reinforced composites has a high correlation with mechanical properties. As the name suggests, reinforcement refers to the added stiffness in the direction of the fiber, and ensuring the fiber length is maintained during processing ensures that higher mechanical properties are preserved [114, 125, 127]. For that reason, studying the influence of the rotating nozzle on fiber length degradation during the 3D printing process needs to be investigated to ensure optimal processing conditions are used which minimize fiber length degradation.

Manually measuring fiber length within discontinuous fiber composites is a time-consuming process as one cubic centimeter sample may contain millions of fibers [128]. By employing the fiber length measurement technique developed at the Polymer Engineering Center at the University of Wisconsin-Madison, measuring 10,000 to 100,000 fibers has become a straightforward and automated process as the pyrolyzed sample leaves behind lose fibers capable of being counted computationally [128]. The loose fibers are dispersed onto an optical glass sheet by using a custom chamber and an ionized air stream. Once scanned, the image undergoes thresholding using Photoshop and then analyzed using the Marching Ball algorithm based on the work of Wang [129], the results are reported using average values L_N and L_W, which represent the number-average fiber length and the weight-average fiber length, respectively. Both average fiber length values are expressed as

$$L_N = \frac{\sum N_i l_i}{\sum N_i} \tag{17}$$

and the weight-average fiber length L_W as

$$L_W = \frac{\sum N_i l_i^2}{\sum N_i} \tag{18}$$

Researchers have reported that one of the largest influences to fiber breakage during the FFF 3D printing process is attributed to restrictive nozzle [130], but that overall, the conventional FFF 3D printing process does not cause significant fiber breakage during the extrusion-based 3D printing process [118,130]. Yang and coworkers observed an 11% decrease in fiber length when comparing the original filament to the extruded bead using a 0.4 mm diameter nozzle. A similar observation

was also seen within our viscous heating 3D printer print trials while disabling rotation of the nozzle, whereas the initial number-average fiber length of 0.266 mm decreased by 15% to a final value of 0.227 mm. It can be seen in Figure 64.a below that varying print temperatures at a print speed of 60 mm/s does not have strong influence on fiber breakage when rotation of the nozzle is disabled. Now, comparing prints done at 260°C with rotation of the nozzle enabled and at 2x the print speed, we can appreciate from those trials that there is no significant decrease in fiber length as we reach 3500 RPMs and as we double the average print speed (Figure 64.b). This achievement is important as the goal of this study is to accelerate 3D printing speeds, all while maintaining or improving on those baseline properties acquired from a non-rotating nozzle FFF 3D printer.

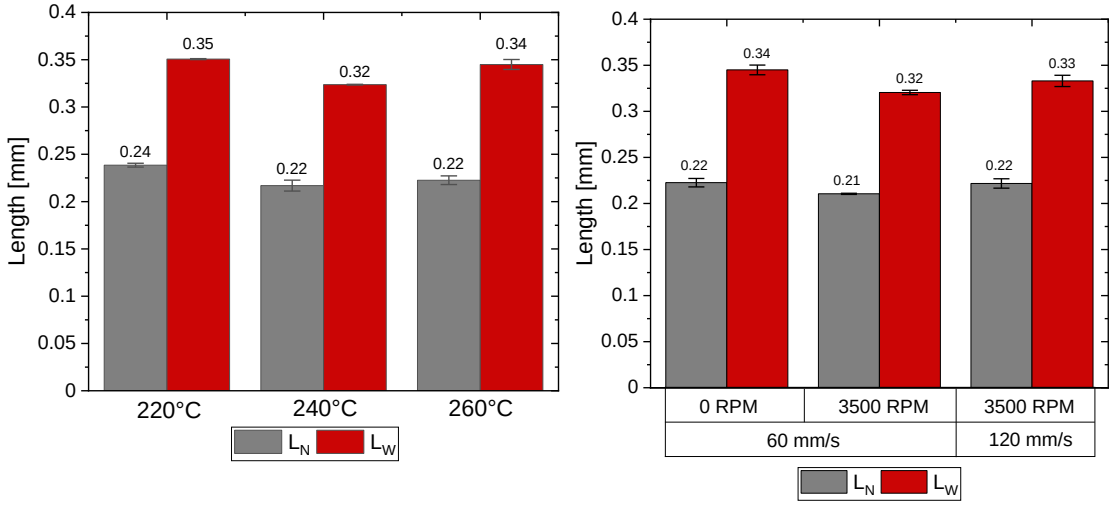

(a) (b)

Figure 64. (a) Fiber length at distinct print temperatures with rotation disabled, and (b) print trials at 260°C while varying rotational speed of the nozzle and print speed

Now, investigating the influence of higher nozzle rotational speeds is also crucial as it is understood that increasing RPMs will drastically reduce the forces necessary for extrusion. Higher RPMs essentially allow for faster filament speeds which translates to faster print speeds. Unfortunately, it can be seen from Figure 65 below that fiber attrition is more prevalent when RPMs surpass 3500 RPMs. When comparing 0 RPMs to 5000 RPMs, it becomes apparent that a 22% decrease in fiber length is experienced. This observation is only seen for this single temperature experimental data point and for one specific print speed. A more profound study is required to ensure this trend is visible at various print temperatures and print speeds.

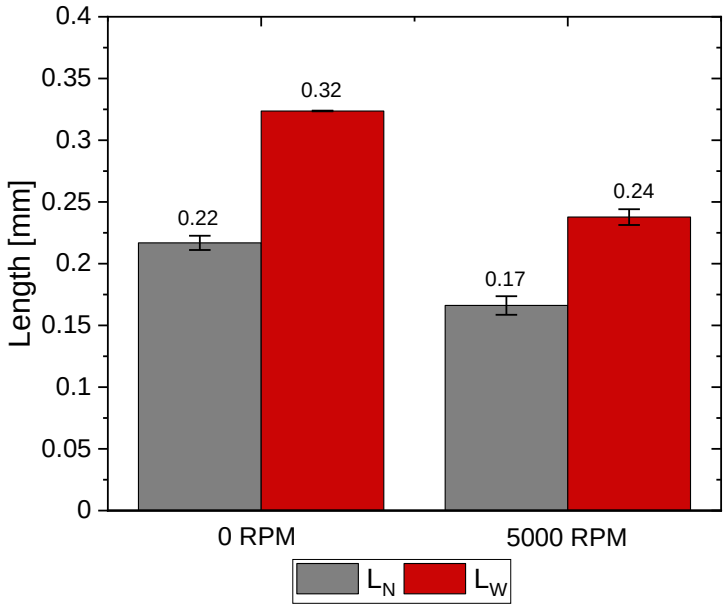

Figure 65. Fiber attrition present in the viscous heating 3D printer at 5000 RPMs.

4.4 Mechanical Performance of 3D Printed Components

It is well known that the performance of an FFF 3D printed tensile testing coupon does not reach similar properties to an injection molded tensile testing coupon. The discrepancy present between both parts manufactured by distinct methods is a result of multiple variables and the relationship between printing parameters and final part properties are still not fully understood. During traditional FFF 3D printing of fiber-reinforced parts, it is known that adhesion between adjacent beads is reduced as fibers present at the bead surface prevents proper adhesion to the adjacent bead [131-132]. Figure 66 clearly illustrates the occurrence of 2 adjacent beads where we can distinguish voids between both beads and that fibers are in fact present at the joint between the beads.

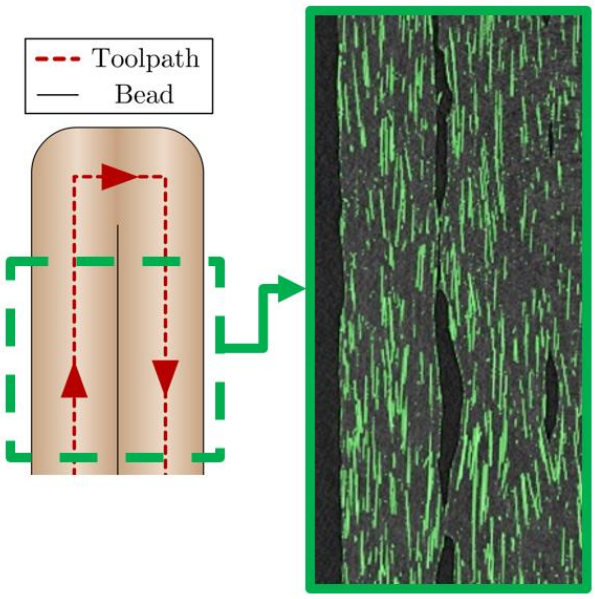

Figure 66. Cross-sectional image of two beads 3D printed with rotation of the nozzle disabled, clearly showing the alignment of fibers in the print direction.

Within Figure 66, the toolpath is denoted as the 1-direction (print direction), therefore it is known that the mechanical properties in the 1-direction will be superior to those in the 2-direction (cross-bead direction). In a perfect case scenario, loading would only occur in the 1-direction and the 3D printed part would perform great, but unfortunately, the reality of manufactured components is that they will undergo various loading types and from loads originating from various directions, therefore, the probability of part failure is quite high when large loads are being experienced in the 2-direction. For this reason, it is crucial that the 2-direction is reinforced in some manner. This section evaluates the mechanical performance in the cross-bead direction by comparing two print orientations (Figure 67): 0° which represents the scenario when loading is parallel to the print direction, and 90° which is when loading is perpendicular to print direction.

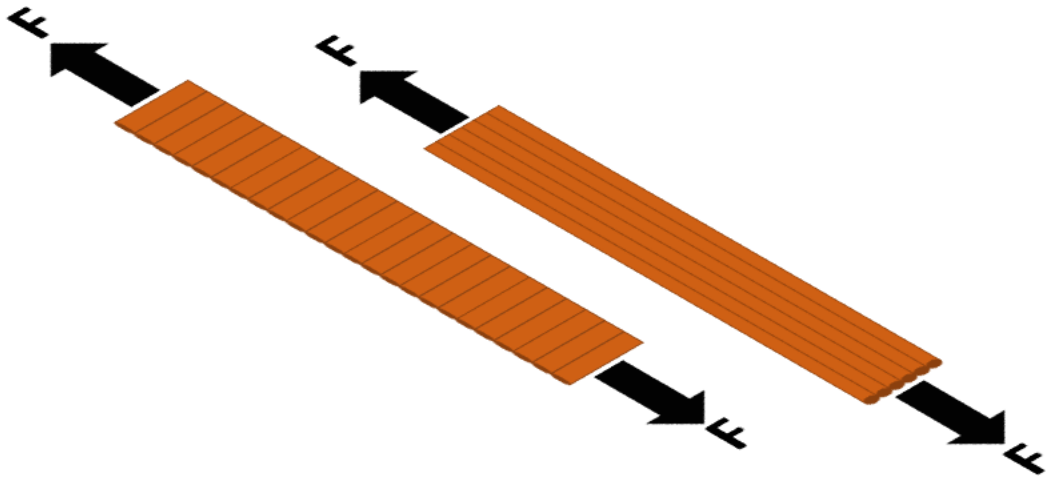

Figure 67. The bead orientations for two testing scenarios where the left is classified as the 90° print and the right figure is the 0° print.

Evaluation of the mechanical properties was done by adapting the ASTM D673 standard in which the printing process mimics the 3-layer procedure done for the fiber microstructure characterization. For the analysis, the ultimate tensile strength reached during testing was reported to gain insight into the effects of nozzle rotation on mechanical performance as bead adhesion is one of the underlying reasons why implementation of FFF within mass manufacturing is not a common practice.

It is expected that the 0° 0 RPM tests will have the highest ultimate tensile strength as ~90% of the fibers will be oriented in the load direction, but it is also hypothesized that the 90° 0 RPM test will have the weakest properties because there will effectively be no reinforcement in the cross-bead direction. The goal of this study is to present results which portray an improved overall performance, which translates in slightly diminished 0° sample performance but increased 90° sample performance by introducing rotation of the nozzle. By presenting an improved overall performance of the 3D printed part, this is working towards solving the second bottleneck of FFF 3D printing which is highly anisotropic parts leading to part failure in the cross-bead direction.

4.4.1 Influence of Rotating Nozzle on Ultimate Tensile Strength

Upon inspection of the full three-dimensional reconstruction of the μCT images, it can be seen from Figure 68.a below that there is preferential orientation within the 0 RPM 3D printed part. All

fibers within Figure 68.a can be seen oriented in the 1-direction (print direction), whereas a part printed with nozzle rotation enabled can be seen to have fibers oriented in all directions within the printing plane (Figure 68.b). Additionally, an interesting occurrence is observed (Figure 69) in that the fibers are seen migrating towards the adjacent bead when rotation is enabled, providing supporting evidence that there will be reinforcement in the 2-direction. The mentioned reinforcement is theorized to improve the 90° orientation sample performance as bead adhesion should hypothetically be improved.

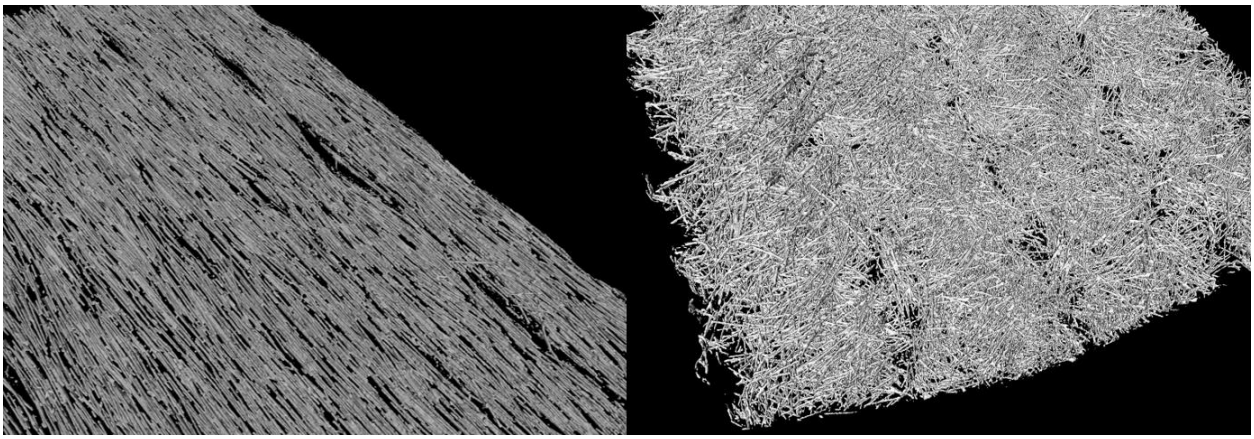

(a) (b)

Figure 68. (a) three-dimensional image reconstruction of the sample produced with rotation of the nozzle disabled. (b) the sample produced with rotation of the nozzle enabled.

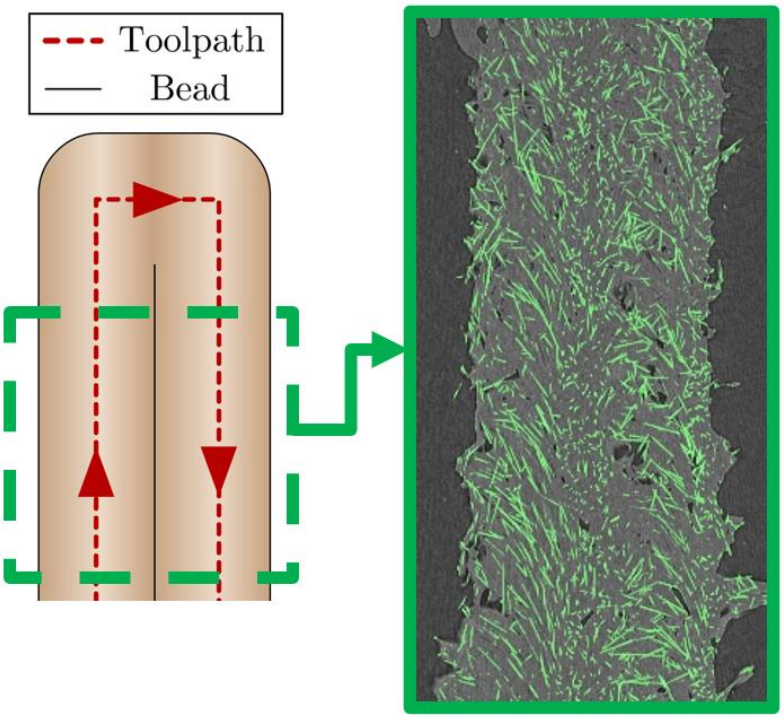

Figure 69. Fiber migration towards the adjacent bead occurring when rotation is activated.

After conducting testing, it can be seen that consistent results are acquired for all 90° orientation tests where 29.5 MPa is the average ultimate tensile strength during transient testing for all four testing conditions. It can also be seen in Figure 70 that the faster print speed of 120 mm/s is still able to reach similar mechanical testing properties to those printed at half the print speed. It should be reminded that average print speeds are near 60 mm/s, therefore, printing at 120 mm/s provides supporting evidence that this rotating nozzle mechanism can in fact be used to accelerate the 3D printing process within FFF.

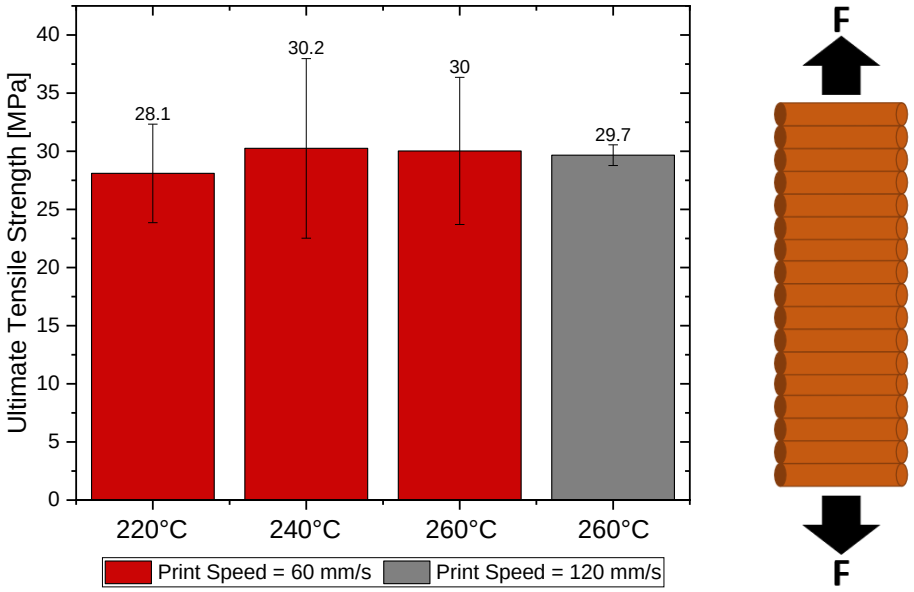

Figure 70. Testing results for the 90° samples realized in accordance with ASTM D673.

Now, comparing mechanical properties from samples printed with varying print temperatures, print orientations and rotational speeds, it can be appreciated that the 0° 0 RPM samples in fact result in the sample with highest mechanical strength (Figure 71). Ultimately a consequence of ~90% of the fibers aligned in the load direction, it should be expected that no other sample will attain superior mechanical properties.

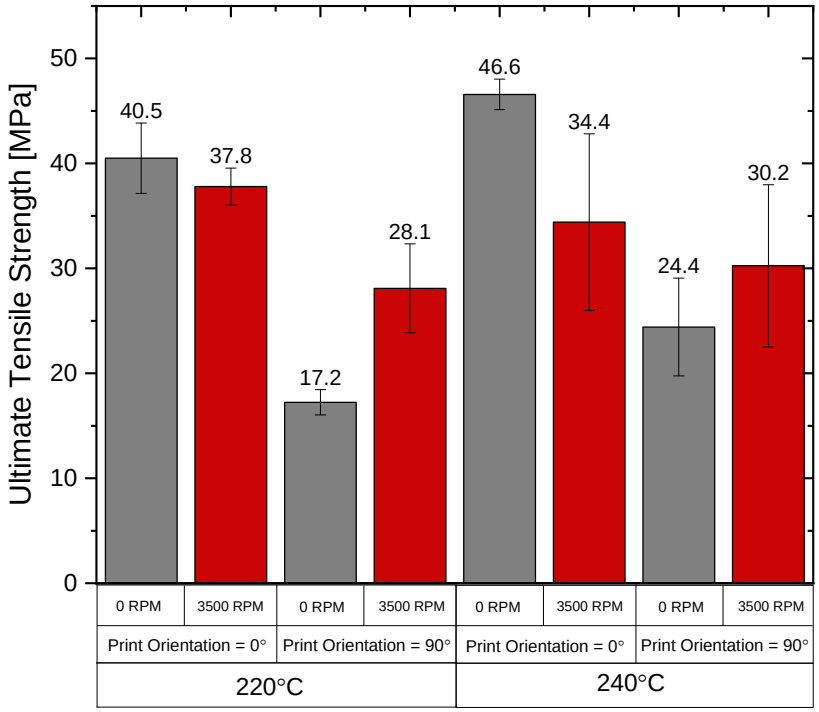

Figure 71. Mechanical tests of all 3D printed components showing the positive effects on overall mechanical performance of 3D printed parts.

Relating samples from both printing temperatures, it can be seen that enabling nozzle rotation reduces the 0° sample strength by 17% but that the 90° sample strength is improved by 40%. As mentioned, it was expected to observe a decrease in 0° sample performance as only 40-45% of the fibers are oriented in direction of the applied load compared to a 0 RPM test which results in ~90% of the fibers oriented in the direction of loading. Therefore, the hypothesis that overall performance was improved has been verified as the overall performance was enhanced by 23%, with adjacent beads experiencing reinforcement effects due to fiber migration and fiber orientation in the cross-bead direction.

5. Summary

5.1 Contributions

To this day, modeling material behavior of polymeric systems is a complex task which is highly influenced by numerous variables. For example, modeling mechanical response requires one to take into consideration the types of inclusions within the system, the rate at which loading is occurring, temperature, and pressure to name a few. The dependence on an abundant number of variables results in an engineering problem deemed too complex for traditional modeling approaches, such as FEA and physical models, to mention a few. For that reason, data-driven modeling has become a powerful tool to predict polymer behavior because of its ability to learn quickly from data, if used appropriately.

This dissertation explored three major strategies to solve polymer engineering problems via data-driven modeling. The first chapter involved using an **image-based machine learning** approach to predict injection molding part defects of highly viscoelastic polymer blends. The defects arise from rheological instabilities from the cross-linked material which has not had enough time to relax. Therefore, the development of a model which uses images, rheological parameters and material composition as inputs informed the user of the probability of molding defects with 92.4% cross-validation (CV) accuracy.

The second chapter explored was in the use of **machine learning for materials development** of novel high-performance materials, and the implementation for reverse engineering of materials based on target properties. Polymer formulation methodologies implemented within industry primarily implicate a high dependence on the formulator's experience as it involves an educated guess-and-check process. The data-driven algorithm developed predicted the following with 100%

5-fold CV accuracy: short-term mechanical behavior, long-term viscoelastic behavior, transient and dynamic properties from only 11 experimental blends.

The final chapter involved the unification of both above-mentioned methods to create a **machine learning tool capable of informing the user of optimal processing conditions** for a novel patented fused filament fabrication (FFF) 3D printer capable of significantly accelerating melting by leveraging the efficiency of viscous dissipation. The response surface methodology is capable of informing the user of the processing window and the forces present during the 3D printing process with 88% accuracy. In conjunction with in-situ imaging, processing parameters and rheological information, the goal of this long-term study is to assess part quality in real-time to allow for process optimization or for user intervention, depending on the severity of the issue.

Data-driven modeling, such as Machine learning (ML), if implemented in a non-black-box fashion, can accelerate materials development and overall polymer process optimization. The result of this work provides a tool for future engineers and researchers to merge polymer science with data-driven modeling to predict complex relationships between processing parameters, rheology, viscoelasticity, and material composition.

5.2 Recommendations for Future Work

Sections 4.1 to 4.4 has provided evidence that the rotating nozzle is capable of the following:

- Decreasing pushing forces necessary for filament to be extruded through the rotating nozzle.
- Decrease the level of anisotropy within a 3D printed part, improving the overall mechanical performance of the 3D printed components.
- Allow for faster filament speeds, translating to shorter print times.

Although faster printing speeds and improved level of anisotropy are crucial for full adoption of additive manufacturing at an industrial level, optimizing part quality is also a leading challenge within industry. For that reason, a real-time diagnostics system is proposed within this work to assess the quality of the extrudate and to classify whether or not under-extrusion is being experienced. This assessment tool is achievable by using convoluted neural networks, a common machine learning algorithm used in image recognition applications.

Yolo version 4 is a machine learning algorithm capable of single-object detection in which the number 1 translates to *object detected* and the number 0 translates to *object not detected*. It implements convoluted neural networks and the pretrained resnet50 model facilitates faster convergence to the final model weights and biases. Yolo v4 has preliminarily been implemented within this 3D printer by using two cameras positioned towards the rotating nozzle structure with the 3D printed component within its viewpoint as well. As under extrusion may appear as voids in the final 3D printed part, to reduce the risk of infill density being misclassified as the result from under extrusion, extensive amounts of training datapoints are needed to accurately predict small-scale occurrences such as under extrusion. Training data will need to include images of 3D printed components that have under extrusion with varying infill densities. Enriching the current data set will ensure that the algorithm has enough data to learn. This is all to make sure that the defect-prediction tool is capable of distinguishing the difference between voids caused by under extrusion and infill density.

Provided that proper classification is achievable, in order to facilitate the development of a *Smart 3D printer*, the following tasks are required:

1) Producing a representative processing window for a wide range of materials by conducting print trials with varying RPM, print temperature, and filament speeds.

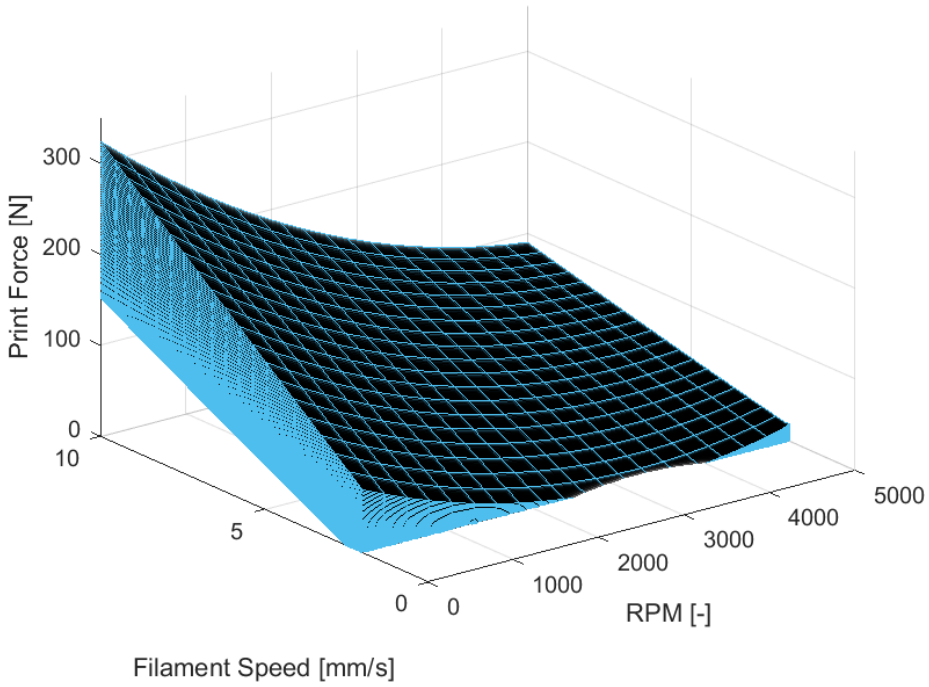

Figure 72. The processing window for the viscous heating 3D printer represented as a volume created from the RSM analysis.

By implementing data-driven modeling, one is capable of extrapolating synthetic experiments and informing the user of the expected outcome. This in turn allows for one to have an informed decision in regard to selecting the upcoming design of experiments. Multiple materials are required to be tested because of the diverse material properties (for example: thermal conductivity, friction and thermal transitions) that polymers exhibit.

2) Characterization the of microstructural properties for the design of experiments to capture the influence of print parameters on microstructure.

This finding is crucial as it is expected that specific processing parameters will lead to a part with higher amounts of voids. It is theorized that higher RPMs will lead to faster print times but that it will also lead to higher amounts of vibration, resulting in a loss in mechanical properties. It would be ideal to capture the processing parameter ranges in which the there is a higher probability for improved mechanical performance.

3) Development of failure criteria for the respective processing parameters.

It should be expected that specific processing conditions, such as extremely high RPMs and filament speeds will have a higher risk of producing extrusion defects as full relaxation of the extrudate will not be attainable. For that reason, it is beneficial to characterize an overall range in which the processing parameters result in a low probability of defects present within the 3D printed part. By superimposing the mechanical properties for each respective processing condition seen in Figure 72, one would have a volume which represents the optimal processing conditions which will result in optimal mechanical properties.

4) Use optimal conditions as the controller for the autonomous 3D printer setup.

For an autonomous system to adjust a processing parameter during manufacturing, the system must know beforehand what conditions will result in an improved extrudate quality. By having the representative volume mentioned in the previous section, the controller will know which areas within the volume have a higher probability of improving the print quality. It will be up to the image-based machine learning algorithm to detect via both cameras when defects occur and then the controller will inform the 3D printer of the specific filament speed adjustment needed for improved extrusion quality.

The proposed work would result in a smart 3D printer capable of adjusting processing parameters during the manufacturing process to ensure optimal parts are manufactured with this new technology. This will also result in an FFF 3D printing process capable of drastically reducing manufacturing lead times and improving part quality by incorporating a rotating nozzle within machine construction.

5.3 Research Products

Patents

Submitted Patent US23023023 – Rotating Nozzle Structure and Method

Referred Journal Publications

Román, A. J., et al., “Natural Rubber Blend Optimization via Data-Driven Modeling: The Implementation for Reverse Engineering,” *Polymers*, 2022, 14, 2262, DOI: 10.3390/polym14112262

Román, A. J., et al., “Neural network feature and architecture optimization for injection molding Surface defect prediction of Model polypropylene,” *Polymer Engineering & Science*, 2021, DOI: 10.1002/pen.25765

Román, A. J., et al., “Optimización de la formulación del caucho natural mediante inteligencia artificial, Parte 1”, *Revista de la Sociedad Latinoamericana Tecnológica de Caucho,* 2022

Román, A. J., et al., “Optimización de la formulación del caucho natural mediante inteligencia artificial, Parte 2”, *Revista de la Sociedad Latinoamericana Tecnológica de Caucho,* 2023

Román, A. J., et al., “Optimización de la formulación del caucho natural mediante inteligencia artificial, Parte 3”, *Revista de la Sociedad Latinoamericana Tecnológica de Caucho,* 2023

Román, A. J., et al., “Optimización de la formulación del caucho natural mediante inteligencia artificial, Parte 4”, *Revista de la Sociedad Latinoamericana Tecnológica de Caucho,* 2023

Shotwell, D., Román, A. J., et al., “Effect of Static Mixer on Fiber Orientation of Injection Molded Fiber-reinforced Composites”, *SPE Polymers,* 2022, DOI: 10.1002/pls2.10080

Poompiew, N., Román, A. J., et al., “3D Printable Carbon Nanotube Composites for Wearable Strain Sensors: Enhancing Mechanical and Electrical Properties”, *Journal of Science: Advanced Materials and Devices,* 2023, DOI: 10.1016/j.jsamd.2023.100546

Kanabenja, W., Román, A. J., et al., “3D Printing Filaments from Plasticized Polyhydroxybutyrate/Polylactic acid Blends Reinforced with Hydroxyapatite”, *Additive Manufacturing,* 2022, DOI: 10.1016/j.addma.2022.103130

Zhao, J., Román, A. J., et al., “Effective Mechanical Properties of Injection Molded Short-Fiber Reinforced Composites Using Periodic Homogenization”, *Advanced Composites and Hybrid Materials,* 2022, DOI: 10.1007/s42114-022-00518-y

Yang, H., Román, A. J., et al., “Cell morphologies, mechanical properties, and fiber orientation of glass fiber-reinforced polyamide composites: Influence of subcritical gas-laden pellet injection molding foaming technology,” *Physics of Fluids*, vol. 34, no. 1, p. 013101, 2022, DOI: 10.1063/5.0078055

Román, A. J., et al., “Influence of plantation climate and storage time on thermal and viscoelastic properties of Natural Rubber”, *AIMS Bioengineering*, 2021, DOI: 10.3934/bioeng.2021010

Rodriguez, J.C., Osswald, T.A., Garcia-Estela, J., Román, A.J., “Environmentally safe preservation and stabilization of natural rubber latex in an acidic environment, *SPE Polymers*, vol. 4 (3), 2023, DOI: 10.1002/pls2.10089

Perez, H.S., Román, A.J., Bechara, A., “Effect of Fiber Bundle Morphology on Fiber Dispersion for Long Fiber-Reinforced Thermoplastics”, *Polymers*, 15 (13), 2023, DOI: 0.3390/polym15132790

Román, A.J., Dibisa, O., Pardo, G., Rodríguez, J.C., Osswald, T.A., “Evaluation of an ammonia-free natural rubber latex adhesive”, *SPE Polymers*, 2023, DOI: 10.1002/pls2.10103

Poompiew, N. Jirawatanaporn, N., Okhawilai, M., Qin, J. Román, A.J., Aumnate, C., Osswald, T.A., Potiyaraj, P., “3D-printed polyacrylamide-based hydrogel polymer electrolytes for flexible zinc-ion battery”, *Electrochimica Acta*, 143076, DOI: 10.1016/j.electacta.2023.143076

Conference Proceedings

Estela-Garcia, J. Román, A.J. and Osswald, T.A., “Material Property Prediction of Recycled Polypropylene via Data-Driven Modeling”, ”, Society of Plastics Engineers, Automotive Composites Conference & Exhibition, Novi Michigan 2023

Román, A. J., et al., “Viscous Heating Fused Filament Fabrication: Accelerating Print Speeds” Polymer Processing Society Annual Conference- 38, St. Gallen, Switzerland 2023

Román, A. J., et al., "Viscoelastic Behavior Prediction of Natural Rubber Blends via Neural Networks and its Application for Reverse Engineering" Polymer Processing Society Annual Conference- 37, Fukuoka Japan 2022

Román, A. J., et al., "Understanding Fiber Dispersion in Couette Rheometer via Machine Learning and X-Ray Imaging", Society of Plastics Engineers, Automotive Composites Conference & Exhibition, Novi Michigan 2021 *Best Poster Award Winner*

Román, A. J., et al., "Characterization of Novel Ammonia-Free Natural Rubber Latex and Machine Learning Implementation for Material Property Prediction", Latin American Natural Rubber Technological Conference, Madison Wisconsin 2021

Román, A. J., et al., "Fiber Orientation Analysis Algorithm Development for Implementation within Microstructural-driven Mechanics Modeling", Automotive Composites Conference & Exhibition, Novi Michigan 2022 (3rd Place Paper Award)

Perez, H., Román, A. J., et al., "The Effect of Fiber Bundle Morphology on Dispersion for Long Fiber-reinforced Thermoplastics", Automotive Composites Conference & Exhibition, Novi Michigan 2021

Román, A. J., et al., "Viscoelastic and Thermal Characterization of Raw Unvulcanized Natural Rubber and the Influence of Plantation Climate", Latin American Natural Rubber Technological Conference, Madison Wisconsin 2020

Osswald, T.A., Román, A. J., et al., "Rheological Behavior of Raw Unvulcanized Natural Rubber", Latin American Natural Rubber Technological Conference, Querétaro Mexico 2019

Román, A. J., et al., "Fabrication Method Effects on Mechanical Performance of Carbon Reinforced Parts and Micromechanics Model Validation", Society of Plastics Engineers, Automotive Composites Conference & Exhibition, Novi Michigan 2019

Supervised Works

During the course of this research, the author has been responsible for supervising the following work:

Konstantin Bauer. “Modification of the Slit Method Orientation Analysis Algorithm to allow for 3D Fiber Orientation Distribution Analysis”, Master thesis. Freidrich-Alexander University at ErlangenNuremberg, Erlangen, Germany

List of References

[1] By: IBM Cloud Education, “What is machine learning?,” IBM. [Online]. Available: https://www.ibm.com/cloud/learn/machine-learning. [Accessed: 09-Oct-2022].

[2] Y.W. Chen, C.J. Lin, “Combining SVMs with Various Feature Selection Strategies. In: Guyon, I., Nikravesh, M., Gunn, S., Zadeh, L.A. (eds) Feature Extraction. Studies in Fuzziness and Soft Computing”, vol 207. Springer, Berlin, Heidelberg. https://doi.org/10.1007/978-3-540-35488-8_13 (2006)

[3] Y.W. Chang, C.J. Lin, “Feature Ranking using linear SVM” JMLR: Workshop and Conference Proceedings, vol 3, pp 53-64 (2008)

[4] T. Haifley, "Linear logistic regression: an introduction," IEEE International Integrated Reliability Workshop Final Report, 2002., pp. 184-187, doi: 10.1109/IRWS.2002.1194264 (2002)

[5] “Linear regression vs logistic regression - javatpoint,” www.javatpoint.com. [Online]. Available: https://www.javatpoint.com/linear-regression-vs-logistic-regression-in-machine-

learning#:~:text=Linear%20regression%20is%20used%20to,given%20set%20of%20independent%20variables. [Accessed: 09-Oct-2022].

[6] A. El Magri, K. El Mabrouk, S. Vaudreuil, and M. Ebn Touhami, "Experimental investigation and optimization of printing parameters of 3D printed polyphenylene sulfide through response surface methodology," *J. Appl. Polym. Sci.*, vol. 138, no. 1, pp. 1–13 doi: 10.1002/app.49625 (2020)

[7] M. Waseem *et al.*, "Multi-response optimization of tensile creep behavior of PLA 3D printed parts using categorical response surface methodology," *Polymers (Basel).*, vol. 12, no. 12, pp. 1–16, doi: 10.3390/polym12122962 (2020)

[8] S. Srewaradachpisal, C. Dechwayukul, S. Chatpun, R. J. Spontak, and W. Thongruang, "Optimization of the Rubber Formulation for Footwear Applications from the Response Surface Method," Polymers, vol. 12, no. 9, p. 2032, doi: 10.3390/polym12092032 (2020)

[9] Coefficients Table for Analyze Response Surface Design. Minitab. Available online: https://support.minitab.com/en-us/minitab/18/help-and-how-to/modeling-statistics/doe/how-to/response-surface/analyze-response-surface-design/interpret-the-results/all-statistics-and-graphs/coefficients-table/ (accessed on 5 May 2022).

[10] Effects Plots for Analyze Response Surface Design. Minitab. Available online: https://support.minitab.com/en-us/minitab/18/help-and-how-to/modeling-statistics/doe/how-to/response-surface/analyze-response-surface-design/interpret-the-results/all-statistics-and-graphs/effects-plots/ (accessed on 5 May2022).

[11] J. Cervantes, F. Garcia-Lamont, L. Rodriguez-Mazahua, A. Lopez, "A comprehensive survey on support vector machine classification: Applications, challenges and trends", Neurocomputing vol 408, pp 189-215, https://doi.org/10.1016/j.neucom.2019.10.118 (2020)

[12] M.N. Murty, R. Raghava, "Kernel-based SVM. In: Support Vector Machines and Perceptrons" Springerbriefs in Computer Science, https://doi.org/10.1007/978-3-319-41063-0_5 (2016)

[13] M. Jacob, S. Thomas, and K. T. Varughese, “Mechanical properties of sisal/oil palm hybrid fiber reinforced natural rubber composites,” Composites Science and Technology, vol. 64, no. 7-8, pp. 955–965 (2004)

[14] S.S. Choi, B.H. Park, H. Song, “Influence of filler type and content on properties ofstyrene-butadiene rubber (SBR) compound reinforcedwith carbon black or silica”, Polym. Adv. Technologies vol 15 pp 122-127 https://doi.org/10.1002/app.22287 (2005)

[15] By: IBM Cloud Education, “What are neural networks?,” IBM. [Online]. Available: https://www.ibm.com/cloud/learn/neural-networks. [Accessed: 09-Oct-2022].

[16] I. Goodfellow, Y. Bengio, and A. Courville, Deep learning. Cambridge, MA: The MIT Press (2017)

[17] Rumelhart, D.E.; Durbin, R.; Golden, R.; Chauvin, Y.; “Backpropagation: Theory, Architecture, and Applications,” Lawrence Erlbaum Associates (1995)

[18] Rasmussen, C.E. Gaussian Processes in machine learning. In Lecture Notes in Computer Science; Max Planck Institute for Bio-logical Cybernetics: Tübingen, Germany; Volume 3176, pp. 63–71. https://doi.org/10.1007/978-3-540-28650-9_4 (2004)

[19] V. L. Popov, M. Heß, and E. Willert, Handbook of Contact Mechanics, Springer Berlin, Hedelberg (2019)

[20] Tseng, H-C; Chang, R-K and Hsu, C-H; “Numerical prediction of fiber orientation and mechanical performance for short/long glass and carbon fiber-reinforced composites”, Composites science and technology, vol.144, pp 51-56, doi:10.1016/j.compscitech.(2017)

[21] Chiu, H-S; Chou, Y-Y; Yang, W-L; Hsu, C-H; Masahi, Y., “Numerical simulation and experimental investigation of fiber in injection molding” SPE ANTEC (2007)

[22] P. K. D. V. Yarlagadda, "Development of an Integrated Neural Network System for Prediction of Process Parameters in Metal Injection Moulding," Journal of Matl. Procc. Technology, vol. 130-131, pp. 315-320, doi:10.1016/S0924-0136(02)00738-0 (2022)

[23] A. C. B. Bogaerds, “Stability analysis of viscoelastic flows,” vol. 45, p. 5600 (2002)

[24] B. Patham, P. Papworth, K. Jayaraman, C. Shu, and M. D. Wolkowicz, “Flow marks in injection molding of polypropylene and ethylene-propylene elastomer blends: Analysis of morphology and rheology,” J. Appl. Polym. Sci., vol. 96, no. 2, pp. 423–434 doi: 10.1002/app.21459 (2005)

[25] G. Iannuzzi, A. Boldizar, and M. Rigdahl, “Characterization of Flow-Induced Surface Defects in Injection Moulded Components – Case Studies,” Ann. Trans. Nord. Rheol. Soc., vol. 17, pp. 157–165, (2009)

[26] R. Y. Chang and B. D. Tsaur, “Experimental and theoretical studies of shrinkage, warpage, and sink marks of crystalline polymer injection molded parts,” Polym. Eng. Sci., vol. 35, no. 15, pp. 1222–1230, doi: 10.1002/pen.760351505 (1995)

[27] L. Mathieu et al., “Flow marks in injection molding of PP - Influence of processing conditions and formation in fountain flow,” Int. Polym. Process., vol. 16, no. 4, pp. 404–411, [Online]. Available: https://www.cheric.org/research/tech/periodicals/view.php?seq=1005235 (2001)

[28] A. Alvarado-Iniesta, D. J. Valles-Rosales, J. L. García-Alcaraz, and A. Maldonado-Macias, “A recurrent neural network for warpage prediction in injection molding,” J. Appl. Res. Technol., vol. 10, no. 6, pp. 912–919, doi: 10.22201/icat.16656423.2012.10.6.351 (2012)

[29] Z. Zhang and K. Friedrich, “Artificial neural networks applied to polymer composites: A review,” Compos. Sci. Technol., vol. 63, no. 14, pp. 2029–2044, doi: 10.1016/S0266-3538(03)00106-4 (2003)

[30] O. I. Abiodun, A. Jantan, A. E. Omolara, K. V. Dada, N. A. E. Mohamed, and H. Arshad, “State-of-the-art in artificial neural network applications: A survey,” Heliyon, vol. 4, no. 11, p. e00938, doi: 10.1016/j.heliyon.2018.e00938 (2018)

[31] A. M. Grillet, A. C. B. Bogaerds, G. W. M. Peters, F. P. T. Baaijens, and M. Bulters, “Numerical analysis of flow mark surface defects in injection molding flow,” J. Rheol. (N. Y. N. Y)., vol. 46, no. 3, pp. 651–669, doi: 10.1122/1.1459419 (2002)

[32] D. Mathivanan, M. Nouby, and R. Vidhya, “Minimization of sink mark defects in injection molding process – Taguchi approach,” Int. J. Eng. Sci. Technol., vol. 2, no. 2, pp. 13–22, doi: 10.4314/ijest.v2i2.59133 (2010)

[33] Y.-M. Deng, D. Zheng, B.-S. Sun, and H.-D. Zhong, “Injection Molding Optimization for Minimizing the Defects of Weld Lines,” Polym. Plast. Technol. Eng., vol. 47, no. 9, pp. 943–952, doi: 10.1080/03602550802274555 (2008)

[34] J. Sreedharan and A. K. Jeevanantham, “Analysis of Shrinkages in ABS Injection Molding Parts for Automobile Applications,” Mater. Today Proc., vol. 5, no. 5, pp. 12744–12749, doi: 10.1016/j.matpr.2018.02.258 (2018)

[35] R. Hussin, R. Saad, R. Hussin, and M. Dawi, "An Optimization of Plastic Injection Molding Parameters Using Taguchi Optimization Method," Asian Transactions on Engineering - ATE ISSN:221-4267, vol. 2, no. 5, pp. 75-80 (2012)

[36] M. Moayyedian, and A. Mamedov, "Multi-objective Optimization of Injection Molding Process for Determination of Feasible Moldability Index," Procedia CIRP, vol. 84, 2019 doi: 10.1016/j.procir.2019.04.213 (2019)

[37] J. Zhu, Z. Qiu, Y. Huang, and W. Huang, "Overview of Injection Molding Process Optimization Techology," Journal of Physics: Conference Series ICAMME 2020, doi:10.1088/1742-6596/1798/012042 (2020)

[38] M. S. Meibadi, A. Vafaeesefat, and F. Sharifi, "Optimization of Plastic Injection Molding Process by Combination of Artificial Neural Network and Genetic Algorithm, Journal of Optimization in Industrial Engineering, vol. 6, no. 13, pp. 49-54, (2013)

[39] Y. Lockner, and C. Hopmann, "Induced Network-Based Transfer Learning in Injection Molding for Process Modelling and Optimization with Artificial Neural Networks, The Int.Journal of Adv. Manuf. Tech., vol. 13, no. 8, doi: 10.3390/su13084120 (2021)

[40] S. M. S. Mukras, "Experimental-Based Optimization of Injection Molding Process Parameters for Short Product Cycle Time, Adv. in Polymer Tech., vol. 2020, doi: 10.1155/2020/1309209 (2020)

[41] C. Fernandes, A. J. Pontes, J. C. Viana, and A. Gaspar-Cunha, "Modelling and Optimization of the Injection-Molding Process: A Review, Adv. Polymer Technology, pp. 429-449, doi: 10.1002/adv.21683 (2018)

[42] D. W. Thurman, J. P. Oberhauser, J. A. Kornfield, and R. A. Ryntz, “Stratified Morphology of a Polypropylene / Elastomer Blend,” Polymer (Guildf)., pp. 2842–2859 (2002)

[43] J. W. Housmans, M. Gahleitner, G. W. M. Peters, and H. E. H. Meijer, “Structure-property relations in molded, nucleated isotactic polypropylene,” Polymer (Guildf)., vol. 50, no. 10, pp. 2304–2319, doi: 10.1016/j.polymer.2009.02.050 (2009)

[44] S. Wu, “Chain structure, phase morphology, and toughness relationships in polymers and blends,” Polym. Eng. Sci., vol. 30, no. 13, pp. 753–761, doi: 10.1002/pen.760301302 (1990)

[45] F. C. Stehling, T. Huff, C. S. Speed, and G. Wissler, “Structure and properties of rubber-modified polypropylene impact blends,” J. Appl. Polym. Sci., vol. 26, no. 8, pp. 2693–2711, doi: 10.1002/app.1981.070260818 (1981)

[46] J. Z. Liang and R. K. Y. Li, “Rubber toughening in polypropylene: A review,” J. Appl. Polym. Sci., vol. 77, no. 2, pp. 409–417, doi: 10.1002/(SICI)1097-4628(20000711)77:2<409::AID-APP18>3.0.CO;2-N (2000)

[47] X. Kuang, K. Chen, C. K. Dunn, J. Wu, V. C. F. Li, and H. J. Qi, “3D Printing of Highly Stretchable, Shape-Memory, and Self-Healing Elastomer toward Novel 4D Printing,” ACS Appl. Mater. Interfaces, vol. 10, no. 8, pp. 7381–7388, doi: 10.1021/acsami.7b18265 (2018)

[48] J. R. A. Pearson, “Instability in Non-Newtonian Flow,” Chem. Eng., no. 1963, pp. 163–181, (1976)

[49] J. tama. bara Karger-Kocsis, Polypropylene handbook, vol. 43, no. 05. Springer US (2006)

[50] J. F. Agassant et al., “Polymer processing extrusion instabilities and methods for their elimination or minimisation,” Int. Polym. Process., vol. 21, no. 3, pp. 239–255, 2006, doi: 10.3139/217.0084 (2006)

[51] Vergnes., “Extrusion Defects and Flow Instabilities of Molten Polymers,” Int. Polym. Process., vol. 30, pp. 3-29, 2015, doi: 10.3138/217.3011 (2015)

[52] B. Boser, I. Guyon, and V. Vapnik, "A Training Algorithm for Optimal Margin Classifiers," Proceedings of the Fifth Annual Workshop on Computational Learning Theory, pp. 144-152, doi:10.1145/130385.130401 (1992)

[53] C. Cortes, V. Vapnik, "Support Vector Networks," Machine Learning vol 20, pp. 273-297, doi: 10.1007/BF00994018 (1995)

[54] T. A. Osswald and J. P. Hernández-ortiz, Polymer processing: modeling and simulation, vol. 44, no. 05. Hanser (2007)

[55] T. A. Osswald and N. M. Rudolph, Polymer rheology, vol. 5, no. 14. Hanser (1961)

[56] J. Bergstra and Y. Bengio, “Random search for hyper-parameter optimization,” J. Mach. Learn. Res., vol. 13, pp. 281–305 (2012)

[57] J. Snoek, H. Larochelle, and R. P. Adams, “Practical Bayesian optimization of machine learning algorithms,” Adv. Neural Inf. Process. Syst., vol. 4, pp. 2951–2959 (2012)

[58] J. L. Garcia, K. W. Koelling, G. Xu, and J. W. Summers, “PVC degradation during injection molding: Experimental evaluation,” J. Vinyl Addit. Technol., vol. 10, no. 1, pp. 17–40, doi: 10.1002/vnl.20004 (2004)

[59] A. Muszaki, “Skin-Core Morphology and Failure,” vol. 27, no. 4 (1987)

[60] J. Zhu and J. C. Chen, “Fuzzy neural network-based in-process mixed material-caused flash prediction (FNN-IPMFP) in injection molding operations,” Int. J. Adv. Manuf. Technol., vol. 29, no. 3–4, pp. 308–316, doi: 10.1007/s00170-005-2528-x (2006)

[61] K. Oda, J. L. White, and E. S. Clark, “Jetting phenomena in injection mold filling mold filling,” Polym. Eng. Sci., vol. 16, no. 8, pp. 585–592, doi: 10.1002/pen.760160811 (1976)

[62] D. Mathivanan and N. S. Parthasarathy, “Prediction of sink depths using nonlinear modeling of injection molding variables,” Int. J. Adv. Manuf. Technol., vol. 43, no. 7–8, pp. 654–663, doi: 10.1007/s00170-008-1749-1 (2009)

[63] J. G. Kovács and B. Sikló, “Experimental validation of simulated weld line formation in injection moulded parts,” Polym. Test., vol. 29, no. 7, pp. 910–914, doi: 10.1016/j.polymertesting.2010.06.003 (2010)

[64] J. G. Kovács and B. Sikló, “Investigation of cooling effect at corners in injection molding,” Int. Commun. Heat Mass Transf., vol. 38, no. 10, pp. 1330–1334, doi: 10.1016/j.icheatmasstransfer.2011.08.007 (2011)

[65] C. Tzoganakis, J. Vlachopoulos, and A. E. Hamielec, “Production of controlled-rheology polypropylene resins by peroxide promoted degradation during extrusion,” Polym. Eng. Sci., vol. 28, no. 3, pp. 170–180, doi: 10.1002/pen.760280308 (1988)

[66] P. Ghosh, D. Dev, and A. Chakrabarti, “Reactive melt processing of polyethylene: Effect of peroxide action on polymer structure, melt rheology and relaxation behaviour,” Polymer (Guildf)., vol. 38, no. 25, pp. 6175–6180, doi: 10.1016/S0032-3861(97)00164-X (1997)

[67] R. Lakes, Viscoelastic Materials. Cambridge University Press. (2009)

[68] T. Kalinowski, J.J. Allaire, and F. Chollet, “Glorot uniform initializer, also called Xavier uniform initializer,” https://keras.rstudio.com/reference/initializer_glorot_uniform.html

[69] M. Morton, “History of synthetic rubber,” Journal of Macromolecular Science: Part A - Chemistry, vol. 15, no. 7, pp. 1289–1302 Morton, M. History of Synthetic Rubber. J. Macromol. Sci. Part A—Chem. 1981, 15, 1289–1302. https://doi.org/10.1080/00222338108056786 (1981)

[70] J. C. Fisher and R. H. Pry, “A simple substitution model of technological change,” Technological Forecasting and Social Change, vol. 3, pp. 75–88, (1971)

[71] X. Ren, C. S. Barrera, J. L. Tardiff, A. Gil, and K. Cornish, “Liquid Guayule natural rubber, a renewable and crosslinkable processing aid in natural and synthetic rubber compounds,” Journal of Cleaner Production, vol. 276, p. 122933, 2020. https://doi.org/10.1016/j.jclepro.2020.122933 (2020)

[72] J.-L. Jacob, J. d’Auzac, and J.-C. Prevôt, “The composition of natural latex fromhevea brasiliensis,” Clinical Reviews in Allergy, vol. 11, no. 3. https://doi.org/10.1007/BF02914415 (1993)

[73] Microwave Technique. Meas. Sci. Rev, 5, 50–54 (2005)

[74] J. Sansatsadeekul, J. Sakdapipanich, and P. Rojruthai, “Characterization of associated proteins and phospholipids in natural rubber latex,” Journal of Bioscience and Bioengineering, vol. 111, no. 6, pp. 628–634, https://doi.org/10.1016/j.jbiosc.2011.01.013 (2011)

[75] M. Salomez, M. Subileau, J. Intapun, F. Bonfils, J. Sainte-Beuve, L. Vaysse, and E. Dubreucq, “Micro-organisms in latex and natural rubber coagula of Hevea brasiliensis and their impact on rubber composition, structure and properties,” Journal of Applied Microbiology, vol. 117, no. 4, pp. 921–929. https://doi.org/10.1111/jam.12556 (2014)

[76] F. Zhao, W. Bi, and S. Zhao, “Influence of crosslink density on mechanical properties of natural Rubber Vulcanizates,” Journal of Macromolecular Science, Part B, vol. 50, no. 7, pp. 1460–1469. https://doi.org/10.1080/00222348.2010.507453 (2011)

[77] N. Sombatsompop, “Analysis of cure characteristics on cross-link density and type, and viscoelastic properties of natural rubber,” Polymer-Plastics Technology and Engineering, vol. 37, no. 3, pp. 333–349. https://doi.org/10.1080/03602559808006932 (1998)

[78] M. Klueppel and G. Heinrich, “Network structure and mechanical properties of sulfur-cured rubbers,” Macromolecules, vol. 27, no. 13, pp. 3596–3603. https://doi.org/10.1021/ma00091a022 (1994)

[79] S. Dasgupta, S. L. Agrawal, S. Bandyopadhyay, S. Chakraborty, R. Mukhopadhyay, R. K. Malkani, and S. C. Ameta, “Characterisation of eco-friendly processing aids for rubber compound: Part II,” Polymer Testing, vol. 27, no. 3, pp. 277–283 https://doi.org/10.1016/J.POLYMERTESTING.2007.11.004 (2008)

[80] P. Raju, V. Nandanan, and S. K. N. Kutty, “A study on the use of castor oil as plasticizer in natural rubber compounds,” Progress in Rubber, Plastics and Recycling Technology, vol. 23, no. 3, pp. 169–180. https://doi.org/10.1177/147776060702300302 (2007)

[81] C. Nakason, S. Saiwaree, S. Tatun, and A. Kaesaman, “Rheological, thermal and morphological properties of maleated natural rubber and its reactive blending with poly(methyl methacrylate),” Polymer Testing, vol. 25, no. 5, pp. 656–667. https://doi.org/10.1016/j.polymertesting.2006.03.011 (2006)

[82] W. Pechurai, T. Muansupan, and P. Seawlee, “Effect of foaming temperature and blowing agent content on cure characteristics, mechanical and morphological properties of natural rubber foams,” Advanced Materials Research, vol. 844, pp. 454–457. https://doi.org/10.4028/www.scientific.net/AMR.844.454 (2013)

[83] N. N. Najib, Z. M. Ariff, A. A. Bakar, and C. S. Sipaut, “Correlation between the acoustic and dynamic mechanical properties of natural rubber foam: Effect of foaming temperature,” Materials & Design, vol. 32, no. 2, pp. 505–511, 2011. https://doi.org/10.1016/j.matdes.2010.08.030 (2011)

[84] J.D. Ferry, Viscoelastic Properties of Polymers; Wiley: Chichester, UK, (1980)

[85] G. M. Thornton, C. B. Frank, and N. G. Shrive, “Ligament creep behavior can be predicted from stress relaxation by incorporating fiber recruitment,” Journal of Rheology, vol. 45, no. 2, pp. 493–507. https://doi.org/10.1122/1.1343877 (2001)

[86] R. C. Koeller, “A theory relating creep and relaxation for linear materials with memory,” Journal of Applied Mechanics, vol. 77, no. 3. https://doi.org/10.1115/1.4000415 (2010)

[87] R. Kane, G. Converse, and R. Roeder, “Effects of the reinforcement morphology on the fatigue properties of hydroxyapatite reinforced polymers,” Journal of the Mechanical Behavior of Biomedical Materials, vol. 1, no. 3, pp. 261–268. https://doi.org/10.1016/j.jmbbm.2008.01.004 (2008)

[88] S. Eslami, P. J. Tavares, and P. M. G. P. Moreira, “Fatigue life assessment of friction stir welded dissimilar polymers,” Procedia Structural Integrity, vol. 5, pp. 1433–1438. https://doi.org/10.1016/j.prostr.2017.07.208 (2017)

[89] J. K. Lee and C. D. Han, “Evolution of polymer blend morphology during compounding in an internal mixer,” Polymer, vol. 40, no. 23, pp. 6277–6296. https://doi.org/10.1016/S0032-3861(99)00022-1 (1999)

[90] M. Fitzka, B. M. Schönbauer, R. K. Rhein, N. Sanaei, S. Zekriardehani, S. A. Tekalur, J. W. Carroll, and H. Mayer, “Usability of ultrasonic frequency testing for rapid generation of high and very high cycle fatigue data,” Materials, vol. 14, no. 9, p. 2245. https://doi.org/10.3390/ma14092245 (2021)

[91] J. M. Hooper and J. Marco, “Understanding vibration frequencies experienced by electric vehicle batteries,” Hybrid and Electric Vehicles Conference 2013 (HEVC 2013). https://doi.org/10.1049/cp.2013.1908 (2013)

[92] E. Mora, L. D. Artavia, and C. W. Macosko, “Modulus development during reactive urethane foaming,” Journal of Rheology, vol. 35, no. 5, pp. 921–940. https://doi.org/10.1122/1.550163 (1991)

[93] J. Park, T. Siegmund, and L. Mongeau, “Viscoelastic properties of Foamed Thermoplastic Vulcanizates and their dependence on Void Fraction,” Cellular Polymers, vol. 22, no. 3, pp. 137–156. https://doi.org/10.1177/026248930302200301 (2003)

[94] S. Shi, J. Liang, and R. He, “Thermal decomposition behavior of silica-phenolic composite exposed to one-sided radiant heating,” Polymer Composites, vol. 36, no. 8, pp. 1557–1564. https://doi.org/10.1002/pc (2014)

[95] H. Ismail, P. K. Freakley, I. Sutherland, and E. Sheng, “Effects of multifunctional additive on mechanical properties of silica filled natural rubber compound,” European Polymer Journal, vol. 31, no. 11, pp. 1109–1117. https://doi.org/10.1016/0014-3057(95)00066-6 (1995)

[96] N. Nasruddin and T. Susanto, “Study of the mechanical properties of natural rubber composites with synthetic rubber using used cooking oil as a softener,” Indonesian Journal of Chemistry, vol. 20, no. 5, p. 967. https://doi.org/10.22146/ijc.42343 (2020)

[97] Y. Lin, Y. Chen, Z. Zeng, J. Zhu, Y. Wei, F. Li, and L. Liu, “Effect of zno nanoparticles doped graphene on static and dynamic mechanical properties of natural rubber composites,” Composites Part A: Applied Science and Manufacturing, vol. 70, pp. 35–44. https://doi.org/10.1016/j.compositesa.2014.12.008 (2015)

[98] F. Pedregosa. G. Varoquaux, A. Gramfort, V. Michel, B. Thirion, O Grisel, M. Blondel, P. Pretenhofer, R. Weiss, V. Du-bourg, et al. Scikit-learn: Machine Learning in Python. J. Mach. Learn. Res., 12, 2825–2830. (2011)

[99] M. Abadi, A. Agarwal, P. Barham, E. Brevdo, Z. Chen, C. Citro, G.S. Corrado, A. Davis, J. Dean, M. Devin, et al. TensorFlow: Large-Scale machine learning on heterogeneous distributed systems. arXiv, arXiv:1603.04467 (2016)

[100] D.P Kingma, J.L. Adam: A method for stochastic optimization. In Proceedings of the 3rd International Conference on Learning Representations, San Diego, CA, USA (2015)

[101] T.A. Osswald, Understanding Polymer Processing: Processes and Governing Equations; Hanser Publishers: Munich, Germany (2018)

[102] J. Shen, X. Lin, J. Liu, and X. Li, "Effects of cross-link density and distribution on static and dynamic properties of chemically cross-linked polymers," Macromolecules, vol. 52, no. 1, pp. 121–134. https://doi.org/10.1021/acs.macromol.8b01389 (2018)

[103] S. S. Fernandez, S. Kunchandy, and S. Ghosh, "Linseed oil plasticizer based natural rubber/expandable graphite vulcanizates: Synthesis and characterizations," Journal of Polymers and the Environment, vol. 23, no. 4, pp. 526–533. https://doi.org/10.1007/s10924-015-0721-z (2015)

[104] E. Brochu, V.M. Cora, N.A. de Freitas, tutorial on bayesian optimization of expensive cost functions, with application to active user modeling and hierarchical reinforcement learning. arXiv, arXiv:1012.2599 (2010)

[105] Q. Lu, L. D. González, R. Kumar, and V. M. Zavala, "Bayesian optimization with reference models: A case study in MPC for HVAC central plants," Computers & Chemical Engineering, vol. 154, p. 107491. https://doi.org/10.1016/j.compchemeng.2021.107491 (2021)

[106] P. Virtanen, R. Gommers, T. E. Oliphant, M. Haberland, T. Reddy, D. Cournapeau, E. Burovski, P. Peterson, W. Weckesser, et al., "SciPy 1.0: Fundamental algorithms for scientific computing in python," Nature Methods, vol. 17, no. 3, pp. 261–272. https://doi.org/10.1038/s41592-019-0686-2 (2020)

[107] J. L. Colón Quintana, S. Hiemer, N. Granda Duarte, and T. Osswald, "Implementation of shear thinning behavior in the fused filament fabrication melting model: Analytical solution and experimental validation," Additive Manufacturing, vol. 37, p. 101687, (2021)

[108] D. Kazmer, A.M. Peterson, D. Masato, A.R. Colon, J. Krantz, J., Polym. Eng. Sci. 2023, 63(3), 943. DOI: 10.1002/pen.26256

[109] M.A. Sellés, S. Sanchez-Caballero, E. Perez-Bernabeu, “Analysis and review of different tools to calculate the production economics in injection molding”, *Procedia Technology*, 12, pp. 439-441, 2014, DOI: 10.1016/j.protcy.2013.12.511

[110] B. P. Conner, G. P. Manogharan, A. N. Martof, L. M. Rodomsky, C. M. Rodomsky, D. C. Jordan and J. W. Limperos, "Making sense of 3-D printing: Creating a map of additive manufacturing products and services," *Additive Manufacturing*, vol. 1–4, no. October 2014, pp. 64-76, 2014, DOI: 10.1117/12.2082521

[111] B. Ahuja, M. Karg, M. Schmidt, M., “Additive Manufacturing in Production – Challenges and Opportunities”, *Proc. SPIE 9353, Laser 3D Manufacturing II*, 935304, 2015, DOI: 10.1117/12.2082521

[112] T. T. Wohlers, I. Campbell, O. Diegel, R. Huff, and J. Kowen, Wohlers Report 2022: 3D Printing and Additive Manufacturing Global State of the Industry. Fort Collins, CO: Wohlers Associates, 2022.

[113] A. Elkaseer, S. Schneider, SG Scholz, “Experiment-based process modeling and optimization for high-quality and resource efficient FFF 3D printing”, *Appl. Sci.*, vol 10, 2020, DOI: 10.3390/app10082899

[114] B. Shaqour, M. Abuabiah, S. Abdel-Fattah, et al. “Gaining a better understanding of the extrusion process in fused filament fabrication 3D printing: a review.” *Int J Adv Manuf Technol*, 114, 1279–1291, 2021, DOI:10.1007/s00170-021-06918-6

[115] Ahn. S.H., Montero, M., Odell, D., Roundy, S., Wright, P.K., “Anistropic material properties of fused deposition modeling ABS”, *Rapid Prototyp. J.*, 8 (4), pp 248-257, DOI: 10.1108/13552540210441166 (2002)

[116] A. Bagsik, V. Schoppner, “Mechanical properties of fused deposition modeling parts manufacturing with Ultem9085”, *ANTEC 2011*, 1294 (2011)

[117] Z. Constance, M. Sharma, and S. Ziemian. "Anisotropic mechanical properties of ABS parts fabricated by fused deposition modelling." Mechanical engineering 23 159-180. (2012):

[118] D. Jiang, D. Smith, “Anisotropic mechanical properties of oriented carbon fiber filled polymer composites produced with fused filament fabrication”, *Additive Manufacturing*, vol 18, pp 84-94, DOI:10.1016/j.addma.2017.08.006

[119] T. Mulholland, S. Goris, J. Boxleitner, T.A. Osswald, N. Rudolph, “Process-Induced Fiber Orientation in Fused Filament Fabrication.” *J. Compos. Sci.*, 2, 45. DOI: 10.3390/jcs2030045 (2018)

[120] T. A. Osswald, G. Menges, Material Science of Polymers for Engineers, Ed. 3E. Hanser (2012)

[121] “Metals, metallic elements and alloys - thermal conductivities,” Engineering ToolBox, https://www.engineeringtoolbox.com/thermal-conductivity-metals-d_858.html (accessed Aug. 23, 2023).

[122] B.A. Davis, P.J. Gramann, J. Del P. Noriega, T.A. Osswald,“Grooved feed single screw extruders - Improving productivity and reducing viscous heating effects*”. Polym. Eng. Sci.* 38, 1199–1204. DOI: 10.1002/pen.10288 (2004)

[123] SABIC: *SABIC STAMAX*, Material Data sheet, (2017)

[124] G. A. Mazzei Capote, "Predicting Mechanical Properties of Fused Filament Fabrication Parts." Order No. 28961684, The University of Wisconsin - Madison, United States -- Wisconsin, 2021.

[125] C. Tucker, Fundamentals of Fiber Orientation, Description, Measurement and Prediction, Ed. 1. Hanser (2022)

[126] N.M. Larson, J. Mueller, A. Chortos, et al. “Rotational multimaterial printing of filaments with subvoxel control.” *Nature* 613, 682–688 DOI: 10.1038/s41586-022-05490-7 (2023)

[127] U. Yilmazer, M. Cansever, “Effects of processing conditions on the fiber length distribution and mechanical properties of glass fiber reinforced nylon-6*”, Polym Compos*, 23: 61-71. DOI: 10.1002/pc.10412 (2002)

[128] S. Goris, T. Back, A. Yanev, D. Brands, D. Drummer, T.A. Osswald, “A novel fiber length measurement technique for discontinuous fiber-reinforced composites: A comparative study with existing methods” *Polym. Compos.*, 39: 4058-4070. DOI: 10.1002/pc.24466 (2018)

[129] H. Wang, “Accurate length measurement of multiple cotton fibers,” *J. Electron. 93 Imaging,* vol. 17, no. 3, p. 031110, (2008).

[130] Z. Yang, Z. Yang, H. Chen, W. Yan, “3D printing of short fiber reinforced composites via material extrusion: Fiber breakage”, *Additive Manufacturing*, 58, 103067, DOI: 10.1016/j.addma.2022.103067

[131] S. Charlon, J. Le Boterff, J. Soulestin, “Fused filament fabrication of polypropylene: Influence of the bead temperature on adhesion and porosity”, *Additive Manufacturing*, vol 38, 101838, DOI: 10.1016/j.addma.2021.101838 (2020)

[132] X. Gao, S. Qi, X. Kuang, Y. Su, J. Li, D. Wang, “Fused filament fabrication of polymer materials: A review of interlayer bond”, *Additive Manufacturing*, vol 37, 101658, DOI:10.1016/j.addma.2020.101658 (2020)